School of Science and Technology

Mathematical Modelling and Design of Current Sensors in Non-Conventional Instrument Transformers

Bojan Nikolic

This thesis is submitted for the fulfilment of the requirements for the degree of Doctor of Philosophy of the City, University of London

June 2023

LIST OF PAPERS

1. B. Nikolić and S. H. Khan, "Modelling and design of low-power, non-conventional current sensors based on smart materials for high-voltage transmission lines," *Meas. Sci. Technol.*, vol. 34, no. 3, article no. 035104, 2022. doi: 10.1088/1361-6501/ac9daf

2. B. Nikolić and S. Khan, "Modelling and optimisation of design of non-conventional instrument transformers," *J. Phys. Conf. Ser.*, vol. 1379, article no. 12057, 2019. doi: 10.1088/1742-6596/1379/1/012057

3. B. Nikolić and S. Khan, "Modelling of non-conventional instrument transformers (NCIT) by FEM," *J. Phys. Conf. Ser.*, vol. 1065, article no. 72046, 2018. doi: 10.1088/1742-6596/1065/7/072046

4. B. Nikolić, S. Khan, and N. Gabdullin, "Development of non-conventional instrument transformers (NCIT) using smart materials," *J. Phys. Conf. Ser.*, vol. 772, article no. 12065, 2016. http://dx.doi.org/10.1088/1742-6596/772/1/012065

TABLE OF CONTENTS

List of Figures

List of Tables

Abstract

This research brings a novel approach for current measurement using magnetic shape memory (MSM) smart alloys. The non-conventional instrument transformer (NCIT) proposed in this research uses the property of these alloys that their shape changes when exposed to a magnetic field.

It has been shown that it is possible to measure alternating currents (a.c.) in high voltage overhead transmission lines by correlating the magnetic field produced by the current to shape changes in an MSM-based sensor. Methodologies for finite element modelling of the proposed NCIT have been developed. The developed methodology and obtained results are validated by comparing them to the results obtained through an experiment done by a manufacturer of MSM materials

5M Ni-Mn-Ga MSM crystals with Type I twin boundaries and a load of 0.5 N/mm^2 were identified as the most suitable type of MSM materials for this application. The combination of a very long fatigue life, with relatively low twinning stress, makes them the most prospective for use in MSM-based current sensors.

The main characteristics of overhead transmission lines are described as well as the types of conductors typically used. This analysis brought us to the conclusion that special attention in this research should be given to ACSR and AAAC conductors, more specifically to 528-Al1/69-ST1A conductor (old code MOOSE) and 996-AL5 (old code REDWOOD). Additionally, the latest trends in the development of overhead transmission lines are discussed, as well as international standards which are relevant to these types of lines.

These conductors were modelled in finite element (FE) package ANSYS APDL, together with the MSM element and the magnetic circuit, and included into a single finite element model. This approach allows us to take into account significant changes that take place within an MSM element during its elongation. Based on this, we were able to determine both the bottom and upper limits of the measurement range, optimise the NCIT for transmission lines, and propose several designs of the NCIT. Finally, this allowed relating the current inside the conductor to the voltage at the output of the LVDT.

List of Abbreviations

5M – Five layer-modulated microstructure

AAAC – All aluminium alloy conductor

AAC – All aluminium conductor

AACSR – Aluminium alloy conductor steel reinforced

AC – Alternating current

ACAR– Aluminium conductor alloy reinforced

ACSR – Aluminium conductor steel reinforced

AMR – Anisotropic magnetoresistance

CT – Current transformer

DC – Direct current

EHV – Extra high voltage

EMF – Electromotive force

FBG – Fibre Bragg grating

GMI – Giant magnetoimpedance

GMM – Giant magnetostrictive materials

GMR – Giant magnetoresistance

HV – High voltage

HVAC – High-voltage alternating current

IEC – International electrotechnical commission

LPG – Long-period grating

LVDT – Linear variable differential transformer

MTJ – Magnetic tunnel junction

MSM – Magnetic shape memory

MSMA – Magnetic shape memory alloy

NCIT – Non-conventional instrument transformer

PCB – Printed circuit board

SMA – Shape memory alloys (thermally activated)

FEM – Finite element method

UHV – Ultra high voltage

1. INTRODUCTION

1.1. Motivation for this study

The measurement of current transformers with an iron core has been the conventional method in electrical power systems. However, the incompatibility of these transformers with modern measurement equipment has been a significant disadvantage that has driven the development of non-conventional instrument transformers (NCITs). These NCITs typicaly use other materials that have a better response to rapidly changing signals. This PhD research proposes a novel solution for current measurement using magnetic shape memory (MSM) materials and presents the methodology for finite element modeling of the proposed NCIT.

Conducting research on non-conventional instrument transformers based on MSMs using FEM will contribute to the advancement of the field of electrical engineering. This can involve developing new techniques, approaches, or methodologies that can improve the performance, accuracy, and efficiency of instrument transformers. The unique characteristics of MSMs allow for the development of non-conventional instrument transformers with a high degree of accuracy, compactness, and low power consumption. The proposed PhD study aims to investigate the design and analysis of non-conventional instrument transformers based on MSM materials using FEM simulation tools, particularly ANSYS APDL. The accuracy and efficiency of the proposed models will be evaluated and compared with existing models and experimental results. The results of this study are expected to contribute to the advancement of non-conventional instrument transformers, particularly those based on MSMs, and enhance their potential for widespread adoption in the power system industry.

Another motivation for this study is exploration of new materials. Magnetic shape memory alloy (MSMA) is a relatively new material that has not been extensively studied in the context of instrument transformers. By conducting research on MSMAs, it is possible to explore their properties, behavior, and applications in instrument transformers. This can lead to the development of new materials with improved characteristics that can be used in

non-conventional instrument transformers. Additionally, it can expand our understanding of MSMAs and their potential for use in other fields of electrical engineering.

Instrument transformers are critical components in electrical power systems, and their performance and accuracy can have a significant impact on the safety, reliability, and efficiency of the system. By developing non-conventional instrument transformers based on MSMAs, practical solutions can be created that can improve the performance and accuracy of these systems. The proposed NCIT can be primarily used for measuring AC currents in overhead transmission lines. The design flexibility of NCITs provides full compatibility with modern digital measuring devices and opens up possibilities for many applications.

This research proposes a novel solution for current measurement using MSMs. The characteristics and unique properties of MSMs are described, and special attention is given to their use in measuring currents in overhead line conductors. The proposed device's design has been optimized, and an evaluation of its performance has been done using models developed in ANSYS APDL, one of the most popular FEM software for the simulation of electromagnetic phenomena. The model of overhead line conductors, together with MSM elements and a magnetic circuit, has been developed. The results of this study can contribute to the advancement of non-conventional instrument transformers, particularly those based on MSMA, and enhance their potential for widespread adoption in the power system industry, ultimately leading to more efficient, accurate, and reliable power systems

The last part of this dissertation reflects on the obtained results and discusses possible routes for further development, demonstrating the potential of non-conventional instrument transformers based on MSM for future applications in the power system industry.

1.2. Aims and objectives

The reasoning above sets academic and industrial context, and from this evolves the main aim of this project: mathematical modelling and design of current sensing elements used in modern non-conventional instrument transformers.

This would be achieved by fulfilling the following primary objectives:

(a) development of methodologies for 2D/3D finite element modelling of low power current transformers;

(b) design optimisation and performance evaluation of appropriate CTs using the models developed in (a);

(c) validation of modelling results by comparing them with data obtained by experimental studies

1.3. Research methods and plan of the thesis

This chapter presents the research methodology employed in this thesis as well as a plan of the thesis. The purpose of this chapter is to outline the approach, techniques, and tools used to address the research objectives and answer the research questions. The chapter provides a description of the research design, data collection methods, data analysis techniques, and the overall structure of the research.

1.3.1. Research questions and plan of the thesis

To achieve the research objectives, several research questions will be addressed.

In Chapter 2, questions such as "What are the characteristics and applications of modern current measurement techniques, including optical sensors, Rogowski coils, magnetic sensors, and Hall effect sensors?" are addressed. It was shown that there are many different solutions for current measurement suggested nowadays. Their existence shows the popularity and importance of this topic. In this chapter, optical current sensors, Rogowski coils, magnetic current sensors and sensors based on the Hall Effect were described, with a focus on their advantages and disadvantages. Only a few of these solutions have found industrial application, and there are still many challenges that need to be overcome.

The focus of Chapter 3 is on overhead transmission lines, as the application of the proposed new sensor should primarily be for measuring AC in overhead line conductors, especially at high voltage. In this chapter, an overview of configurations of transmission lines that can be found worldwide was made, as well as the types of conductors that are typically used. The factors which influence the choice of conductors and their power capabilities were discussed. Questions such as which conductors are typically used at high voltage transmission lines, what is the current ampacity of those conductors, as well as typical values of currents, are answered in this chapter. Additionally, the latest trends in the development of overhead transmission lines are discussed at the end of Chapter 3, as well as international standards which are relevant to these types of lines.

The characteristics and unique properties of MSM elements are described in Chapter 4. The novel current measuring principle using this material is proposed and described in this chapter. MSM alloys have a remarkable magnetic field-induced strain that is more than one order of magnitude higher than the maximum strains produced by conventional magnetostrictive (e.g. Terfenol-D) and piezoelectric materials, reaching the strains of well-known thermal shape memory alloys. However, unlike thermal shape memory alloys, MSM alloys do not involve a phase transformation. As a result, their response to magnetic field excitation is significantly faster, and they have a very long fatigue life. Furthermore, at the end of Chapter 4, an overview of available LVDTs is made, as well as considerations of which type and which characteristics would be most suitable for the proposed NCIT.

The focus of Chapter 5 is on modelling and evaluation of the performance of the proposed current sensor using ANSYS APDL. The modelling approach is validated by comparing the

obtained results with results obtained through another research. An analytical approach to computing electromagnetic processes has been presented, as well as the importance of the finite element method (FEM) in many practical applications. Some physical phenomena important for this research, such as skin and proximity effects, were also discussed in this chapter.

In this chapter, some of the questions that are answered are:

- How can the FEM be employed to model the electromagnetic fields of high voltage conductors?
- How can the geometric parameters and suitable materials be determined for the design and optimisation of non-conventional instrument transformers?
- How does the strain of the MSM element correlate with the conductor current?
- How does voltage at the output of the LVDT correlate with the conductor current?
- How can these correlations be utilized for current sensing?
- What are the modelling errors associated with the developed models?

Several designs of the proposed current sensor have been suggested, which could be used to measure various ranges of AC in overhead transmission lines. Additionally, possible routes for further development of the sensor have been discussed at the end of this dissertation.

1.3.2. Research design

This research will adopt a comprehensive mixed-methods approach, combining experimental measurements and simulation-based modelling.

Simulation and modelling will be carried out using the finite element method to develop precise mathematical models of high voltage conductors and non-conventional instrument transformers. The FEM simulations will involve setting up the material properties, geometric configurations, and boundary conditions of the models. To validate the results obtained from the simulations, they will be analysed and compared with experimental measurements obtained through another research.

1.3.3. Data collection and data analysis methods

The research data will be collected through literature review, and simulation and modelling.

A comprehensive literature review will be conducted to gather relevant information on modern current measurement techniques, conductor selection for overhead transmission lines, international standards, power carrying capacities of transmission lines, characteristics, and operation principles of MSM materials, and relevant modelling methods.

Simulation and modelling will be conducted using the finite element method to generate data on the electromagnetic fields and performance of high voltage conductors and non-conventional instrument transformers. The data obtained from these simulations will be used for analysis and comparison with experimental measurements.

The data obtained from the FEM simulations will be analysed by comparing the model predictions with the experimental measurements. The accuracy, precision, and other relevant performance metrics of the models will be assessed and evaluated.

1.3.4. Limitations of the research

The research is subject to certain limitations, such as the availability of resources, the complexity of the mathematical models, and assumptions made during the modelling process. The research will strive to acknowledge and address these limitations transparently, while ensuring that the validity and reliability of the research findings are upheld.

This chapter provided an overview of the research methods employed in the study. It outlined the research questions, research design, data collection methods, data analysis methods, limitations of the research, and a plan of the thesis. By utilizing a mixed-methods approach and incorporating experimental measurements and simulation-based modelling, this research aims to develop accurate mathematical models for non-conventional

instrument transformers and high voltage conductors, as well as to design and optimise current sensors based on these models.

2. A REVIEW OF MODERN CURRENT MEASUREMENT TECHNIQUES

The focus of this chapter will be on the modern ways of measuring electrical currents such as using optical sensors, Rogowski coil, different types of magnetic sensors, or Hall effect sensors.

However, at the beginning of this review, we will briefly mention the most simple and basic way to measure current – shunt. By measuring the voltage at the ends of a resistor and the known value of its resistance, the value of the current in the circuit is obtained. This way of measuring has a lot of limitations and can be used in a very limited number of situations. No galvanic isolation (the current-sensing instrument must become part of the circuit being monitored) for some applications such as the ones operating at low voltage and power levels may not be an issue, but for other applications, safety concerns will make it mandatory that the measurement circuit is separated from the power-handling circuit.

2.1. Optical current sensors

The discovery of fibre optics has revolutionised the industry in many ways, but what is of special interest for this research is their application as fibre sensors. Several ideas for current measurement using optical sensors were proposed in various papers. [1-14].

The use of optical fibres as sensing elements for electric current measurements has been developed by several methods such as those utilizing magnetic field to generate the Faraday effect, magnetomotive force to make fibres bend, magnetostrictive material bonded on a fibre to contract or lengthen the fibre, and heating effect to change the fibre's length and refractive index. In all the above methods, perturbations such as magnetic field, pressure, strain and temperature are induced by the measurand i.e. electric current, accordingly resulting in a change of the optical fibre characteristics and then modulation of light within the fibre. More details about the characteristics of optical sensors and proposed solutions for current measurement can be found in [1-14].

Optical current sensors usually use one of the two principles for measurement of current: change of fibre-grating wavelength or Faraday's effect. There are two main types of fibre gratings: short-period gratings or fibre Bragg gratings (FBG) and long-period gratings (LPG). It should be noted at the outset that current sensors based on Faraday's effect (effect of plane rotation of polarised light when it travels through a magnetic field) have too low sensitivity for practical applications, are extremely difficult to implement accurately and stably and may only be affordable for high voltage lines. [3],[15] Consequently, more attention will be given to the sensors based on the first of the above optical principles.

To explain these approaches and discover their advantages and disadvantages, some physical principles need to be reviewed.

2.1.1. Fibre Bragg grating

A Fibre Bragg grating (FBG) acts as a mirror, reflecting the light of a specific wavelength as it is shown in Figure 2.1.1. The spatial period of the fibre and its effective index determine the Bragg wavelength at which the reflection would be maximum.

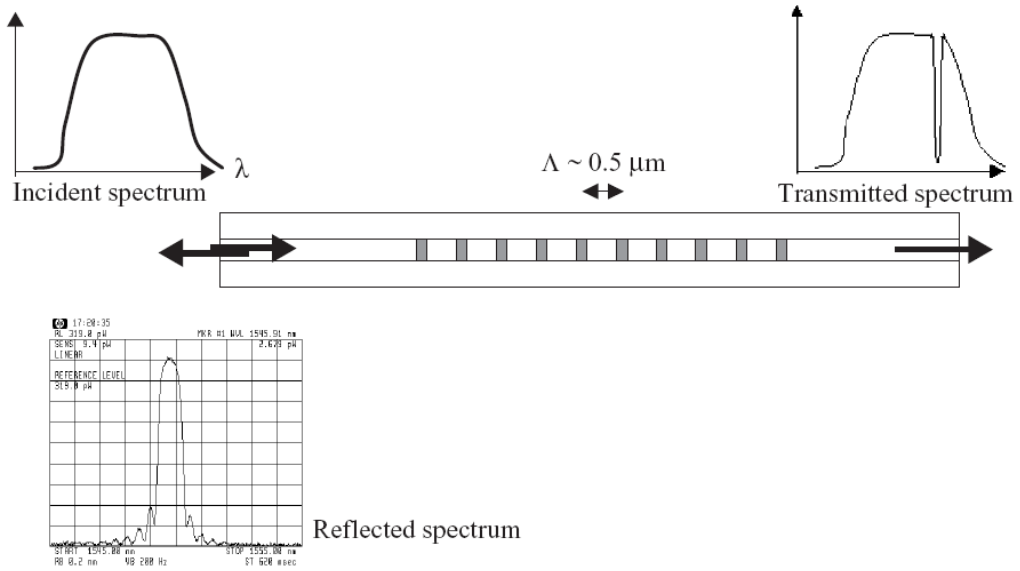

Figure 2.1.1 – An FBG reflects light of a specific wavelength and thus acts like a wavelength-selective reflector [16]

When the light containing various wavelengths is incident on an FBG, only the wavelength corresponding to the Bragg wavelength will get strongly reflected and the other wavelengths get transmitted to another end of the fibre.

FBGs have a very good potential for applications as sensors for sensing mechanical strain, temperature, acceleration and similar. Furthermore, they have attracted a lot of intention lately to be used for measuring electrical current.

The Bragg wavelength depends on both the refractive index of the fibre and the period of the grating. The basic principle of using FBGs in sensing applications is based on measuring the changes in the reflected wavelength which can be caused by any external parameter which is needed to measure. Very often FBGs are used in a way that when they are strained, their grating is elongated, which causes an increase in the period of grating and small changes in the refractive index of the fibre. The result of this is a change in the Bragg wavelength of the grating.

FBGs can be also used as temperature sensors because the fact that the refractive index and the period of the grating change with a temperature change, thus when the temperature is changed the change in the peak reflected wavelength will also occur. The temperature sensitivity of FBGs is typically about 6 pm/◦C. [16] These values of the peak wavelength change are very small and special techniques need to be used to measure them.

One of the advantages of FBG sensors is the possibility to multiplex them which is shown in Figure 2.1.2. Several FBGs with different Bragg wavelengths, chosen such that they do not overlap each other, are placed at different points along the length of a single-mode fibre. By measuring changes in the Bragg wavelength of individual FBGs, it is possible to sense the strains or temperature changes at each FBG location independently.

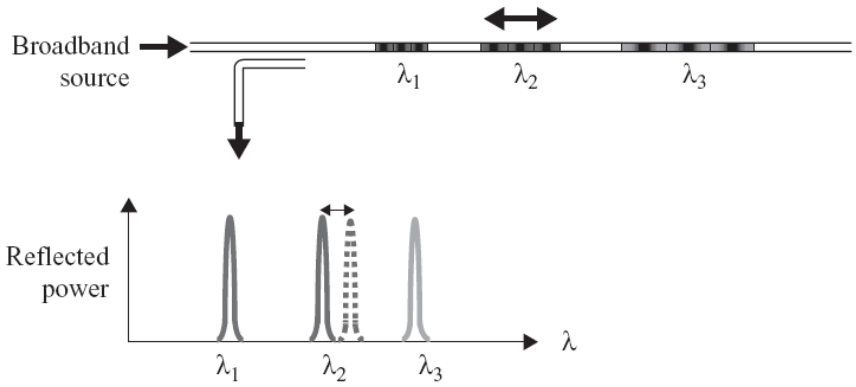

Figure 2.1.2 – Multipoint sensor based on FBGs reflecting at various wavelengths [16]

One of the problems when using FBGs is the problem of differentiating the changes of the Bragg wavelength caused by strain from those caused by temperature changes. On the other hand, they are not sensitive to fluctuations of light intensity as the measurement is based only on the wavelength shift of the reflected peak. This shift is almost a linear function of strain and temperature [16] and mass production is easily achievable.

2.1.2. Long-period grating

In contrast to FBGs, long-period gratings (LPGs) do not reflect anything, but instead, the waves of certain wavelengths are not transferred forward because they are lost in the fibre cladding (Figure 2.1.3). These gratings act as wavelength-dependent loss components. This is a reason why LPGs, unlike FBGs that exhibit dips in the transmission and a peak in the reflection spectrum, only show dips in the transmission spectrum.

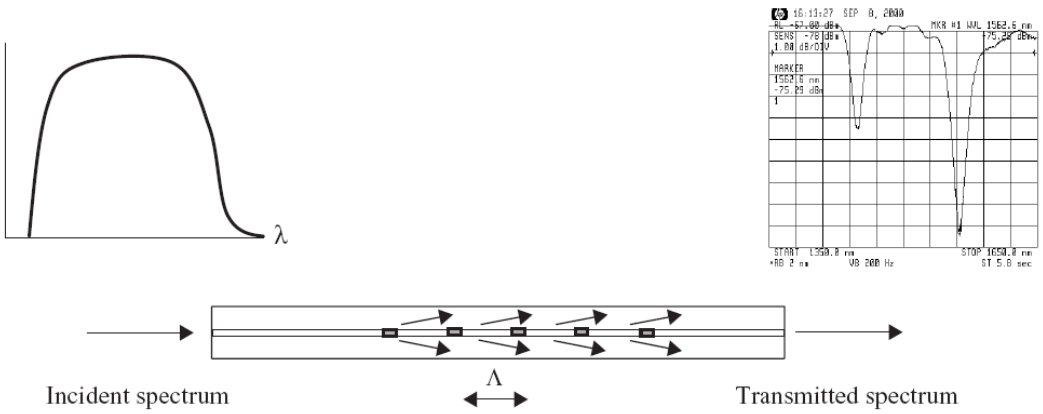

Figure 2.1.3 – Propagation of the LPG-coupled light in fibre [16]

The FBG's spatial period of modulation is approximately 0.5 µm. That means that the refractive index of the fibre core varies periodically along the fibre and has the same value after every 0.5 µm. The spatial period of an LPG is usually a few hundred micrometres.

LPGs are very sensitive to strain, temperature and bending. Since any change around the fibre cladding could influence the power transmitted through the fibre, this fact can be used to realise very sensitive sensors. The temperature sensitivity of an LPG can be as high as 3.4 nm/°C. The LPG strain sensitivity is up to 33.6 nm/mε. [16]

2.1.3. Faraday effect

The Faraday effect describes the behaviour of the light when it is exposed to the magnetic field. When a linearly polarised light beam propagates through media (such as ordinary glass), its state of polarisation normally will not change. However, if a magnetic field is applied along or opposite to the direction of propagation of the light beam in the medium, the polarisation plane of the propagating light beam will rotate. This effect is called the Faraday effect.

The angle of rotation is proportional to the length of the propagated path, applied magnetic field, and it also depends on the material through a constant called the Verdet constant. It can be calculated using the following equation [16]:

$$\theta = VNI \tag{2.4}$$

where are

V - Verdet constant, which for silica has a value of $2.64 \cdot 10^{-4}$ degree/A

N - turns of fibre around the current-carrying conductor

I - current passing through the conductor

The main idea behind the current sensor based on the Faraday effect is that by measuring the angle of the plane rotation of the polarised light, it is possible to measure the magnetic field which is produced by a current-carrying conductor. Using this effect, it is possible to measure currents greater than tens of kiloampers. [16]

2.1.4. Characteristics of optical sensors

One of the main advantages of optical sensors is the fact that there is an optical signal at their output which makes them very convenient for use in modern systems where a lot of fibre optics is used. Unlike Rogowski sensors, optical sensors are not sensitive to surrounding electromagnetic fields and they are smaller and more compatible with the requirements of modern smart grids. Their nonconductive nature makes them electrically passive which, along with their chemical inertness, makes them an excellent choice for measurement in corrosive and explosive environments. Generally, optical sensors don't saturate and have linear outputs comparable to Rogowski sensors.

Optical sensors are lightweight which helps to produce portable equipment, but also a collector, which contains all accompanying electrical components and, hence does not need to be placed near the measurement location when fibre optics is used. This is very useful for current measurement in the presence of high voltages. This is not only because it is easier to place equipment and manipulate later with it, but also because sensor electronics at the ground level are separated from the optical fibre at high voltage. They can be easily used for remote operations and inspections over long distances.

Even though it is possible to add to the list of very positive features of optical sensors features like large bandwidth and the possibility to achieve highly accurate current measurements, there are also several drawbacks of this technology. They are very sensitive to vibrations, temperature and other environmental effects making outdoor installation complex. The temperature sensitivity of FBG is typically around 6 pm/˚C, and for LPG it can be as high as 3.4 nm/˚C [16]. Their output data are more unstable than those of the Rogowski coils [1].

The time delay of the fibre optic current sensor's output signal is generally around 100µs [17], while some magneto-optical sensors (sensors which use the Faraday's effect) with ns response have been produced. [18] One of the main disadvantages of current measurement using FBG or LPG is often a very complex demodulation system needed for the wavelength shift measurement. High production costs due to the high demand for materials and complex production processes make it difficult for them to achieve mass production.

2.2. Rogowski coils

One of the most popular sensors for current measurement is a Rogowski coil. These coils do not have any ferromagnetic core, which allows the current measurement over a wide range (Figure 2.2.1). Using the same Rogowski coil, it is possible to measure currents larger than 1 MA and as small as a few miliampers [19]. Furthermore, current measurement over this wide range is linear since no core can get saturated. More details about the properties of Rogowski coil sensors and the proposed solutions for current measurement can be found in [20-24].

Their measurement principle is based on "sensing" the magnetic field produced by the current, meaning that they cannot be used for the measurement of DC currents. The measurement frequency range is approximately 0.1 Hz-1 GHz [1], so they can be successfully used for the measurement of AC as well as transients.

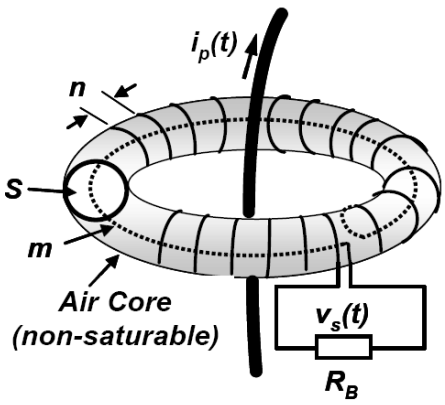

Figure 2.2.1 – Rogowski coil [25]

Rogowski coils are small, compact, lightweight, and their power consumption is very low, which makes current measurements in high-voltage circuits easy and safe owing to the absence of any electrical connections with the measured circuit. There are also the so-called flexible designs of Rogowski coils which allow measurements without interrupting the current circuit, but their accuracy is less than the accuracy of the non-flexible ones. An example of a flexible design of the Rogowski coil can be seen in Figure 2.2.2. Rogowski sensors cause no disturbances to the measurement system since they draw no power from the main circuit and the inductance added into the circuit due to the presence of the coil is only a few picohenries. [19]

Figure 2.2.2 – Flexible Rogowski coil [26]

Moreover, these coils require almost no maintenance, except for periodical examination for physical damage if the coils are exposed to some harsh environment. They can be calibrated at any convenient current level and later used for any current level, including very large currents. They cause no damage by large overload.

Furthermore, considering that the same device can be used for current measurement, control and protection and that it has a low price, it is more than clear why Rogowski coils found wide applications in industry. However, there are several drawbacks which point to other instruments for current measurement.

One of their main disadvantages is sensitivity to surrounding electromagnetic fields, meaning that some kind of shielding is needed. Their output is very small which necessitates proper grounding and shielding. The voltage on the coil's output is in order of μV for primary currents below 100A. However, at the same time, such low sensitivity can be their advantage in some applications.

Measurement errors are typically in the range from 5-20% of the rated current [19], but there are some measures which increased their accuracy [22] where the error is in the range from 0.5-5% of the rated current.

This issue is partly addressed by the design of printed circuit board (PCB) Rogowski coils, which have better accuracy (0.2-0.5% accuracy class) and higher immunity to external fields compared to classical Rogowski coils, but at the same time, their output voltage is lower [25]. Figure 2.2.3 shows a design of two PCBs where each one has an imprinted Rogowski coil. To reduce the magnetic influence from nearby conductors, coils are wounded in electrically opposite directions.

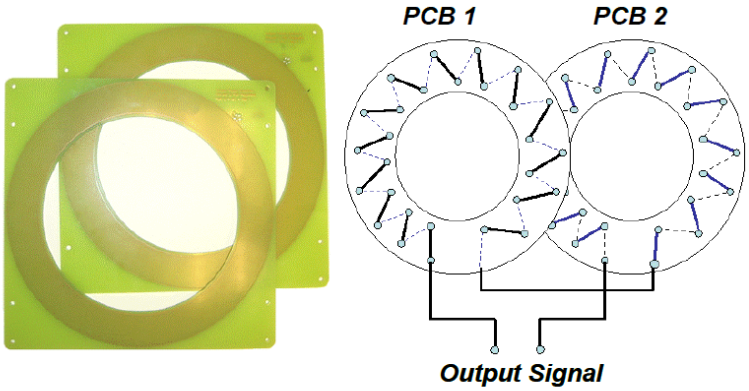

Figure 2.2.3 – Rogowski coil designed on two Printed Circuit Boards [25]

The output voltage of PCB Rogowski coils is smaller than the output voltage of conventional ones because their cross-section is smaller. Therefore, special care should be taken to protect the low-output signal from external disturbances. PCB Rogowski coils in a split-core style have also been designed. Their accuracy, as mentioned earlier, is less than that of non-split core ones.

Electromotive force (EMF) induced in Rogowski coil, *e(t)*, can be calculated using the following formula:

$$e(t) = -M\frac{di(t)}{dt} \tag{2.5}$$

where *M* is the mutual inductance, and *di(t)/dt* is a derivative of the current that needs to be measured.

Another drawback of Rogowski-coil-based current measurement can be seen from this equation. Rogowski coils need an integrator for the vast majority of measurements. In addition to the fact that the integrator affects the accuracy and stability of the Rogowski sensor, the measurements conducted usually require that sampling, A/D conversions and data transmissions are done at measurement locations, which can be impractical in some situations. This also means that if all these electrical components are placed at a high voltage site, a separate power supply is needed.

In certain cases, Rogowski coils do not need an integrator and they can work in the so-called self-integrating mode. The termination resistance of the Rogowski coil needs to be as low as possible to achieve this mode. Such an application is described in [19]. However, Rogowski coils can be used in this mode for measuring only high current impulses. They showed good results in measuring current impulses of duration less than twice the transit time of the coil.

2.3. Magnetic sensors

It is believed that the first non-laboratory use of magnetic sensors was fusing sea mines during World War II. Today, they found their application in many areas, such as in the automobile industry, inside computers, and medical/biological applications. They can be highly sensitive so that they can be used in applications when the effects of the Earth's magnetic field need to be taken into account (such as brain function mapping, magnetic anomaly detection, magnetic compass, munitions fuzing). However, these applications are not of interest to this research as the effects of the Earth's magnetic field, which is in the range of 10^{-4}-10^{-5}T, can be neglected.

Magnetic sensors have attracted a lot of attention in recent years which can be seen by a good number of theoretical papers on magnetic sensors proposing various operating principles. The proposed measurement systems using magnetic sensors usually involve some other transducers and other technologies (very often optical fibre grating), which makes these systems very complex and susceptible to errors. More about magnetic sensors properties and the proposed solutions for current measurement can be found in [3], [6-8], [10], [13],[18], [27-33].

2.3.1. Magnetoresistive sensors

So far many magnetic sensors have been proposed and among them are magnetoresistive sensors. They work on the principle that the magnetic field affects the resistance of the sensor. This could be based on anisotropic magnetoresistance (AMR), giant magnetoresistance (GMR), magnetic tunnel junction (MTJ) and giant magnetoimpedance (GMI) sensors. Sensors which use magnetic force produced by measured current have been also proposed, as well as sensors made of magnetostrictive materials. Of particular interest are magnetostrictive materials, which belong to the group of giant magnetostrictive materials (GMM). All magnetic sensors are generally very small and light which makes them interesting for many applications.

Magnetoresistive magnetometers can be energised by applying a constant current and the output voltage is proportional to the strength of the magnetic field. In AMR sensors, the resistance depends on the angle between the magnetisation and the direction of the current. The most commonly used material is permalloy because it has a relatively large magnetoresistance and some of its characteristics are compatible with fabrication techniques. Permalloy contains around 80% nickel and 20% iron. The resistance changes roughly as the square of the cosine of the angle between the magnetisation and the current direction. They can be used to measure magnetic fields between 10^{-6}T and $5 \cdot 10^{-3}$T in an extremely wide frequency range – from dc to nearly 1GHz. They can sense so weak fields as 10^{-10}T, but only for limited bandwidths. [18]

On the other hand, magnetoresistance is generally not so large and for permalloy, it is less than 4%. Magnetoresistance is defined as a ratio ΔR/R, where ΔR is the change of resistance due to material exposure to a magnetic field, and R is the resistance when there is no magnetic field (H=0).

AMR sensors are usually small, light and require only 0.1-0.5 mW of power. They can operate on temperatures as low as -55˚C and as high as 200˚C. [18]

GMR sensors exhibit a larger change in resistance once they are exposed to the external magnetic field. The simplest design of GMR sensors includes a four-layer structure that consists of an antiferromagnet and two thin ferromagnets separated by a conductor. Their sensitivity range is 10^{-8}-10^{-1}T. [18] They are often used in the read heads of computer hard drives.

MTJ sensors are also called spin-dependent sensors. Their structure is similar to one of GMR sensors, the only difference is that the layer between two ferromagnets is an insulator. A change in resistance of 180%-220% was reported. [34],[35] These sensors have higher magnetoresistance values than GMR sensors, so they use less power than GMR sensors.

They are especially attractive for low-cost applications. Magnetoresistive sensors are generally energy-efficient devices (for example, AMR sensors' power consumption is less than 1W) [15]. They can sense very low magnetic fields (for AMR sensors this can be as low as 0.1nT) as well as relatively strong fields (GMR sensors can be used in fields as large as 0.1T). [18]

2.3.2. Magnetostrictive sensors

Magnetostriction is a property of magnetic materials to expand or contract in response to a magnetic field. This effect allows magnetostrictive materials to convert electromagnetic energy into mechanical energy and vice versa. It is observed in a variety of ferromagnetic and antiferromagnetic materials. The most used one is Terfenol-D.

Increased interest in magnetostrictive sensor technology results from improvements in the performance of magnetostrictive materials and led to increased use of these sensors for a wide range of applications. Whereas magnetoresistive sensors are used mostly for measuring weaker magnetic fields, magnetostrictive sensors can be used also to measure larger ones.

2.3.3. Characteristics and application of magnetic sensors

Despite what has been said earlier, magnetic sensors have several serious drawbacks that prevent their even wider application. They tend to be highly nonlinear and suffer from hysteresis which usually requires some compensation methods to be used to linearise the sensor. Besides, they are also sensitive to temperature changes and, often to vibrations. For example, magnetostrictive materials have a temperature dependence in the order of 5ppm/˚C. [3]

Magnetostriction is a unipolar phenomenon which means that a positive strain is produced in opposite directions of the magnetic field. Furthermore, a relatively large magnetic field is needed to make use of the magnetostrictive property. Their strain output is proportional to the square of the magnetic field strength. Furthermore, since magnetostrictive sensors do not transduce current directly into an electrical form, at least one more step is needed for current measurement.

For magnetoresistive materials, the change of resistance caused by an external magnetic field is very small. For example, for permalloy, which is the most common used material for AMR sensors, this is less than 4%. [18]

The impedance of GMI sensors depends strongly on both the magnetic field strength and its frequency. To benefit from the GMI effect, a high-frequency current of the order of GHz is needed which limits their application as sensors. [18]

As mentioned earlier, there are several papers which propose measurement systems using magnetic sensors in combination with some other technologies. Different combinations of

magnetic sensors and FBGs, very often including some other elements, are very common proposals for current measurement. Especially popular is the application of magnetostrictive materials.

One such solution is proposed in [7] where are combined magnetostrictive rod, FBG mounted on it, lights source and a system for optical demodulation and spectrum analysis. This system, designed for high AC and temperature measurements, although still combining many elements, can be considered very simple in comparison with some other, similar, solutions. The main idea behind the proposed system is to measure electrical current by measuring shifts of wavelengths of reflected light from FBGs. The measuring current amplitude and the temperature are coded in the analysed optical signal. The wavelength shifts are caused by FBG deformation caused by elongation of a magnetostrictive rod which is caused by the magnetic field around the conductor carrying AC. The sensor can be multiplexed and operated long-distance, but the fact that it needs to be mounted directly on a high voltage conductor brings additional challenges in applying this kind of measurement system in practice.

Another example is a fibre optic magnetometer, described in [18]. Two glass fibres are used to form a Mach–Zender interferometer, which is used for spectrum analysis of an optical signal. One of the fibres is wrapped around the magnetostrictive material. When the system is exposed to a magnetic field, magnetostrictive material changes its size, and as a result of that, there will be a slight phase difference at the receiving end between the light which travelled along the fibre wrapped around the magnetostrictive material and another fibre which is used as a reference fibre. This phase difference is used to measure the current which has produced that magnetic field. These sensors have a high sensitivity and can be used to measure magnetic fields in the range of 10^{-11}-10^{-3} T. However, the use of many optical components and magnetic material makes this measurement solution very sensitive to mechanical damage, temperature changes and vibrations.

Another example of the use of magnetostrictive materials is their application together with piezoelectric materials. The three-layer laminate solution, consisting of two layers of magnetostrictive materials separated by a layer of piezoelectric material is proposed in [27]. The most commonly used magnetostrictive material is Terfenol-D. As a piezoelectric material

is used $Pb(Mg_{1/3}\ Nb_{2/3})O_3$ - $PbTiO_3$. Although this solution is passive and consumes no power, its application is very limited because it can measure only very low magnetic fields. Its sensitivity is in the pT range. [27]

For example, in [6] is described an interesting solution for measuring both, static and quasistatic current signals. A pendulum-type solution is proposed which combines a permanent magnet, two FBGs and a current coil. The main idea of the proposed measurement system is to measure a change in received light power, which will occur due to the changes in the reflected FBG spectrum caused by an electromagnetic force produced by the measured current. Although the proposed novel system detection method for demodulation of FBG is electrically passive (and therefore it can be safely applied in corrosive or explosive environments), the system is very sensitive to vibrations and temperature changes. This makes the proposed solution very unreliable for practical applications due to possibly large measurement errors. Although the error of ±1mA in 'most measurements' in the measurement range of 400mA has been reported, it is not clear under what conditions and in what situations the error is in this range and when this is not the case.

2.4. Hall effect sensors

Another very popular method for current measurement is Hall effect sensors.

When a magnetic field is applied to the plate so it is at right angles to the current flow, electrons move toward one of the edges of the plate and thus a small voltage appears across the plate. This voltage can be measured and related to the current through the plate (Figure 2.4.1). If the direction of the magnetic field is reversed, the polarity of induced voltage will also reverse. The Hall effect occurs also under steady-state conditions i.e. when current and magnetic field are constant over time. This means that the sensors based on the Hall effect can be used for measuring both, AC and DC.

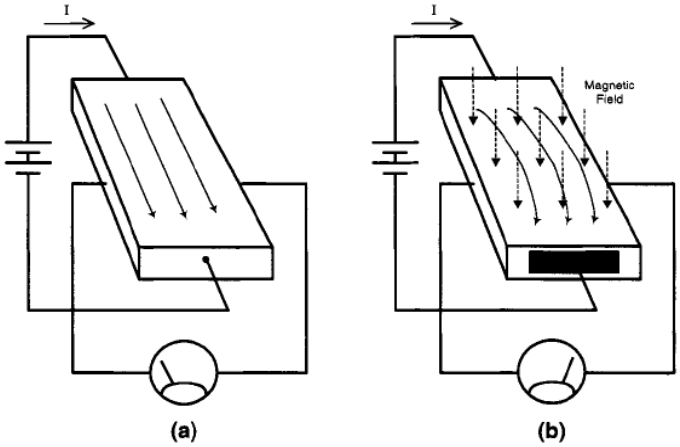

Figure 2.4.1 – Hall effect [36]

These sensors have an easier fabrication process and lower cost compared to Rogowski coils and optical sensors. They can measure currents over a relatively wide frequency range (from DC-1MHz) [18] provided that the current values are between 10mA and 35kA [37]. They are usually very small and linear (linearity errors less than 1% over a significant operating range) [36] and have modest power consumption between 0.1-0.2W [18]. It is possible to install them without interrupting the current circuit. More details about Hall sensors, their characteristics and applications can be found in [38-41].

A major limitation of these sensors is sensitivity drift. The drift is caused by temperature variations, mechanical stress and ageing. The thermal sensitivity drift is typically 500ppm/˚C [38]. The drift due to ageing is unpredictable and cannot be eliminated without regular calibration. It can be up to 2%. [38]

There are many papers which tackle these problems such as [38]. A continuous calibration of the sensor sensitivity is proposed in [38]. Although the sensitivity drift of the sensor is significantly improved (50ppm/˚C), the sensitivity of such a sensor is very low (35V/T). Furthermore, to obtain continuous sensitivity, calibration of a lot of integrated elements is required, including the integrated coil.

Another solution for measuring electrical current and performing a continuous calibration of a Hall sensor is suggested in [39]. The sensitivity drift is improved by using the system called Hall sensor microsystem which consists of a range of electronic components. However, the

sensitivity of the sensor is decreased 4-10 times to its non-calibrated counterpart. The linearity of the proposed sensor is very good (the non-linearity within the range of less than ±0.08%), but its sensitivity drift is 300ppm/˚C which is not such a great improvement in comparison to the solution proposed in [38]. On the other hand, the proposed solution can measure current contactless, but due to the insensitivity of the Hall sensor, an iron core is used to focus the magnetic field towards the sensor.

Very often a Hall sensor is placed in an air gap within an iron core which surrounds the conductor which current is measured. That is the case in the proposed measuring system in [39] too. This kind of approach is mainly used as a low-cost solution for measuring small currents with large bandwidths. Special core materials, which are more expensive, are needed for large current measurements without core saturation. In comparison with the current measurement using Rogowski coils, the proposed solution is more complicated and also requires the use of an iron core which is not desirable because of its saturation properties.

There are solutions which use a Hall sensor to measure current without using an iron core or a lot of electronic components for calibration purposes. One such solution is presented in [40] where four Hall sensors are placed symmetrically, directly on the conductor. The output voltage of all four sensors is averaged to cancel the influence of the other two phases in a three-phase system as well as other magnetic interferences.

Placing Hall sensors directly on conductors overcomes a problem of the sensors' insensitivity, but raises questions about the sensor practicability and reliability. For example, the temperature of the conductor will vary depending on the electrical current through the conductor and environmental conditions and Hall sensors are very sensitive to temperature changes. Although the authors have discussed some other problems which can influence the accuracy of the proposed system, such as unbalanced three-phase currents, fault currents or different arrangements of three-phase cables, they have not discussed and taken into consideration above mention problem of temperature sensitivity.

At the end of this chapter, it might be useful to summarise in a table the main advantages and disadvantages of the current sensing technologies mentioned earlier (Table 2.1) .

Table 2.1 – The main advantages and disadvantages of the reviewed current sensing technologies

OPTICAL SENSORS	**Working principles: the change of fibre-grating wavelength (short fibre grating FBG and long-period grating LPG) and Faraday effect**	
	ADVANTAGES	**DISADVANTAGES**
	Large bandwidth	High production costs
	Accurate measurements	Difficult to achieve mass production
	An optical signal at output is convenient for use of fibre optics	A quite sensitive optical system
	No electromagnetic problems	Susceptible to vibration, temperature and other environmental impacts, so outdoor installation is complex
	The non-conductive nature of optical components, electrically passive, can be used in corrosive or explosive environments	Very complex modulation system of FBGs and LPGs
	A collector does not need to be placed at the measuring location	Faraday effect is difficult to implement accurately and stably way and it has very low sensitivity
ROGOWSKI COIL SENSORS	**Types of Rogowski coils: classical vs. printed circuit board Rogowski coils, flexible and non-flexible ones**	
	ADVANTAGES	**DISADVANTAGES**
	Great linearity over a very wide bandwidth	Very small sensitivity
	Capability to measure a large range of currents	Relatively high measurement errors
	Small, compact, lightweight	Sensitive to other electromagnetic fields
	Low power consumption during operation	Integrator required
	No electrical connection between the measured current and the sensor	Method of interrogation for Rogowski coils usually requires sampling, analogue-to-digital conversion, integration, and data transmission to be performed at the measurement location

		A separate power supply is needed for the collector (integration, A/D sampling etc.) if the collector is at the high voltage side
MAGNETIC SENSORS	**Working principles: magnetoresistive sensors (anisotropic magnetoresistance AMR, giant magnetoresistance GMR, magnetic tunnel junction MTJ, giant magnetoimpedance GMI), sensors utilising magnetic force, sensors based on magnetostriction**	
	ADVANTAGES	**DISADVANTAGES**
	Light and small	Highly nonlinear and hysteretic
	Low power consumption	Sensitive to vibration and temperature
	Low production cost	Magnetic sensors usually require some other transducers and other technologies (very often optical fibre grating), which makes these systems very complex and susceptible to errors.
	Electrically passive, can safely work in corrosive or explosive environments	Magnetostriction is a unipolar phenomenon and it reacts to both positive and negative fields by producing a positive strain.
	Performances of magnetic materials are constantly improving	Whereas relatively large magnetic fields are necessary for the use of magnetostrictive sensors, magnetoresistive sensors can be mostly used in very small fields.
		The change of resistance of magnetoresistive sensors caused by an external magnetic field is very small
HALL EFFECT SENSORS	**Working principle: Hall effect**	
	ADVANTAGES	**DISADVANTAGES**
	Easy fabrication and very low cost	Sensor performances are very affected by temperature, stress and ageing.
	Wide frequency range including the possibility to measure DC currents	The sensor system exhibits non-negligible offset and sensitivity drifts. The drift due to ageing is unpredictable and cannot be eliminated without regular calibration.

	Possibility to measure a wide range of currents	The solutions which propose the sensor's calibration to overcome problems with its sensitivity drift decrease its sensitivity and make the system more complex.
	Small size	
	Good linearity	

This table shows, as mentioned earlier, that although there are many different devices and principles for current measurement, there are still many unsolved problems and challenges that need to be overcome.

3. TRANSMISSION LINE INSIGHTS: FROM CONDUCTORS TO CUTTING-EDGE TRENDS

Overhead lines are air-insulated cables suspended from pylons or poles. The transmission of electrical energy worldwide is primarily based on high-voltage alternating current (HVAC) overhead line technology. Over 98% of the extra high voltage electricity transmission network in the European Union, Norway and Switzerland is of HVAC overhead line construction [42-67]. The main reason for overhead lines being so dominantly used is because they are significantly cheaper than underground cables. However, there are other factors which must be taken into account, such as clearance problems, planning permission, and maintenance requirements.

Climatic conditions of the area where the lines will be placed must be considered in order to choose a conductor with suitable electrical and mechanical characteristics. Especially important for this research is the temperature which influences the conductor current rating and sag. Maximum conductor operating temperature should not exceed 75 °C for bare conductors to prevent annealing of aluminium. Conductor temperatures up to 210 °C are possible with a 'Gap' conductor. [43]

3.1. Selection of conductors for overhead transmission lines

In deciding which cable to choose at a particular voltage level the following criteria are used:

1. The maximum power transfer capability must meet the system requirements.
2. The conductor thermal capacity must be adequate.
3. The conductor diameter or bundle size must be following recognised international standards for radio interference and corona discharge.
4. The conductor must be suitable for the environmental conditions

5. The conductor cross-sectional area should be chosen in such a way as to minimise the initial capital cost (which is higher for large conductors) and to capitalise on the cost of the losses (which are lower for large conductors).
6. The conductor should conform to conductor sizes already used elsewhere on the network to minimise the number of spare conductors. [43]

Copper-based overhead lines are typically used for local distribution because they are too expensive for higher voltage levels. All aluminium conductors (AACs) are also employed at local distribution voltage levels.

Aluminium conductor steel reinforced (ACSR) and all aluminium alloy conductor (AAAC) may be considered for 36 kV transmission and above. Aluminium conductor alloy reinforced (ACAR) and aluminium alloy conductor steel reinforced (AACSR) are less in use than AAAC because they are usually more expensive than ACSR.

ACSR has been widely used throughout history primarily because of its mechanical strength, already developed production capacities and reasonable cost production. It is the most commonly used conductor. A steel core is used for reinforcement of the strength of aluminium, although ACAR cables are being increasingly used where the steel core is replaced by high tensile strength aluminium.

The choice between ACSR and AAAC is not so obvious from a materials point of view. AAAC consists of alloys of Al, Mg and Si. These cables have 10% - 15% less loss than ACSR. [42] When a steel core is used, because of its high permeability and inductance, current flows only in the aluminium strands, thus the cross-section is better utilised in ACAR and AAAC conductors. AAAC becomes especially interesting at larger conductors. Its strength/weight ratio can be very good and in some cases, cable sag can be smaller than ACSR's so lower tower heights can be used. ACSR has better performance regarding long-term creep or relaxation (inelastic stretch or permanent elongation of the material in the direction of the stress when the material is subjected to stress). AAAC is slightly easier to join than ACSR. The characteristics of different conductor materials are given in Table 3.1.

Table 3.1 – Characteristics of different conductor materials [43]

Property	Annealed Copper	Hard-Drawn Copper	Cadmium Copper	Hard-Drawn Aluminium	Aluminium Alloy (BS 3242)	Galvanized Steel
Relative conductivity [%]	100	97 (average)	79.2 (min)	61 (min)	53.5	-
Resistance at 20°C [Ω·mm²/km]	17.241	17.71	21.77	28.26	32.2	-
Density [kg/m³]	8890	8890	8945	2703	2703	7780
Mass [kg/mm²/km]	8.89	8.89	8.945	2.703	2.703	7.78
Coefficient of linear expansion [per °C]	17×10^{-6}	17×10^{-6}	17×10^{-6}	23×10^{-6}	23×10^{-6}	11.5×10^{-6}
Modulus of elasticity [MN/m²]	100×10^{3}	125×10^{3}	125×10^{3}	70×10^{3}	70×10^{3}	200×10^{3}

There are many different types of ACSR cables with many different combinations of steel and aluminium strands. In most cases, the steel strands are placed in the centre of the cable. Typical strandings of ACSR conductors are shown in Figure 3.1.1 and Figure 3.1.2.

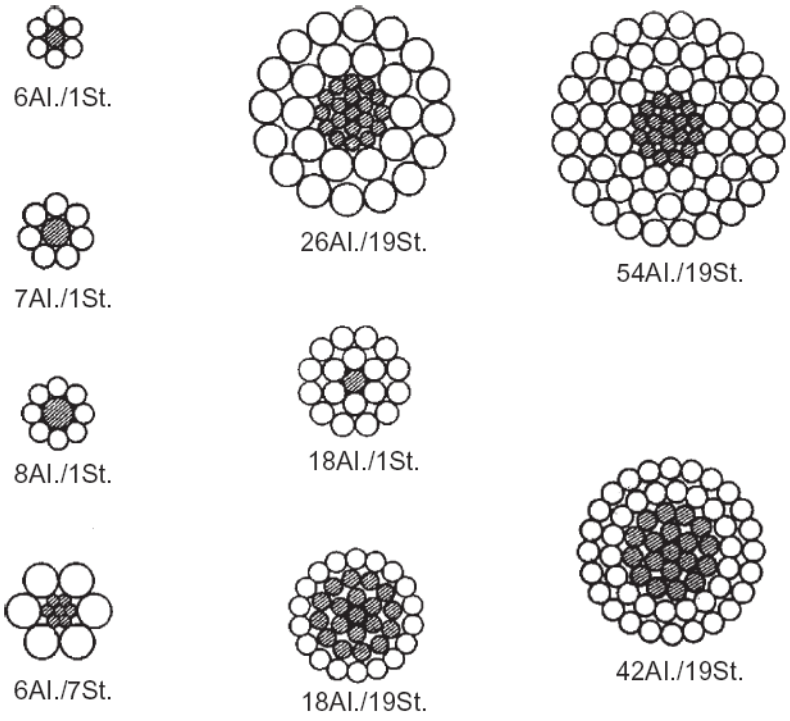

Figure 3.1.1 – Typical stranding of ACSR conductors (part1) [43]

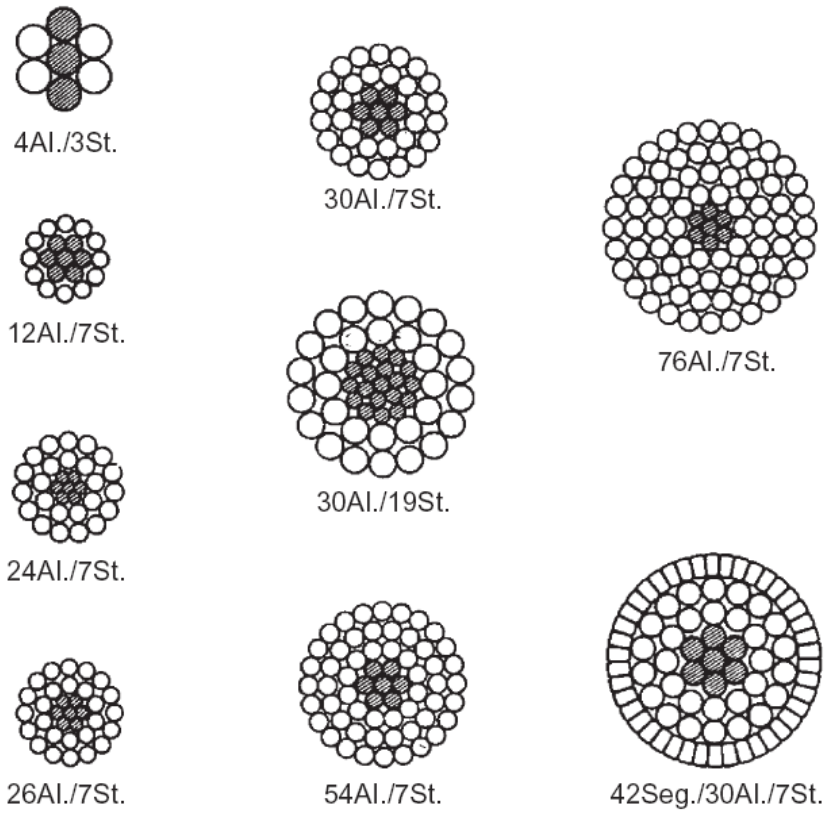

Figure 3.1.2 – Typical stranding of ACSR conductors (part2) [43]

3.2. International standards related to overhead line conductors

The international standards covering most conductor types are:

- IEC 61089 – Conductors for overhead lines – Round wire concentric lay overhead electrical stranded conductors
- EN 50182 – Conductors for overhead lines – Round wire concentric lay stranded conductors (supersedes IEC 61089 for European use)
- EN 50183 – Conductors for overhead lines – Aluminium-magnesium-silicon alloy wires

Other important standards for overhead line cables are:

- IEC 60060-466 – International Electrotechnical Vocabulary (IEV) – Chapter 466: Overhead Lines
- EN 50189 – Conductors for overhead lines – Zinc-coated steel wires
- EN 50326 – Conductors for overhead lines – Characteristics of greases
- EN 60889 Hard-drawn aluminium wire for overhead line conductors
- EN 61232 Aluminium-clad steel wires for electrical purposes

According to standard EN50182, all wires in a stranded conductor should be concentrically stranded. Adjacent wire layers should be stranded in the reverse lay direction. The direction of lay of the external layer shall be right hand except when otherwise specified by the purchaser. The wires shall be evenly and closely stranded around the underlying wire or wires in each layer. The lay ratios for the aluminium layers of all types of conductors need to be as given in Table 3.2.

Table 3.2 – Lay ratios for aluminium layer [44]

All inner Layers		Outer layers	
Min	Max	Min	Max
10	16	10	14

The required lay ratios for zinc-coated or aluminium-clad steel wire layers are presented in Table 3.3.

Table 3.3 – Lay ratios for zinc-coated or aluminium-clad steel layers [44]

Number of steel wires	Lay ratio							
	3 wire layer		6 wire layer		12 wire layer		18 wire layer	
	Min	Max	Min	Max	Min	Max	Min	Max
3	16	26	-	-	-	-	-	-
7	-	-	16	26	-	-	-	-
19	-	-	16	26	14	22	-	-
37	-	-	17	25	16	22	14	18

For zinc-coated or aluminium-clad steel core constructions exceeding 37 wires, the lay ratio of the outer layer shall lie between 14 and 18, and the lay ratio of the inner layers shall lie between 16 and 26. [44]

In a multi-layer conductor, the lay ratio of any layer needs to be equal to or less than the lay ratio of the layer immediately beneath it. Lay ratios used for some calculations in standard EN 50182 can be found in Appendix 1.

Standard EN 50182 has a list of the most common conductors used in Europe and their properties. A list of typical ACSR cables used in the United Kingdom can be seen in Appendix 2. Information about other countries, members of CENELEC (the vast majority of EU countries) and other types of cables used in the United Kingdom can be found in [44].

Table 3.4 – Characteristics of aluminium wires Al1-Al7 recommended for calculations by EN 50183 standard [45]

Density at 20°C	2.70 kg/dm^3
Coefficient of linear expansion	$23 \cdot 10^{-6}$ 1/K
Modulus of elasticity	68,000 N/mm^2

Table 3.5 – Properties of Al2- Al5 wires according to EN 50183 [45]

Type	**Nominal conductivity [% IACS]**	**Nominal diameter [mm]**		**Maximum resistivity [nΩ·m]**	
		Over	**Up to and including**	**Of individual wires**	**Mean of a lot**
AL2	52.50	1.50	3.50	32.84	-
		3.50	5.00	32.84	-
AL3	53.00	1.50	5.00	32.53	-
AL4	52.90	1.50	3.50	32.90	32.60
		3.50	5.00	32.90	32.60
AL5	55.25	1.50	5.00	32.20	31.20
AL6	55.60	1.50	3.50	31.50	31.00
		3.50	5.00	31.50	31.00
AL7	57.50	1.50	2.50	30.50	30.00
		2.50	3.00	30.50	30.00
		3.00	3.50	30.50	30.00
		3.50	4.00	30.50	30.00
		4.00	5.00	30.50	30.00

The standards also recommend the exact values of various conductor properties for calculation purposes for different types of cables. Thus, standard EN 50183 defines the characteristics of aluminium alloy wires (for all different types Al1 - Al7) which are shown in Table 3.4 and Table 3.5.

Historically, there has been no standard nomenclature for overhead line conductors. It led to the situation that the code names for ACSR cables have been used based on animals in the UK and birds in North America. At the same time, AAAC cables were named after insects in the UK and after flowers in North America. The size of a cable cross-sectional area is quoted in circular mils in the United States and Canada (1000 circular mils = 0.507 mm^2).

Standard EN 50182 has defined these codes in Europe while permitting each country to retain the actual different conductor types via the National Normative Aspects. The codes are based on the following rules, described in EN 50182 standard:

- A designation system is used to identify stranded conductors made of aluminium or its alloys with or without steel wires.
- Homogeneous aluminium conductors are designated ALx, where x identifies the type of aluminium. Homogeneous aluminium-clad steel conductors are designated yzSA, where y represents the type of steel (grade A or B, applicable to class 20SA only), and z represents the class of aluminium cladding (20, 21, 30 or 40).
- Composite aluminium/zinc coated steel conductors are designated ALx/STyz, where ALx identifies the external aluminium wires (envelope), and STzy identifies the steel core. In the designation of zinc-coated steel wires, y represents the type of steel (grades 1-6) and z represents the class of zinc coating (A to E).
- Composite aluminium/aluminium-clad steel conductors are designated ALx/yzSA, where ALx identifies the external aluminium wires (envelope), and yzSA identifies the steel core.
- Conductors are identified as follows:
    - A code number giving the nominal area, rounded to an integer, of the aluminium or steel as appropriate

- ❖ A designation identifying the type of wires constituting the conductor, for composite conductors the first description applies to the envelope and the second to the core.

Examples:

16-Al1 – Conductor of AL1 aluminium with an area of 15.9 mm^2, rounded to 16 mm^2.

587-AL2: Conductor of AL2 aluminium with an area of 586.9 mm^2, rounded to 587 mm^2.

401-AL1/28-ST1A – Conductor made of AL1 aluminium wires around a core of ST1A zinc-coated steel wires with a class A zinc coating. The integer area of Al1 is wires is 401 mm^2 and that of the ST1A wires 28 mm^2

401-AL1/28-A20SA – Conductor made of AL1 aluminium wires around a core of Grade A, class 20 aluminium-clad steel wires. The integer area of A20SA wires is 401 mm^2 and that of the ST1A wires 28 mm^2

65-A20SA – Conductor made of Grade A, class 20 aluminium-clad steel wires with an area of 65 mm^2

As mentioned earlier, 'Gap-type' conductors can stand higher temperatures than normal cables. These cables can work in temperatures up to 210 ˚C, depending on the used alloys. [43] Their current-carrying capacity is up to twice that of hard-drawn aluminium.

Their design consists of an extra high strength galvanised steel core, and heat-resistant aluminium alloy outer layers, separated by a gap filled with heat-resistant grease. To maintain the gap, the wires of the inner layer of the aluminium alloy are trapezoid-shaped.

3.3. Power carrying capacity

As mentioned earlier, there are several types of conductors which are used in transmission lines, but ACSR is the one which is the most commonly used at the high voltage (HV) level and above. Although many factors influence a conductor selection at a certain voltage level

in different areas, and the data given in Appendix 3 cannot be considered as the „rules“ in selecting conductors, the presented data can give an idea of ACSR conductor selection. [43]

In practice, the capacity will be limited over long distances by the conductor's natural impedance (voltage regulation) as well as by the conductor's thermal capacity. Depending upon the required electrical load transfer, the number of overhead line conductors of a particular type used per phase may vary.

3.3.1. Conductor configurations

Bundled conductors are almost always used for e.h.v. transmission lines. As an exception to this rule can be mentioned a line in the USA where a special expanded ACSR conductor of 2.5-inch diameter (6.35 cm) has been used for a 525 kV line. [46], [47]

The number of overhead line conductors of a particular type used per phase may vary, depending upon the required electrical load transfer. Several typical conductor configurations are shown in Figure 3.3.1.

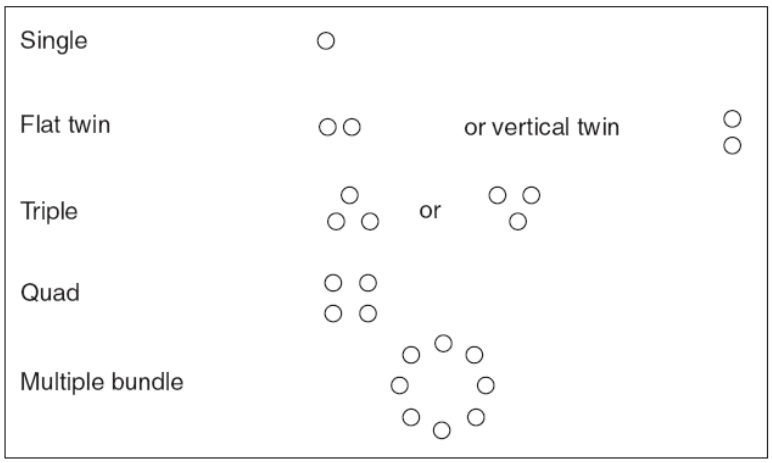

Figure 3.3.1 – Typical configurations of overhead line conductors [43]

The twin conductor has become the most common solution for 400 kV lines, although there are lines such as the Rheinau line in Germany which uses 4 conductors in a bundle in a 4-circuit configuration. A 4-conductor bundle is normally used for 750 kV lines. The conductor radius is in the range of 1.5-1.75 cm, and the current density value in normal operating conditions lies between 0.5 -1 A/mm^2. [48-50]

3.3.2. Line configurations

Very often electricity pylons are designed to carry several electric circuits, especially for HV and EHV. Sometimes the same pylon carries circuits on different voltage levels. Figure 3.3.2 shows several typical examples of line configurations used in various parts of the world.

Double-circuit (D/C) lines are not very common, as single-circuit (S/C) or four-circuit lines. Although one 750 kV circuit can transmit as much power as 4-400 kV circuits, there is a tendency to favour the four-circuit 400 kV lines instead of using the higher voltage level in those countries where technology for this voltage level already exists. For comparison, it should be mentioned that one 1200–kV circuit can carry as much power as three 750 kV lines and twelve 400kV lines for the same distance of transmission. [48,68-72]

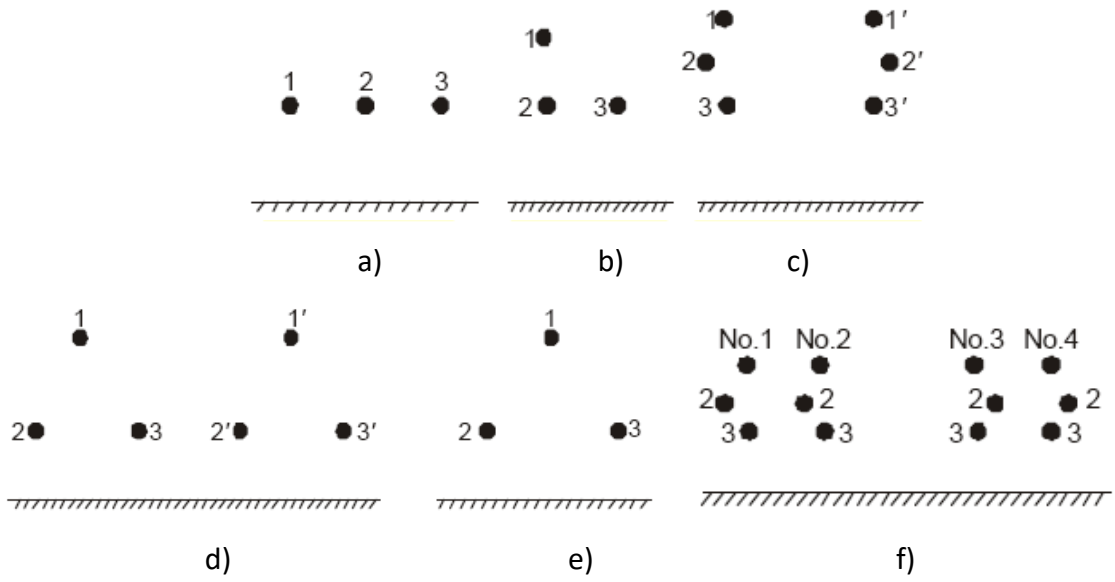

Figure 3.3.2 – EHV typical line configurations a) S/C Horizontal; b) S/C L-Type; c) D/C Conventional; d)D/C Double Triangle; e) S/C Delta; f) Four-Circuit Tower [48]

3.4. Latest trends in the development of transmission lines

The AC transmission system in a range from 35kV to 220 kV are considered high voltage (HV) systems, while extra high voltage (EHV) ranges from 330 to 750 kV. The AC Ultra high voltage systems (UHV), according to the International Electrotechnical Commission (IEC) definition, are rated at 1000 kV and above and the UHV DC system is ±800 kV. [51]

Transmission lines can be built with a different number of subconductors. All of the 765-kV lines built in the 1960s and 1970s have 4 subconductors. There are also some different solutions, for example, although some 750kV lines in Russia have also 4 subconductors, most of them have 5. Some lines have 6 subconductors, such as the Eskom lines which are built at higher altitudes or the line in the Appalachian Mountains in Virginia and the double-circuit low-reactance line built in Korea. The lines built to operate above 1000 kV use 8 subconductors. [49]

Until several years ago, there were no lines in the world operating above 1000kV. The situation has changed today, mostly thanks to Chinese great development and big investments in UHV technology. Today, India has joined them too although the system is still in the test phase. Figure 3.4.1 shows the development of EHV and UHV transmission lines throughout the world from their very beginnings until today.

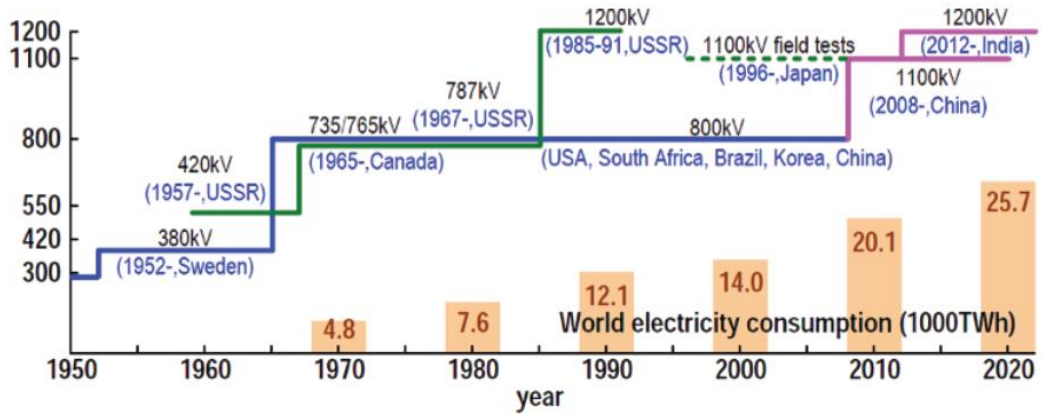

Figure 3.4.1 – Development of EHV and UHV Technology throughout history [51]

In China, the HV AC system includes both 110 kV and 220 kV transmission lines, while the EHV AC lines have various voltages at 330 kV, 500 kV, and 750 kV. [52] China has the plan to build a grid which would be composed of numerous 1200 kV AC and 1100 kV DC lines.

One of these routes, the Jingdongnan-Nanyang-Jingmen UHV AC Demonstration Project, was commissioned in 2009 and is considered to be the first commercially operated 1000 kV line in the world. In addition, the Huannan-Shanghai project became the first commercially operated UHV AC project to transmit double circuits on the same tower in 2013. [51]

India, too, is planning a 1200 kV UHV AC transmission line. Other countries like USA and Brazil are also considering the development of the UHV AC transmission system in their network.

The first 1200kV system was field-tested & commissioned in USSR, but it was discontinued after the disintegration of the USSR. Although Japan started developmental work on the 1100 kV UHV system long before China too, it also still does not have UHV lines as developmental tests are continuing. Japan is planning to upgrade its existing line from 550 kV to 1100 kV.

UHV systems are quite different from EHV transmission networks in terms of topology, conductors, short-circuit power through UHV transformers, line lengths, and insulation coordination.

In 2008, IEC and CIGRE recommended the 1000 kV UHV AC line as the international standard voltage, which IEC approved a year later as the highest voltage for equipment of its type.

4. DEVELOPMENT OF NON-CONVENTIONAL INSTRUMENT TRANSFORMERS USING SMART MATERIALS

The main idea of this research topic is to suggest a new solution for electrical current measurement using a new type of material called magnetic shape memory (MSM) alloys. There have been some attempts to use some very interesting properties of these materials for several applications, but there are no suggestions to use them for current measurements. The focus of this chapter will be on MSM materials and the proposed measurement solution.

4.1. MSM materials

Magnetic shape memory (MSM) alloys are relatively new 'smart' materials which change their shape when subjected to external magnetic fields. They belong to the group of ferromagnetic materials, so they are also called ferromagnetic shape memory alloys. There are several alloys which exhibit a similar effect, but the Ni-Mn-Ga alloys are by far the most studied and the most promising MSM alloys which have been shown to have enormous potential to be used in actuators and sensors.

MSM alloys have a remarkable magnetic field-induced strain, the maximum theoretical value of which varies, depending on the material's microstructure from 6% for the most studied five-layered modulated (5M) to 12% for non-modulated structures [73], [74]. These are more than one order of magnitude higher than maximum strains produced by conventional magnetostrictive (e.g. Terfenol-D) and piezoelectric materials, reaching the strains of well-known thermal shape memory alloys (SMAs). However, unlike thermal shape memory alloys, MSM alloys do not involve a phase transformation so their response to magnetic field excitation is significantly faster and they have a very long fatigue life. As it is obvious from their reversible properties, MSM alloys can be used as both position and stress sensors [75]. Since 5M MSM alloys have the lowest twinning stress and high mobility of twin boundaries

they are the best choice for these applications. The meaning of twinning stress and twin boundaries will be explained in more detail later in this chapter.

It is interesting to compare some of the properties of MSM alloys (MSMA) and other conventional materials. This is shown in Table 4.1

Table 4.1 – Comparison of MSM alloys and other conventional materials

	Piezoelectric (PZT)	Magnetostrictive (Terf.-D)	SMA (NiTi)	MSMA (Ni-Mn-Ga)
Control mode	Electric	magnetic	heat	magnetic
Max strain [%]	0.1 – 0.6	0.15 - 0.2	2 – 8	6 – 10
Blocking stress (MPa)	100	70	250	3
Response time	µs	ms	s	ms

MSM alloys belong to the group of ferromagnetic materials. Although ferromagnetic materials change their shape when exposed to the magnetic field due to magnetostriction, the main reason for the strain of MSM materials is a variant reorientation. It has been shown that the effect of magnetostriction is so small in comparison to variant reorientation that it can be neglected [76].

It is worth it to mention that due to the larger strain range, MSM alloys can be used in applications where GMM materials are not adequate. For instance, a typical 20mm MSM element with 5M microstructure elongates by up to 1.2mm under no larger than 0.6T magnetic field if the mechanical load is small [77].

To summarise, the main attributes of MSM materials are:

- Large stroke, *nm* precisely controlled
- Microsecond response time
- Wide operation frequency range

- High fatigue capabilities
- Complicated shape changes in a magnetic field

These properties suggest that MSM alloys could be better candidates for NCIT than other, above mentioned magnetic materials.

4.2. Operation of MSM materials

The change of shape of an MSM element in a magnetic field occurs due to inequality in lattice parameters coupled with magnetic anisotropy of the crystal [78]. An MSM element is formed of multiple parts with different orientations of the crystallographic *c* axis (also called the 'easy' magnetisation axis). These parts are called twin variants. There are two types of variants: 'easy' and 'hard' variants (Figure 4.2.1). Variants which have their 'easy' axes aligned with the applied magnetic field are called 'easy' variants, while in 'hard' variants these axes are transverse to the applied magnetic field.

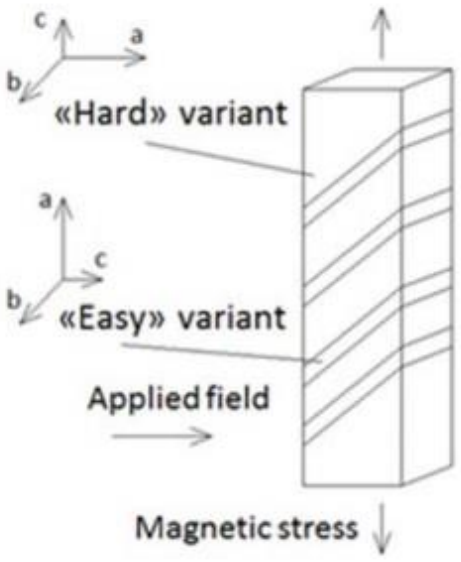

Figure 4.2.1 – Orientation of crystallographic axes in twin variants of MSM element [79]

A short crystallographic *c* axis tends to align with the applied magnetic field which leads to local reorientation of the crystal. [80] The other two crystallographic axes, *a* and *b* (also

called 'hard' magnetisation axes) are longer than the *c* axis, so the local reorientation of the crystal results in overall elongation or contraction of the MSM element. Figure 4.2.1 shows the case when the MSM element would elongate for the presented direction of the magnetic field. When MSM elements are considered it is usually said that they possess a 'hard plane' and an 'easy axis' of magnetisation, and only the behaviour of the *a*-*c* plane is commonly of interest since reorientation happens in this plane.

The operation of an MSM element can be seen in Figure 4.2.2. The parts a), b) and c) in Figure 4.2.2 show the process of elongation of the MSM element from its initial stage when it consists of only hard variants to its full elongation after the field was applied transversely. The parts d), e) and f) of the same figure show the process of the MSM element's return to its initial stage by applying the field along the element or by using compression force.

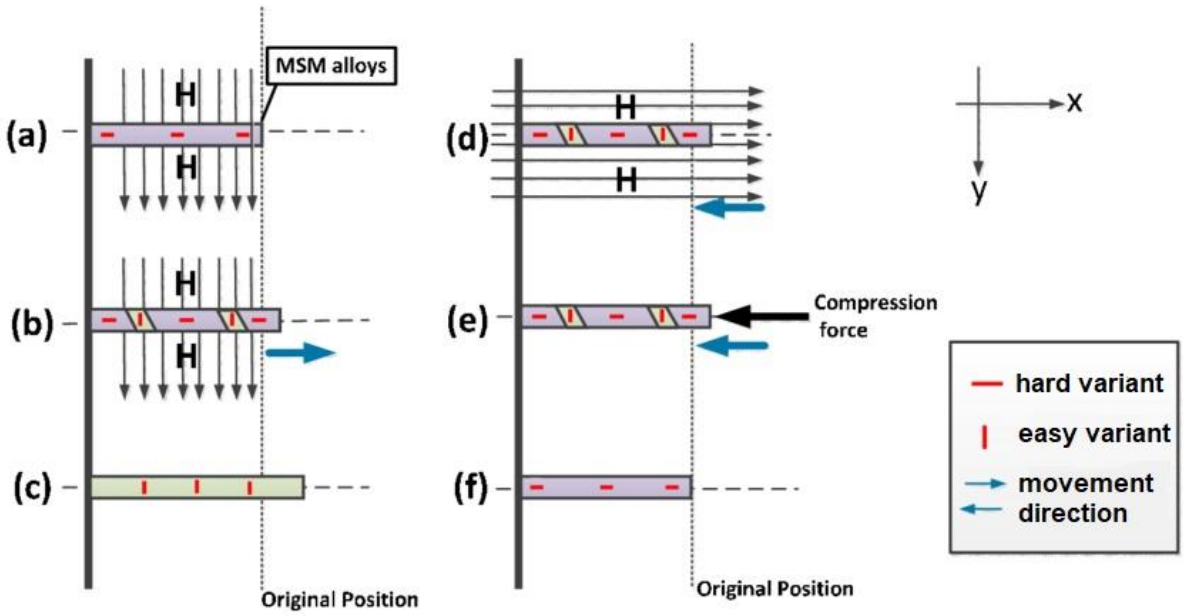

Figure 4.2.2 – Operation of an MSM element [81]

As the intensity of the applied magnetic field increases, 'easy' variants grow and expand at expense of 'hard' variants. This process will last until only one type of variant exist in an MSM element [73]. This means, that elongation is possible while 'hard' variants exist in the element. The elongation of MSM elements will stop depending on the strength of the magnetic field. When the magnetic field is turned off or is not strong enough to turn more hard variants into easy variants, the MSM element retains the length of its elongation. The

field is usually applied transverse to the longest side of an MSM element in order to elongate it as shown in Figure 4.2.1.

On the other hand, if the magnetic field is applied along the length of the MSM element, the element will contract. Another way to contract the MSM element is to apply compression force on it. By using any of these two ways, it is possible to return the MSM element to its original shape if the magnetic field or compressive force is strong enough. During this process, easy variants are turning into hard variants.

MSM materials have the tetragonal lattice in the low-temperature martensite phase and the cubic lattice in the high-temperature austenite phase. The main reason for the change of the shape of MSM materials is a lattice distortion in the low-temperature martensite phase, so the temperature is one of the limiting factors when these materials can be used. As Curie's temperature of MSM materials is higher than the transformation phase temperature in available Ni-Mn-Ga alloys, only the latter should be considered. This temperature is in the range of 60-80˚C [82].

Although using MSM alloys above their martensite-austenite transformation temperature is not of interest for this research because they lose many of the above-mentioned properties, it is worth it to mention that they can be used as conventional SMA materials if the shape change during the phase transformation is utilised. If they are used in this way, the shape change occurs at a particular (phase transformation) temperature, unlike gradual straining due to the twinning stress change.

4.3. Characteristics of MSM materials

One of the most important properties of MSM alloys for this research is the value of the magnetic field which will trigger the elongation of MSM material. Twin variants start to reorient when the magnetic field exceeds a certain threshold. This threshold is characterised by the minimum value of the external stress or magnetic field required to overcome the twinning stress of a crystal and to initiate reorientation. The minimum value of the magnetic field is known as a switching field.

When an MSM element is not elongated it consists only of hard variants and its relative magnetic permeability in this situation is μ_r = 2. When the MSM element is fully elongated it consists of only easy variants and its relative magnetic permeability is μ_r = 50 in that case. It should also be mentioned that the values of relative magnetic permeability are different for 'easy' and 'hard' axes. While different researches have reported different values for 'easy' axes, the value of relative magnetic permeability for 'hard' axes has been consistently reported as 2. This value for 'easy' axes has been reported in the range of 40 to 210, depending on the MSM alloy [79]. In our research, it is assumed to be equal to 50 which corresponds to the data published on the official website of the manufacturer of MSM alloys, ETO MAGNETIC [83].

Figure 4.3.1 shows the elongation curves obtained by this manufacturer. [83] MSM crystals have a different strain-magnetic field relationship at different pre-stress levels (loads). The best option for our NCIT application would be MSM elements which follow the curve at a load of 0.5 N/mm^2 (the dark blue curve). This curve has the lowest threshold for triggering the MSM element (reversibly) under a magnetic field and it has the largest strain. The black curve does not have a return branch and the other curves, although return to their original state (unlike the dark blue one), need high values of the magnetic fields to be triggered. Furthermore, the ones with a load over 2 N/mm^2 are not able to reach the full strain.

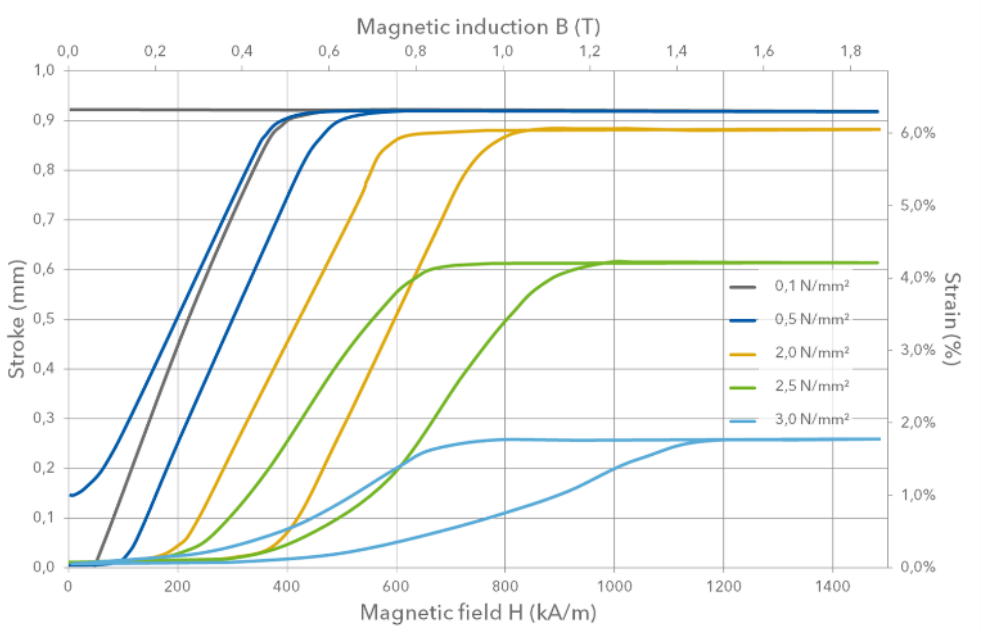

Figure 4.3.1 – Strain-magnetic field relation for the ETO MAGNETIC MSM crystals at different pre-stress (load) levels [83]

The MSM element following the dark blue curve would be triggered in this case by an approximately 0.085 T magnetic field, but higher values of the field are needed so that the MSM element starts to elongate linearly. The maximum value of the applied field before the material reaches saturation point is around B = 0.5T. Therefore, Figure 4.3.1 shows that the MSM element will react to external magnetic field excitation in the range of B = 0.085 - 0.5 T.

4.4. Novel sensing principle based on MSM 'smart alloys'

The basic principle of a novel current sensor based on MSM alloys, proposed in this research relies upon the proportionality of the strain produced by an MSM element which is subjected to a magnetic field produced by the current whose magnitude is being measured. This is shown schematically in Figure 4.4.1 in which the output voltage, V generated by the linear variable differential transformer (LVDT) is proportional to the strain, ε produced by the MSM element. This MSM strain is, in turn, proportional to the magnetic field B which is ultimately proportional to the current in the conductor, I (measurand).

Figure 4.4.1 – Schematic showing the proposed current measurement system based on magnetic shape memory (MSM) alloys [84]

The sensor system consists of an MSM element and a suitably coupled LVDT. The magnetic field (B) produced by a current (I) in the conductor is converted into the displacement of the MSM element (ε) which changes the output voltage (V) of the LDVT. This approach allows sensing very high currents remotely essentially by sensing the magnetic field produced by these currents.

The main disadvantages of the proposed MSM-based current sensors are attributable to temperature sensitivity and magneto-mechanical hysteresis of currently available MSM

alloys. The former is associated with the upper-temperature limit determined by the martensite – austenite transformation temperature of 60-80˚C for conventional alloys and by the temperature-dependent twinning stress, as was mentioned above. The hysteresis is also associated with this twinning stress. The twinning stress can be seen as an energy barrier to be overcome for propagating twin boundaries in the MSM material and hence, changing the shape of the MSM element. Consequently, the sensitivity of the proposed sensor is inversely proportional to the magnitude of the twinning stress. Twinning stress is still considerably high for conventional MSM materials with type I twin boundaries. However, less studied, MSM materials with type II twin boundaries can be very promising for sensor applications due to low twinning stress which does not depend on temperature [85]. This results in very low hysteresis together with good temperature stability. The lowest type II twinning stress of 0.01 MPa and corresponding switching field of only 30mT were reported in [86]. This means that it will be required a much smaller value of the electromagnetic field to trigger the shape change of MSM stick if material with twin boundary type II instead of twin boundary type I is used. As the research on MSM alloys with type II twin boundary type is a very intense ongoing process and a lot of attention is paid to it, the biggest problem at the moment is twin microstructure instability. [87]

Our initial research that will be presented later in Chapter 5 has shown that the MSM element is not sensitive enough to be used by itself for the measurement of AC in high voltage overhead transmission lines in the normal working regime. That was a motivation for adding a magnetic circuit to the NCIT's design, to collect as much of the magnetic field around the current-carrying conductor and focus it towards the MSM element.

This modified schematic of the proposed NCIT can be seen in Figure 4.4.2.

Figure 4.4.2 – Schematic showing the proposed current-measurement system based on (MSM) alloys (with concentrator)

More details about the above-mentioned magnetic circuit will be given in Chapter 5.4.

4.5. LVDT

4.5.1. Principle of operation of LVDT

The linear variable differential transformer (LVDT) is one of the most widely used transducers for measuring linear displacement. Its output is a direct and linear function of its input. There are two types of them: “AC-LVDTs” and “DC-LVDTs”. Due to their working principle, they are AC-in/AC-out devices, but it is possible to make them DC-in/DC-out devices by adding electronic parts.

LVDT like any other transformer consists of a primary coil, secondary coils and a magnetic core (Figure 4.5.1). The central coil is the primary coil and the other two are identical secondary coils which are connected in series in such a way that their outputs oppose each other. The object in which translational displacement needs to be measured is attached to the central iron core of the transformer. In that way, all body motions are transferred to the core.

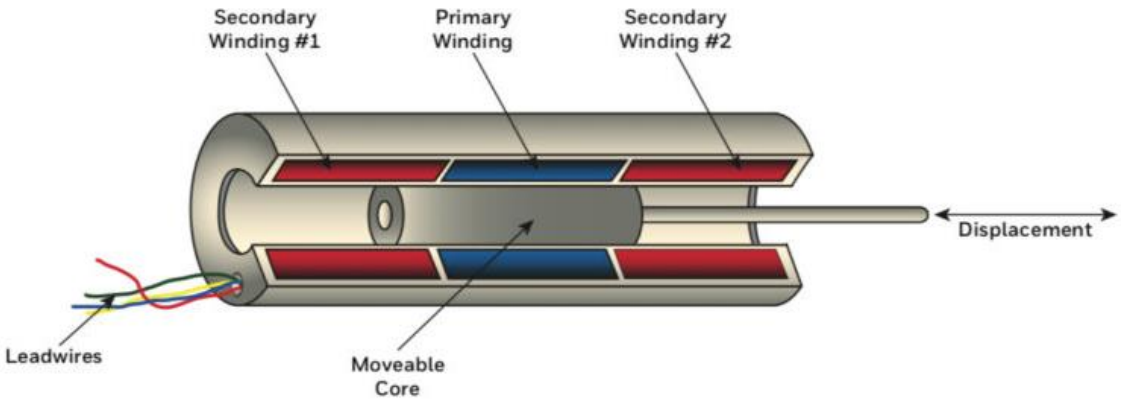

Figure 4.5.1 - Operation of LVDT [88]

When the primary coil is energized with constant amplitude AC, the electromotive force is induced in the secondary coils. If the magnetic core is in the central position, the equal parts of it are in each of the secondary coils and thus the same amount of electromotive force is induced in each of the coils. Since they are connected in a way that their outputs oppose

each other, the net output is zero. However, when the core is displaced from the central position there is a greater amount of magnetic core in one of the coils. This results in unbalanced values of electromotive forces induced in two secondary coils and causes a non-zero output. The bigger the core's displacement is, the bigger the difference between the two electromotive forces, and thus the absolute value of LVDT's output increases. The signal output has a linear relationship with the actual mechanical movement of the core.

Additionally, the secondary output signal can be processed in a demodulator (which is switched at the same frequency as the primary energizing supply). In this way, it is possible to provide a DC output proportional to the core movement and also indicate its direction, positive or negative, from the central zero point.

The advantage of using an LVDT displacement transducer is that the moving core does not make contact with other electrical components of the assembly, thus offering high reliability and long life. LVDTs have excellent resolution, good repeatability and in theory infinite mechanical life. It can be made suitable for operation in corrosive environments and it is insensitive to mechanical shock and vibration.

Some problems that affect the accuracy of the LVDT are the presence of higher harmonics in the excitation voltage and stray capacitances. Furthermore, it is also impossible in practice to produce two identical secondary windings. All of this can cause a nonzero null output, but its magnitude is always less than 1% of the full-scale output and often is of little consequence. [89] Where necessary, this inaccuracy can be measured by applying known displacements to the instrument and appropriate compensation can be applied then to subsequent measurements.

4.5.2. Characteristics of LVDT

There are several factors important to consider when selecting LVDT. One of the most important ones is the maximum range of core motion. The core can be displaced from null toward either end. A distance that the core can travel from its null position to one of the ends is called full-scale displacement and it is stated with ± sign. When it is stated without a

polarity, it is called the LVDT's full range, full stroke, or total stroke. Commercially available LVDTs can be used to measure displacement in the range from ±100 µm to ±500 mm. [89], [90]

Another important parameter is the resolution of LVDT. That is the smallest core position change that can be observed in LVDT output. Since LVDT's work principle is based on magnetic coupling, its resolution is essentially infinite. An infinitesimal change in core position will produce an output change, but in practice, there are certain limitations on system resolution. The resolution depends on the ability of the associated electronic equipment to sense the change in LVDT output, which is called the signal-to-noise ratio of the system.

As mentioned earlier, there are two types of LVDTS: AC and DC. The AC LVDT can tolerate extreme variations in operating temperature which is not the case with DC LVDTs. DC LVDTs usually have an oscillator, carrier amplifier and demodulator circuitry. Due to the presence of these electronic components, their temperature operating range is typically from -40°C to 120°C.

LVDTs are usually excited by AC voltage of the frequency between 50 Hz and 25 kHz with 2.5 kHz taken as a nominal value. This frequency is usually selected to be at least 10 times greater than the highest expected frequency of the core motion. There are two ways how the sensor is attached to the moving part. It is either a fixed mechanical interface or a spring-biased probe that follows the moving surface.

For the application of our sensor, an especially important parameter is the supply requirement to the sensor because the proposed NCIT should be operating in overhead transmission lines where supply options are very limited. Most LVDTs operate on values within the range of 5V DC to 30V DC.

The output from LVDT can be DCV, ACV, DCmA or a range of digital signals. The best way to compare different LVDTs is through their sensitivity (for AC-LVDTs) and scale factor (for DC-LVDTs). Sensitivity is usually specified in terms of mV output per mm core displacement per Volt of excitation (mV/mm/Volt). Sensitivity varies with excitation frequency, which is also always specified. The scale factor is usually expressed as Volts DC output per mm of core

displacement. DC-LVDTs with outputs into a 4-20mA current loop can also be found, so their scale factors are expressed as mA/mm.

Typical non-linearity errors of LVDTs are ±0.25% of the full range, but the errors of just ±0.05% of full range output are possible to achieve. Temperature sensitivity is ±0.01% of the full range. [89], [90]

5. MODELLING AND DESIGN OF NON-CONVENTIONAL INSTRUMENT TRANSFORMERS AND HIGH VOLTAGE CONDUCTORS

In the previous chapter, the working principle of the proposed new current sensor and the main characteristics of MSM alloys which should be used as a sensing part of the new sensor have been presented. Chapter 3 explains in detail what types of conductors are used in overhead transmission lines as well as their properties. Many of the conclusions and properties mentioned earlier are used during the modelling which is done in the software ANSYS APDL and will be presented in this chapter.

Two approaches in computing electromagnetic problems will be discussed in this chapter - analytical and using the Finite Element Method (FEM). Some physical phenomena important for this research, such as skin and proximity effect, will be explained. The focus of this chapter is on the modelling procedures and the obtained results. There are two important parts of these modelling procedures which are going to be presented in this chapter. The first one is a very flexible 2D solution which allows the calculation of the magnetic field around almost any conductor used in overhead lines. The values of the magnetic field around the conductors are essential information to make any conclusions about the proposed current sensor. The second part involves modelling and obtaining results when an MSM element is placed near the conductor.

Due to the axial symmetry exhibited by the proposed magnetic circuit and the current carrying conductor, the electromagnetic field remains consistent in the x-y plane when considering a 2D analysis around the conductor.

Additionally, given the very small size of the airgap (0.1 mm as described in Chapter 5.4.4), it is reasonable to assume that the flux lines will follow the path from the magnetic circuit's poles, through the airgap, to the MSM element. Any alternative path would result in longer flux lines and higher reluctance. This assumption holds particularly true for non-saturated magnetic circuits, which is the case in our research as none of the observed currents lead to saturation within the considered range.

As a result, by utilizing a 2D cross-sectional representation, we can simplify the problem's complexity, eliminating the need for 3D modeling while still maintaining accurate results.

5.1. Background electromagnetic field theory

Maxwell's equations are a set of partial differential equations which can be used to describe all electromagnetic processes on a macroscopic level. They relate the electric and magnetic fields to each other and to electric charges and currents. Like any differential equation, to obtain a unique solution, it is necessary to define the initial and the boundary conditions. These equations can be written as follows:

$$\nabla \times \boldsymbol{B} = \mu_0(\boldsymbol{J} + \varepsilon_0 \frac{\partial \boldsymbol{E}}{\partial t}) \tag{5.1}$$

$$\nabla \times \boldsymbol{E} = -\frac{\partial \boldsymbol{B}}{\partial t} \tag{5.2}$$

$$\nabla \cdot \boldsymbol{E} = \frac{\rho}{\varepsilon_0} \tag{5.3}$$

$$\nabla \cdot \boldsymbol{B} = 0 \tag{5.4}$$

where ***E*** is the electric field intensity [V/m], ***B*** is magnetic flux density [T], ***J*** is current density [A/m^2], ρ is the electric charge density [C/m^3], $\varepsilon_0 = 8.85 \cdot 10^{12}\ F/m$ is free space permittivity and $\mu_0 = 4\pi \cdot 10^{-7}\ \mathrm{H/m}$ is free space permeability. $\nabla \cdot$ is the divergence operator and $\nabla \times$ is the curl operator.

The first equation is also known as Ampere's Law with Maxwell's addition and the second one as Faraday's Law. The last two equations represent Gauss's Law in electrical form and Gauss's Law for magnetism, respectively.

In addition to these four equations, two more equations are usually added, known as constitutive relations. They specify relations between displacement field ***D*** and electric field ***E***, as well as the magnetic field strength ***H*** and magnetic flux density ***B***. They can be written as:

$$\boldsymbol{D} = \varepsilon_r \varepsilon_0 \boldsymbol{E} \tag{5.5}$$

$$\boldsymbol{B} = \mu_r \mu_0 \boldsymbol{H} \tag{5.6}$$

where ε_r and μ_r are relative permittivity and relative permeability, respectively.

Equation 5.6 is especially important in dealing with magnetic materials. Ferromagnetic materials have relative permeability $\mu_r > 1$, and moreover, they are dependent on the values of magnetic field ***H*** and temperature. Thus, B-H curves usually need to be taken into consideration in these cases.

Very often, electromagnetic problems are rather complicated using Maxwell's equations (especially if the problems are not symmetric). Finite element methods (FEM) is usually used to solve problems in these situations.

It should be noted that Maxwell's equations successfully describe a variety of phenomena on a macroscopic level, but they cannot explain or predict certain effects (for example photoelectric effect, Planck's law, phenomena in quantum mechanics etc.) which are not of interest in this research.

In problems that involve time-varying current, which is exactly the case in this research, frequency-dependent processes should be considered.

A time-invariant current in homogeneous cylindrical conductors is distributed uniformly over the whole cross-section. That is not the case with time-varying currents which tend to concentrate near the conductor surfaces. If the frequency is very high, the current flows only along a very thin layer near the conductor's surface. This phenomenon is known as the skin effect.

As a result of this, the diameter of the conductor is effectively reduced and thus, its resistivity is increased. This is a reason why the AC resistance of conductors is always higher than their DC resistance. Skin effect is the reason why a transfer of high currents even at the power line frequencies is not efficient through thick, solid conductors. In these cases, as it is explained in Chapter 3, bundled conductors are used instead.

A skin depth is a parameter which is used to describe a level of skin effect. Skin depth is the distance measured from the conductor's surface at which the amplitude of current density decreases to 1/e (approximately to 37%) of its value at the surface. It can be calculated using the following equation:

$$\delta = \frac{1}{\sqrt{\pi f \mu \sigma}} \tag{5.7}$$

where f is a frequency of supply current [Hz], $\mu = \mu_r \mu_0$ is absolute relative permeability $[\mathrm{H/m}]$ and σ is conductor's conductivity [S/m].

Equation 5.7 is valid for current distribution in any homogenous conductor with a radius of curvature much larger than the skin depth. It can be used at frequencies much below 1/(ρε) which is ensured for conductors at least up to microwave frequencies (ρ and ε are resistivity and permittivity of the conductor, respectively).

Stranded conductors are not homogenous conductors as there are inevitably spaces between the strands filled with air or grease. As a result, the skin depth will be higher in this case than can be calculated using Equation 5.7, thus the current will flow through a larger cross-section than in a solid conductor of the same material at the same frequency. Time-varying magnetic fields also exhibit the skin effect. FEM can be used to get current distribution in these cases.

Another effect that should be mentioned is the proximity effect. A time-varying current in one conductor influences the current distribution in nearby conductors. This phenomenon is known as the proximity effect. Both skin effect and proximity effect, are consequences of electromagnetic induction. The analysis of the proximity effect, especially when it is combined with the skin effect, is rather complicated.

5.2. Finite Element Method (FEM) approach in modelling magnetic fields

There are many practical engineering problems for which we cannot obtain exact solutions or it is very difficult to do that. The finite element method is a numerical technique that can be used to obtain solutions to various engineering problems, such as electromagnetism, stress analysis, heat transfer and fluid flow. The results obtained using this approach are approximate solutions for systems of differential equations for certain boundary conditions.

As it was mentioned earlier, solving many electromagnetic problems can be rather complicated using Maxwell's equations without making some simplifications and assumptions and very often that cannot be done in real-life problems. Current distribution is possible to predict and accurately calculate for a single solid conductor but in the case of stranded conductors that is not possible, especially having in mind the influence of skin and proximity effect on current distribution inside conductors. Furthermore, the conductors used in high voltage overhead lines have strands wrapped around the central strand, in the opposite lay direction in each adjacent level, which makes geometry and calculations even more complicated. [91-93]

Different FEM programs are available on the market. ANSYS Multiphysics software package is used during this research, although the basic principle of how FEM programs operate is the same for all of them.

In contrast to analytical solutions, which show the exact behaviour of a system at any point within the system, numerical solutions provide solutions only at certain points in the system. These points are called nodes. A complex domain is divided into simple subdomains which are called elements. A mesh of the model is obtained this way. Equations for the elements can be written in a simpler form which is very useful, especially for problems which include complex geometry or nonlinear material properties.

The accuracy of the solutions obtained depends on the number and size of the elements. By increasing the number of elements and thus having a finer mesh of the model, the accuracy of the solution increases. However, this process increases the computational time and

resources needed to perform these calculations. No matter how fine the mesh of the model is, errors called discretisation errors can never be fully eliminated.

The typical approach to solving this problem is to find a compromise between the number of elements in the model and the computational time needed to obtain a solution. This is done by refining the mesh in the critical areas (or areas of particular interest) and having somewhat less fine mesh in other areas.

Applying loads means choosing a relevant source of excitation for the considered model. Loads that can be applied in solving electromagnetic problems are: current, current density, voltage, and coercive force (for permanent magnets).

To obtain a solution to a magnetic field problem, and to solve Maxwell's equations using FEM, two types of magnetic potential formulation are used. They are scalar potential ψ and magnetic vector potential A. Electric scalar potential ϕ is also used. All other parameters are derived from them. Magnetic and electric field equations using these potentials can be written as follows [94]:

$$\boldsymbol{B} = \nabla \times \boldsymbol{A} \tag{5.8}$$

$$\boldsymbol{H} = -\nabla \psi \tag{5.9}$$

$$\boldsymbol{E} = -\nabla \phi - \frac{\partial \boldsymbol{A}}{\partial t} \tag{5.10}$$

A, ψ and ϕ are the degrees of freedom (DOF) used by the ANSYS solver.

The choice of potential that is going to be used is based on several factors such as field dynamics, field dimensionality, source current configuration, domain size and discretization. The vector potential method is used for solving 2D problems, thus it was used so far in this research. Since harmonic analysis is done in this research due to the nature of the considered problem, it is important to mention that the harmonic analysis in the ANSYS software package provides two sets of solutions – the real and the imaginary component of a complex solution. [95]

The magnitudes of the real and imaginary sets describe the measurable field at $t = 0$ and $\omega t = -90$ degrees, respectively. That means that to obtain amplitude $a(r)$ and phase angle $\varphi(r)$ of the measurable harmonic function $\boldsymbol{Q}(\boldsymbol{r})$ (for example, magnetic flux density $\boldsymbol{B}$ or current density $\boldsymbol{J}$), the following calculations are necessary to perform during the postprocessing process:

$$\boldsymbol{a}(\boldsymbol{r})^2 = \boldsymbol{Q_r}(\boldsymbol{r})^2 + \boldsymbol{Q_i}(\boldsymbol{r})^2 \tag{5.11}$$

$$\boldsymbol{tan}\big(\boldsymbol{\varphi}(\boldsymbol{r})\big) = \boldsymbol{Q_i}(\boldsymbol{r})/\boldsymbol{Q_r}(\boldsymbol{r}) \tag{5.12}$$

where $\boldsymbol{Q_r}(\boldsymbol{r})$ and $\boldsymbol{Q_i}(\boldsymbol{r})$ are the real and imaginary parts of the complex function $\boldsymbol{Q}(\boldsymbol{r})$, respectively i.e.:

$$\boldsymbol{Q}(\boldsymbol{r}) = \boldsymbol{Q_r}(\boldsymbol{r}) + \boldsymbol{j}\boldsymbol{Q_i}(\boldsymbol{r}) \tag{5.13}$$

The basic magnetic analysis results are: magnetic field intensity, magnetic flux density, magnetic forces and current densities. The basic electric analysis results include electric field intensity, electric current densities, electric flux density, Joule heat and stored electric energy. [95] The magnetic flux density is the first derived result (it is defined as the curl of the magnetic vector potential). Magnetic field intensity is derived from the flux density.

Any FEM analysis requires specified boundary conditions for the outer boundaries of the model as an unconstrained field problem can have an infinite number of solutions. Boundary conditions can also be used to take into consideration the surrounding environment which is not necessarily included in the model. The two most common types of boundary conditions are Dirichlet (or first-type) and Neumann (or second-type) boundary conditions.

Dirichlet boundary condition specifies the values that a solution of an ordinary or partial differential equation needs to take along the outer boundary. For magnetic vector potential, it can be written as:

$$\boldsymbol{A} = 0 \tag{5.14}$$

On the other hand, the Neumann boundary condition specifies the values that the derivative of a solution of an ordinary or partial differential equation needs to take along the outer boundary. This condition, in the case of the magnetic vector potential, is:

$$\frac{d\boldsymbol{A}}{dn} = 0 \tag{5.15}$$

The above-mentioned FEM approach was important to consider and take into account for modelling of NCIT what will be discussed in details in the following chapters.

5.3. Modelling of high voltage transmission lines

As was explained in Chapter 3, Aluminium Conductor Steel Reinforced (ACSR) and All Aluminium Alloy Conductor (AAAC) are dominantly used in overhead transmission lines. This was a reason why special attention was given to those two types of conductors, although the model can be used also for All Aluminium Conductors (AAC) as well as for Aluminium Conductor Alloy Reinforced (ACAR).

5.3.1. Capabilities of the developed model

As a part of developing a model of high voltage conductors, a program that can analyse various phenomena and simulate almost any type of conductors used in overhead transmission lines was developed. More specifically, those conductors are:

- ACSR
- AAAC
- AAC
- ACAR

The user needs only to enter the number of aluminium and steel strands of a chosen conductor, their diameters, and the program will plot the geometry and produce the full model of the conductor (Figure 5.3.1). The number of strands for different types of conductors and their diameters can be found in standard EN 50182. [44]

The full analysis can be done for a range of current values and frequencies which the user can enter at the start of the program.

In the current version of this program, the resistivity of the aluminium alloys is entered in the code, so that is something that needs to be manually changed for AAAC and ACAR conductors before starting the program. By default, the program produces a model of ACSR conductor 528-Al1/69-ST1A for the amplitude current of 1000A and 50Hz.

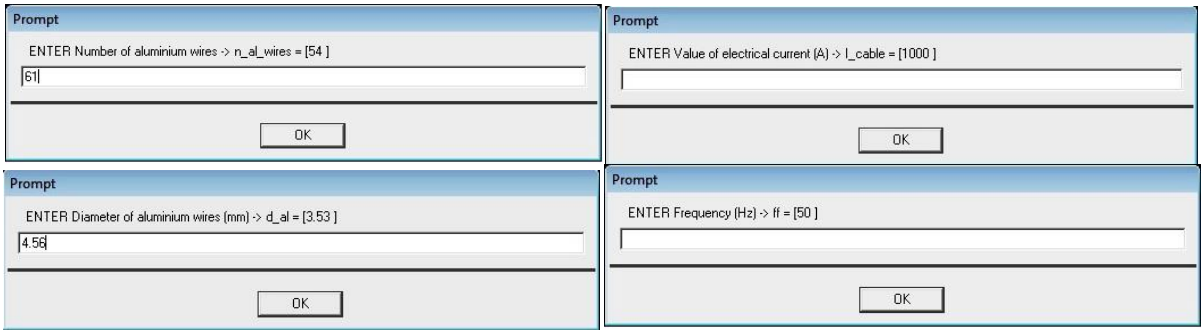

Figure 5.3.1 – Program interface – information that the user enters at the start of the program developed for modelling high voltage conductors

The obtained results and discussion of these results for several conductors will be given later in this chapter. This model was also used as the base for modelling the NCIT and producing various designs of magnetic concentrators as described in Section 5.4

5.3.2. Setting up the material properties of the model

ACSR and AAAC conductors, as the most commonly used type of conductors for high voltage, extra high voltage and ultra-high voltage overhead transmission lines, will be used as

examples in this section. Similar examples and results can be easily obtained for other types of conductors by only changing material properties.

Several international standards specify the exact values of some material properties which should be taken into account for calculation purposes. On the other hand, the same standards specify not exact, but the maximum value of resistivity at 20˚C for different materials. These values are given in Table 3.4 and Table 3.5 for aluminium alloys conductors (Al2-Al7). For hard-drawn aluminium (Al1), these values can be seen in Table 3.1.

Although in some cases aluminium-clad steel can be used as a conductor reinforcement, normally, galvanised (zinc-coated) steel is used. This is the reason why the characteristics of zinc-coated steel are taken for this model as it is defined in standard EN 50189.

During this research, a conductor for overhead transmission lines having an ampacity higher than 2.5 kA has not been found. As mentioned earlier, current density value in normal working regime lies between 0.5 A/mm^2 and 1 A/mm^2 and conductor radii are in the range from 1.5-1.75 cm. [44], [45], [49], [50], [63], [65],[96]
As an example are chosen two conductors (an ACSR and an AAAC conductor) that have the highest current ratings of all the conductors used in the UK. [45] These two conductors are also one of the most used conductors in the EU for carrying high currents. The chosen ACSR conductor is 528-Al1/69-ST1A and the AAAC one is 996-AL5.

Table 5.1 – Parameters used to model 528-Al1/69-ST1A conductor (MOOSE) [63], [65]

	Number of strands	Diameter of a strand [mm]	Conductivity [S/m]	Relative magnetic permeability	Diameter of core [mm]	Total diameter [mm]	Total area [mm^2]
Zinc coated steel	7	3.53	$5.21 \cdot 10^6$	100	10.6		
Al1 (hard drawn aluminium)	54	3.53	$3.54 \cdot 10^7$	1			
Total	61					31.8	597

Table 5.2 – Parameters used to model 996-AL5 conductor 996-AL5 (REDWOOD) [65]

	Number of strands	Diameter of a strand [mm]	Conductivity [S/m]	Relative magnetic permeability	Total diameter [mm]	Total area [mm²]
Al5 (aluminium alloy)	61	4.56	$3.2 \cdot 10^7$	1	41	996.2

In Table 5.1 and Table 5.2 can be seen a summary of the conductor properties used in modelling (ρ and μ are resistivity and relative magnetic permeability, respectively).

5.3.3. Setting up the geometry of the model

The chosen ACSR conductor is 528-Al1/69-ST1A (its old code was MOOSE). It has 54 aluminium strands and 7 steel strands (Table 5.1). The diameter of the aluminium and steel wires is the same and its value is 3.53 mm. The diameter of the core is 10.6 mm and of the conductor is 31.8 mm. The total area of the conductor is 597 mm^2 of which 528.7 mm^2 is the area of its aluminium part and 68.5 mm^2 of its steel part. The geometry of the model of this conductor is shown in Figure 5.3.2.

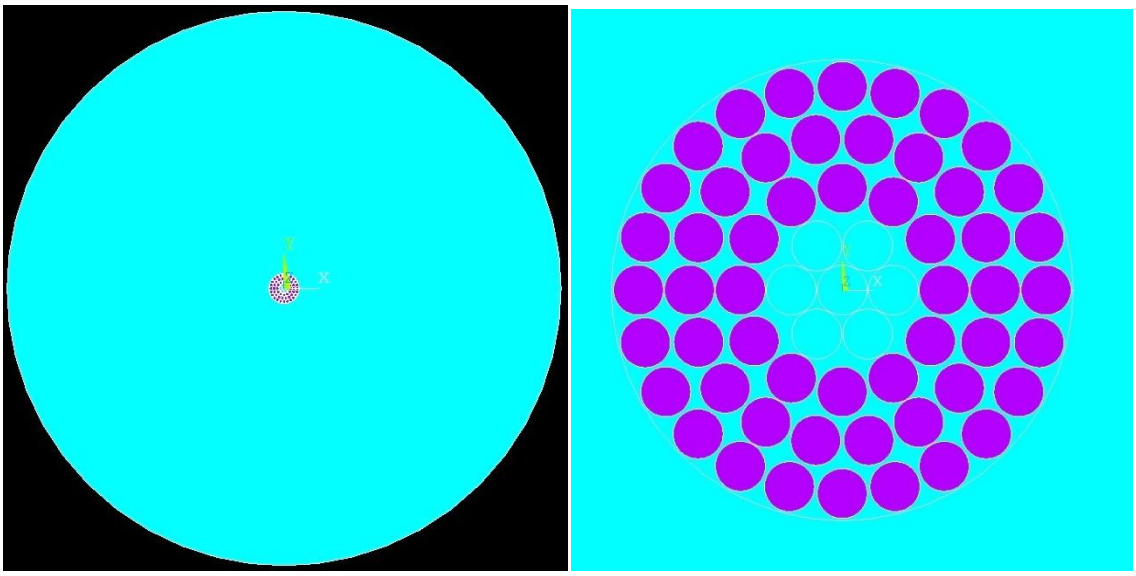

a) *b)*

Figure 5.3.2 – a) geometry of the whole model; b) geometry of the ACSR conductor 528-Al1/69-ST1A

Figure 5.3.2 a) shows the geometry of the whole model, whereas the geometry of the conductor consisting of the aluminium and steel strands can be seen in Figure 5.3.2 b). Although there are few exceptions, almost always the reinforcing part of the conductor is placed in its centre (in this example, steel strands are placed in the centre of the ACSR conductor, surrounded by aluminium strands). The program developed during this research assumes that the reinforcing part of the conductor is always in the middle. If that is not the case, a few changes would need to be done to the code.

The size of the „air circle“ (air surrounding the conductor) affects both, the accuracy of the obtained solution and the computational time to solve the problem. The border of the air circle should be far enough from the conductor because zero boundary conditions are enforced on its exterior. On the other hand, too big a circle and too many elements can significantly increase computational time.

The radius of the air circle in this model is 30 cm which is more than needed for the expected sizes of overhead conductors and values of electrical currents which are going to be modelled. However, as this size of air circle did not significantly increase computational time, and at the same time, it added the flexibility of testing higher currents than would normally be expected (and thus higher values of the magnetic field), it was reasonable not to decrease it. Another important advantage of such air circle size is the possibility to place an MSM element at further distances from the conductor. It should also be mentioned that although the strands inside the real conductor are touching other strands, in this model is introduced a very small distance between them of $7 \cdot 10^{-5}$ m to overcome the problem experienced in ANSYS APDL when two or more curves touch each other at a single point. As this distance is several orders of magnitude smaller than the dimensions of the strands inside the conductor and the conductor itself, this will have a negligible influence on the obtained results.

Another example of the conductor which is going to be shown here is, as mentioned earlier, AAAC conductor 996-AL5 (its old code was REDWOOD). It has 61 strands made of aluminium alloy AL5 Table 5.2. The diameter of each wire is 4.56 mm and the diameter of the conductor is 41 mm. The total area of the conductor is 996.2 mm^2. The geometry of the model of this conductor is shown in Figure 5.3.3. All procedures and reasonings that were mentioned for the modelled ACSR conductor before, apply to this model too.

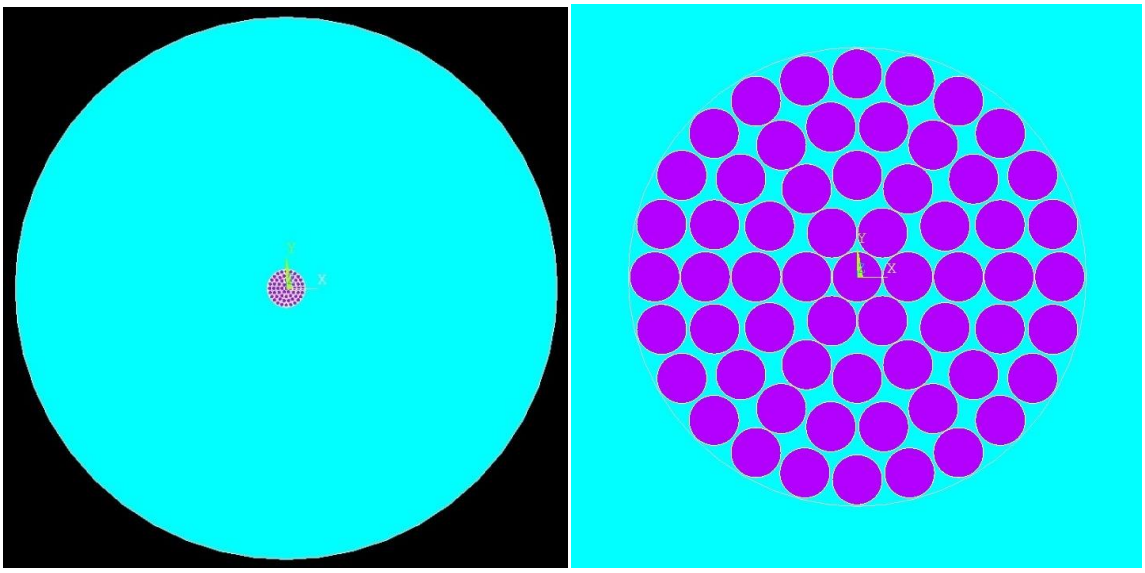

a) b)

Figure 5.3.3 – a) geometry of the whole model; b) geometry of the AAAC conductor 996-AL5

5.3.4. Finite element method model of the conductor

The next step which needs to be done in ANSYS APDL is to make a mesh. The mesh of the whole ACSR conductor is shown in Figure 5.3.4 (all aluminium and steel strands, the air between them and the air around the conductor) whereas the mesh of just one strand of this conductor (the middle one) can be seen in Figure 5.3.5. The mesh was obtained automatically by ANSYS APDL using its Mesh Tool. A level of mesh fineness was set to 1 (the highest level), and additional refinement was done after that. The elements that belong to the area around the conductor are refined at level 2 (the coarsest level of refinement is level 1) and the elements inside the conductor at level 3. There was no need for additional or better refinements of the model elements as a higher level of refinement did not give significantly better results (the maximum value of magnetix flux density in the model remained the same for the first five significant digits even when number of elements was increased) and the time of processing would unnecessarily be increased. The same procedure and the same reasoning were done for the model of the AAAC conductor.

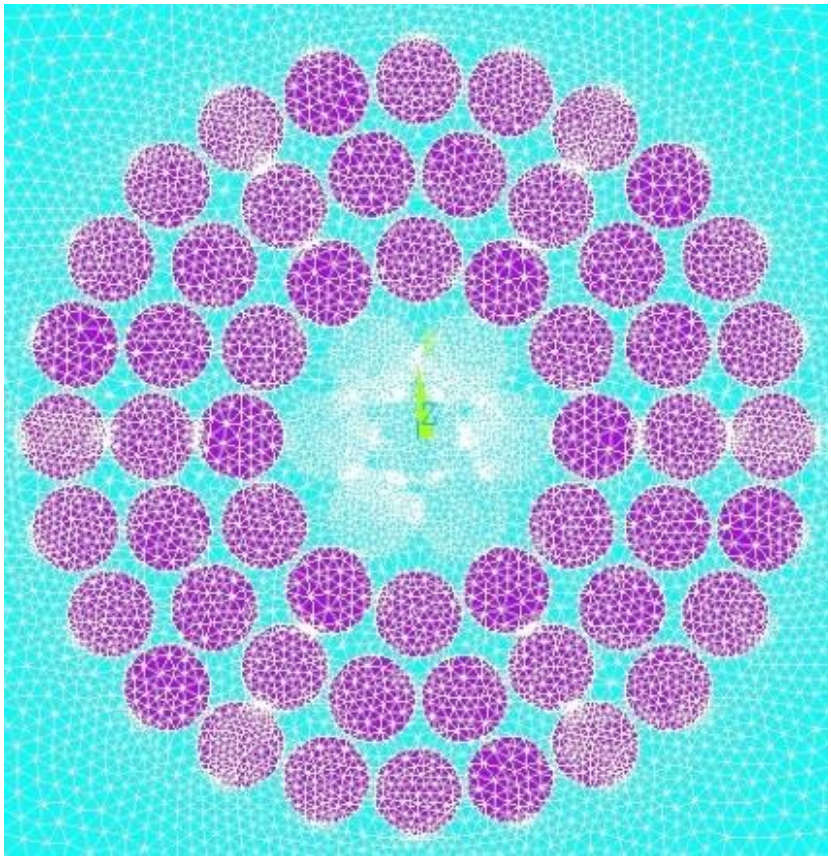

Figure 5.3.4 – Mesh of the ACSR conductor 528-Al1/69-ST1A

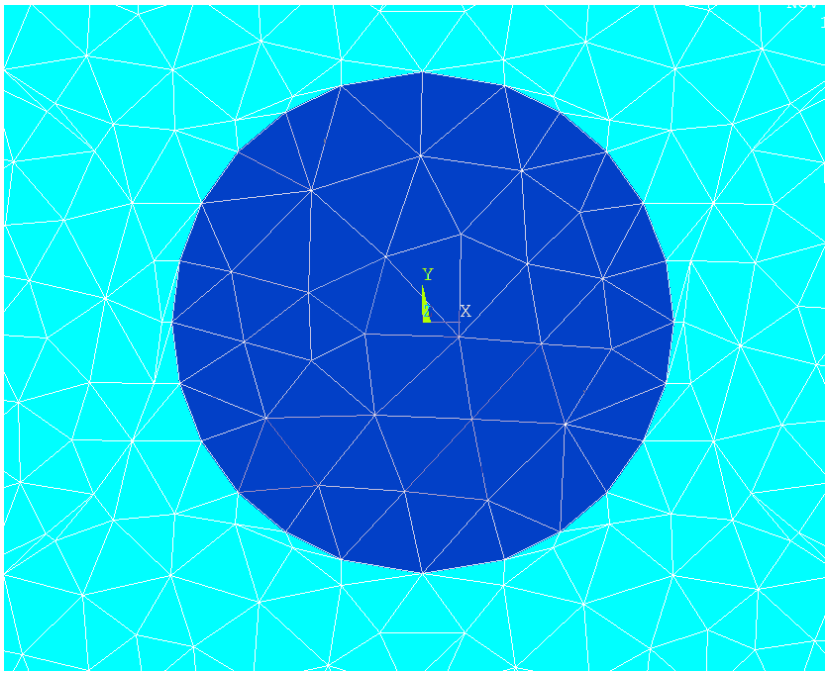

Figure 5.3.5 – Mesh of one strand of the ACSR conductor 528-Al1/69-ST1A

Element Plane53 has been used for modelling. It is an eight nodes element which is based on the magnetic vector potential formulation and has a nonlinear magnetic capability for modelling B-H curves. A non-linear time-harmonic analysis has been performed as it can predict quantities such as the time-averaged torque and power losses with good accuracy, and yet at much reduced computational cost compared to a transient time-stepping procedure.

When a non-harmonic analysis is done in ANSYS, the program replaces the DC B-H curve which was entered for the material in question with a fictitious or effective B-H curve based on an energy equivalence method. By using the effective B-H curve, a nonlinear transient problem can be effectively reduced to a nonlinear time-harmonic one. In this case, all field quantities are sinusoidal at a given frequency (similar to the linear harmonic analysis), but a nonlinear solution is computed.

The basic principle of the present nonlinear time-harmonic analysis is briefly explained next. First of all, the actual nonlinear ferromagnetic material is represented by another fictitious material based on energy equivalence. This amounts to replacing the DC B-H curve with a fictitious or effective B-H curve based on the following equation for the time period cycle [97]:

$$\frac{1}{2}\int_0^{B_{eff}} H_m dB_{eff} = \frac{4}{T}\int_0^{\frac{T}{4}} \left(\int_0^{B} H_m sin(\omega t)\, dB\right) dt \tag{5.16}$$

where is:

H_m - peak value of magnetic field

B - magnetic flux density

B_{eff} - effective magnetic flux density

T - time period

ω - angular velocity

t - time

Numerical benchmarks show that the approximation is of satisfactory engineering accuracy. [95]

It should be noted that Dirichlet boundary conditions were assigned to the exterior boundaries of the model. The load of the model is electrical AC where the value and frequency are defined by the user and need to be input at the start of the program.

5.3.5. Results and discussions on the model of the conductor

It is interesting to analyse the current distribution within the two conductors and the magnetic field around them. If these were solid conductors of the same effective cross-section area and if the current of amplitude 500A was uniformly distributed, the amplitude of current density would be:

$$J_{ACSR} = \frac{I}{A_{ACSRAl}} = \frac{500A}{528.7mm^2} = 9.46 \cdot 10^5 \frac{A}{m^2} \quad (5.17)$$

$$J_{AAAC} = \frac{I}{A_{AAAC}} = \frac{500A}{996.2mm^2} = 5.02 \cdot 10^5 \frac{A}{m^2} \quad (5.18)$$

where A_{ACSRAl} and A_{AAAC} are the areas of aluminium part of conductors 528-Al1/69-ST1A and 996-AL5, respectively. It should be mentioned that the effective areas of the strand conductors are smaller than of the solid conductors of the same diameter because of inevitable spaces between the strands filled with air.

However, the current will not be uniformly distributed as both, the proximity effect and skin effect (which is always present for any conductor loaded with AC) can be expected. Both these effects increase with the increase of frequency and increase of the cross-sectional area of the conductor. These effects are more prominent for solid conductors than for stranded ones.

Furthermore, the equation (5.7) will not provide accurate results for calculating skin depth in this case for two reasons. Skin depth depends on the conductivity of the conductor (it is larger for the conductors with lower conductivity). The stranded conductors will have lower conductivity than the solid conductors of the same size and the same material because of inevitable air gaps between the strands. This means that skin depth will be bigger for the stranded conductors.

Besides having the stranded conductors and not the solid ones, the other reason why the equation (5.7) will not provide accurate results is that the radius of both, individual strands and the whole conductors, is not much larger than the skin depth of the conductors (even if the conductors are observed as solid ones). Skin depth for these two conductors if we observe them as solid aluminium conductors with the same radius would be:

$$\delta_{ACSR} = \frac{1}{\sqrt{\pi f \mu \sigma}} = \frac{1}{\sqrt{\pi \cdot 50 \cdot 4\pi \cdot 10^{-7} \cdot 3.54 \cdot 10^{7}}} = 11.96\ mm \quad (5.19)$$

$$\delta_{AAAC} = \frac{1}{\sqrt{\pi f \mu \sigma}} = \frac{1}{\sqrt{\pi \cdot 50 \cdot 4\pi \cdot 10^{-7} \cdot 3.2 \cdot 10^{7}}} = 12.58\ mm \quad (5.20)$$

The radius of the ACSR conductor is 15.9 mm whereas the radius of the AAAC conductor is 20.5 mm which is the same order of magnitude as the values calculated in (5.19) and (5.20).

The current distribution inside the observed conductors is not possible to calculate analytically. The model that we have developed can provide more insight into it. Figure 5.3.6 and Figure 5.3.7 show the distribution of current density amplitude for the ACSR and the AAAC conductors respectively when the amplitude of the applied load is 500 A, 50 Hz.

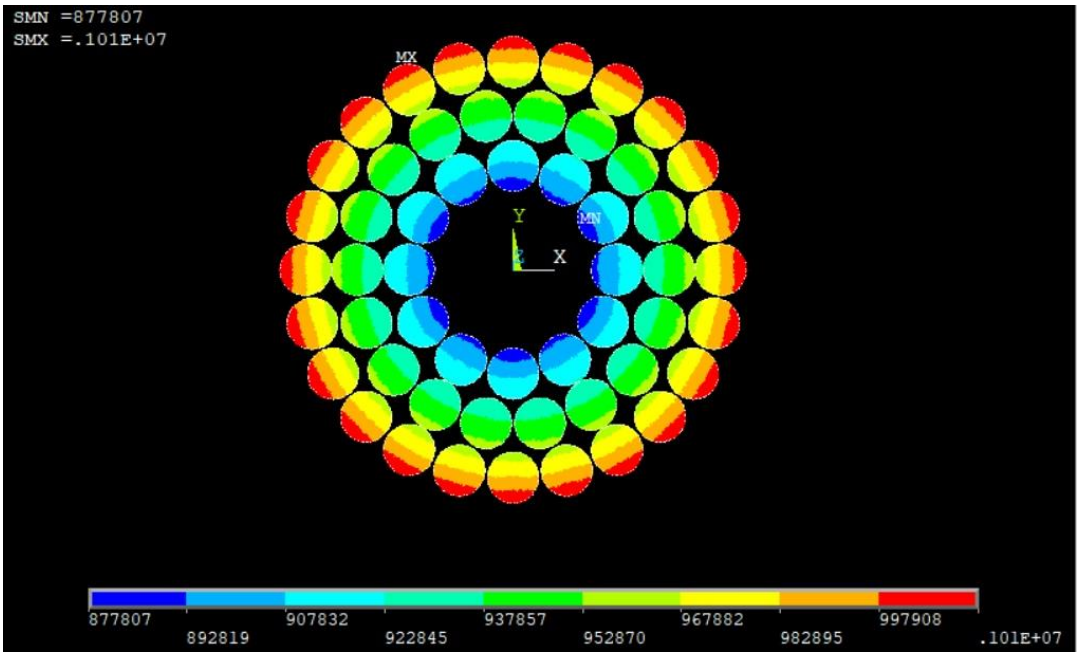

Figure 5.3.6 – Distribution of current density amplitude [A/m^2] inside ACSR 528-Al1/69-ST1A conductor when the amplitude of the applied load is 500 A, 50 Hz

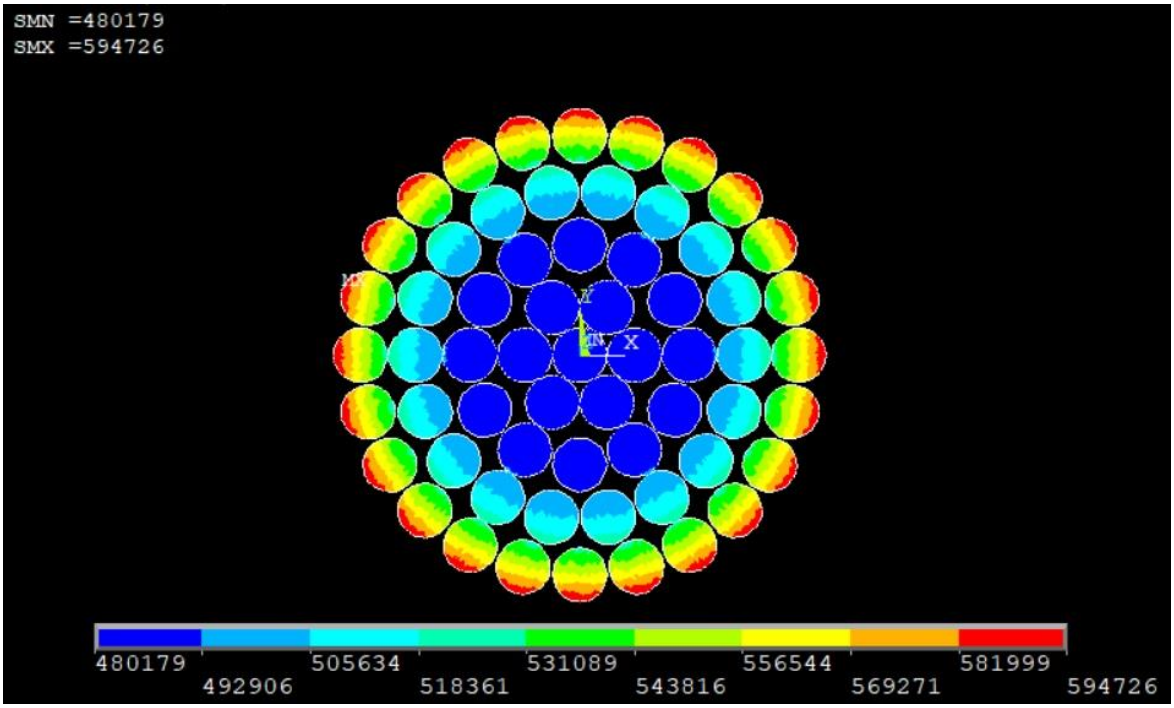

Figure 5.3.7 - Distribution of current density amplitude [A/m^2] inside AAAC 996-AL5 conductor when the amplitude of the applied load is 500 A, 50 Hz

The obtained results show that the current will be more concentrated near the conductors' surfaces similar to what it would have been for the solid conductors. In Figure 5.3.6 it can be seen that the current density amplitude changes in the range $8.78 \cdot 10^5 - 10.1 \cdot 10^5 Am^{-2}$ from the bottom part of the first layer of aluminium strands to the surface of the ACSR conductor. If it was uniformly distributed, its amplitude would have been $9.46 \cdot 10^5\ Am^{-2}$ (equation 5.17). Our results show that in the case of the AAAC conductor, the current density amplitude changes in the range $4.8 \cdot 10^5 - 5.95 \cdot 10^5\ Am^{-2}$ from the centre of the conductor to its surface. If it was uniformly distributed, its value would have been $5.02 \cdot 10^5\ Am^{-2}$ (equation 5.18).

It can be concluded from these results that although the current will be larger near the surface for both conductors (in a similar way as it would be the case for solid conductors), the skin and proximity effect are not very strong for none of these conductors at the frequency of 50 Hz as the significant current will flow through their whole cross-section. In the following models and analysis, more attention will be given to the ACSR conductor.

Another important thing that can be observed from the developed model is the distribution of the magnetic field around the conductor. Figure 5.3.8 shows the distribution of magnetic flux density around the ACSR conductor (the beginning of X-axes is at the conductor's surface) when the amplitude of the applied load is 500 A, 50Hz.

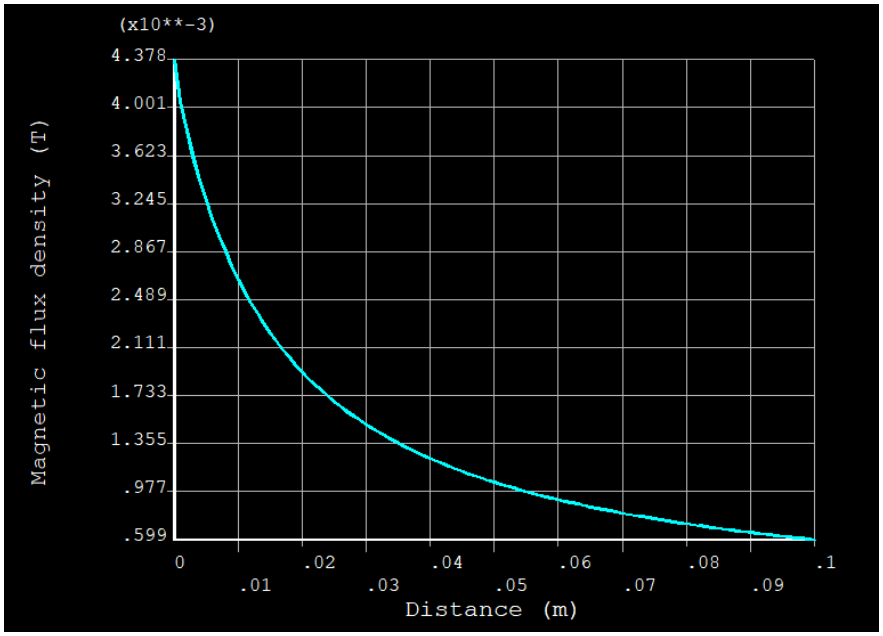

Figure 5.3.8 – Variation of magnetic flux density with distance from the surface of the ACSR 528-Al1/69-ST1A conductor (amplitude current 500 A, 50 Hz)

It will be interesting to compare this result to the results when an MSM material is placed near the conductor which will be discussed in Chapter 5.4.

5.3.6. 'Validation' of the developed model of the conductor

To check the developed model and the results obtained, we have compared it with the results published in another research [98-99] where the authors were investigating the effects of skin effect on current density distribution in solid conductors. In that research, two conductors with the same characteristics but different dimensions were analysed and the distribution of current density inside the conductors is provided (Figure 5.3.9 and Figure 5.3.10).

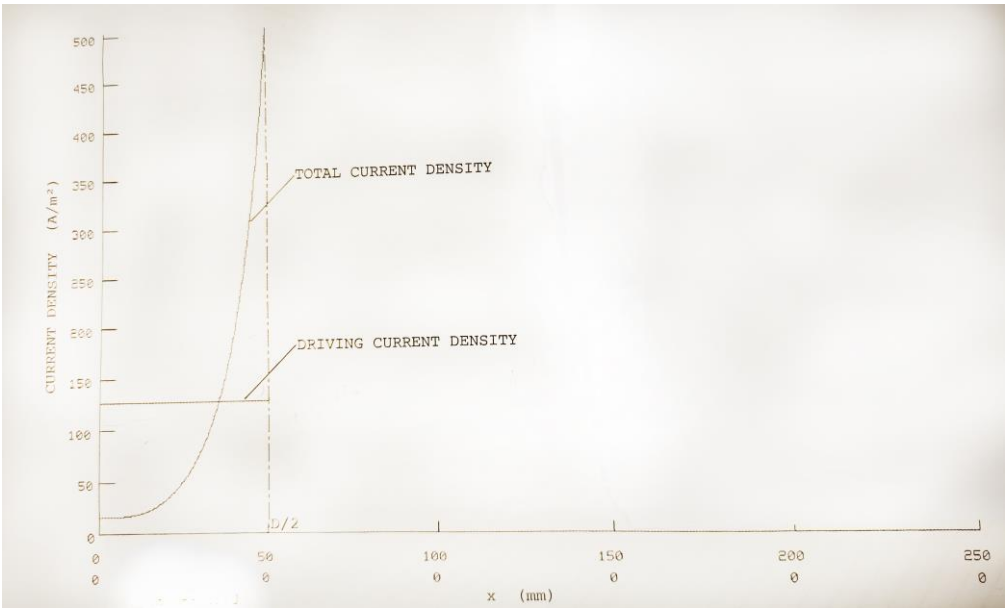

Figure 5.3.9 – Variation of current density through the solid conductor (d = 100 mm) with distance from its centre obtained in another research [98-99] – I = 1 A, 50 Hz

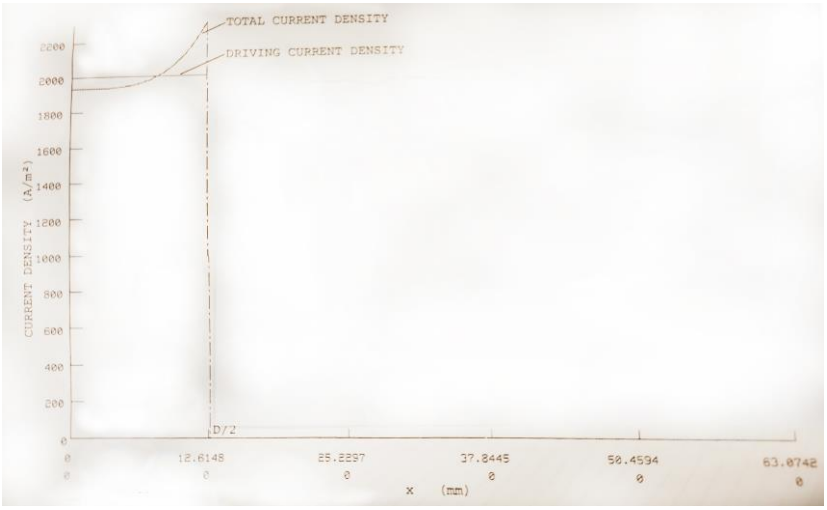

Figure 5.3.10 – Variation of current density through the solid conductor (d = 25.23 mm) with distance from its centre obtained in another research [98-99] – I = 1 A, 50 Hz

As mentioned earlier, the code we have developed can be used to analyse various types of conductors. Following the same procedure and having the same approach as in the previously described model, we have developed the same conductors as in [98-99]. They are

solid conductors of which one has a diameter of d = 100 mm and another d = 25.23 mm. Their resistivity is $\rho = 1.7241 \cdot 10^{-8}$ Ωm. The applied load was AC of I = 1 A, f = 50 Hz. The geometry of the whole model of the larger conductor is shown in Figure 5.3.11.

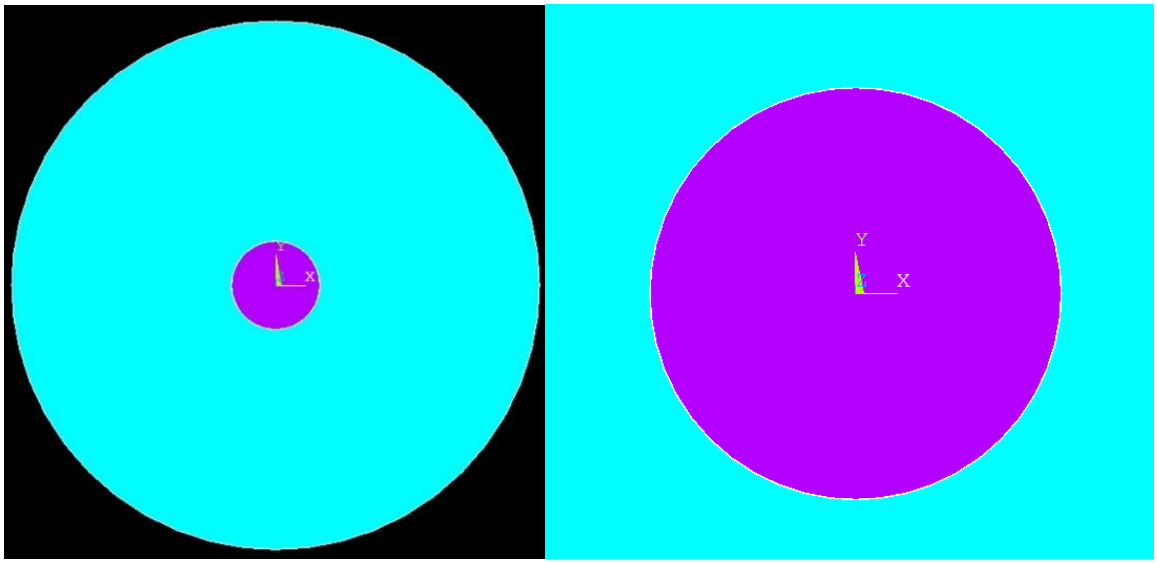

Figure 5.3.11 – a) Geometry of the whole model of the solid conductor in [98-99] (d = 100 mm); b) Geometry of the solid conductor

Skin depth in this case is:

$$\delta = \frac{1}{\sqrt{\pi f \mu \sigma}} = \sqrt{\frac{\rho}{\pi f \mu}} = 9.35 \text{ mm} \tag{5.21}$$

The results that we have obtained using our model for current density distribution inside those two conductors can be seen in Figure 5.3.12 and Figure 5.3.13.

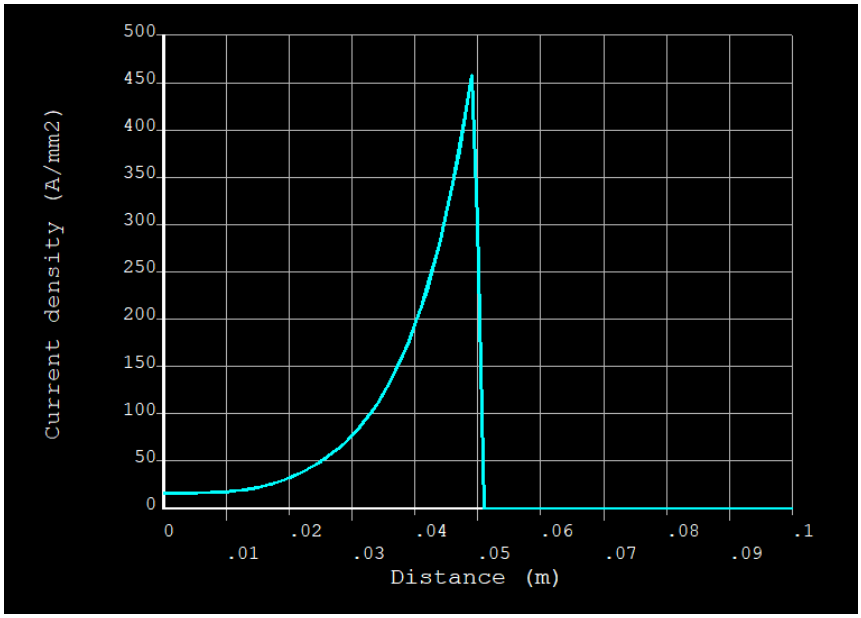

Figure 5.3.12 – Variation of current density through the solid conductor (d = 100 mm) as in [98-99] with distance from its centre – I = 1 A, 50 Hz

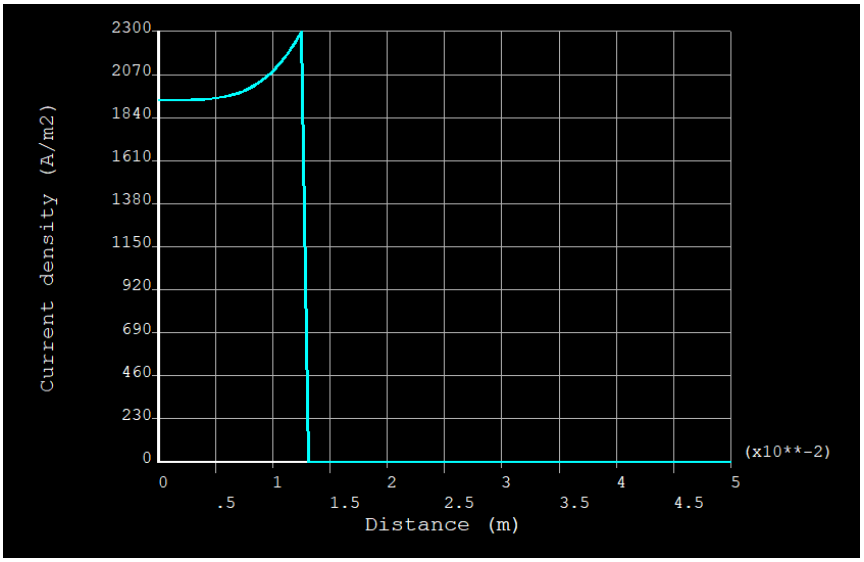

Figure 5.3.13 – Variation of current density through the solid conductor (d = 25.23 mm) as in [98-99] with distance from its centre – I = 1 A, 50 Hz

When comparing the graphs obtained from our model with those obtained in the aforementioned research, a strong correspondence is evident (see Table 5.3 and Table 5.4). We have compared the current density values at various characteristic points for each conductor. Although the data was obtained from the graphs, which introduces some errors, it is notable that the maximum difference between the results for the conductor with a diameter of d = 100 mm was slightly above 5%, while the conductor with a diameter of d = 25.23 mm exhibited a difference of less than 1% across all observed points.

Table 5.3 – Comparison of data obtained using our model with data from another research (d = 100 mm, I = 1 A, 50 Hz)

Distance from the centre of conductor [mm]	Current density - another research [A/m²]	Current density – our model [A/m²]	Difference [%]
0	16.75	16.05	4.18
10	18.34	18.97	-3.44
25.2	51.04	51.07	-0.06
35.7	126.79	129.86	-2.42
44.1	289.47	283.79	1.96
50	482.46	458.15	5.04

Table 5.4 – Comparison of data obtained using our model with data from another research (d = 25.23 mm, I = 1 A, 50 Hz)

Distance from the centre of conductor [mm]	Current density - another research [A/m²]	Current density – our model [A/m²]	Difference [%]
0	1944.61	1933.56	0.57
3.8	1951.91	1933.56	0.94
5.4	1959.20	1949.15	0.51
7.9	2013.93	1999.83	0.70
10.6	2152.57	2140.17	0.58
12.6	2320.40	2300.00	0.88

Besides validating the results obtained by our model, these results also show the validity of the taken approach and methodology in developing our model.

5.4. Modelling of non-conventional instrument transformer

5.4.1. Model of MSM near conductors

When a magnetic material such as MSM is placed near the conductor, it influences magnetic field distribution. To analyse this and the possibility of triggering MSM material, what is especially important for this research, a non-elongated MSM element has been placed near the surface of the conductor (at a distance of 1 mm from its surface).

This model has been developed in the same way as the previously described model of conductors, just an additional MSM element has been added next to ACSR conductor 528-Al1/69-ST1A (Figure 5.4.1).

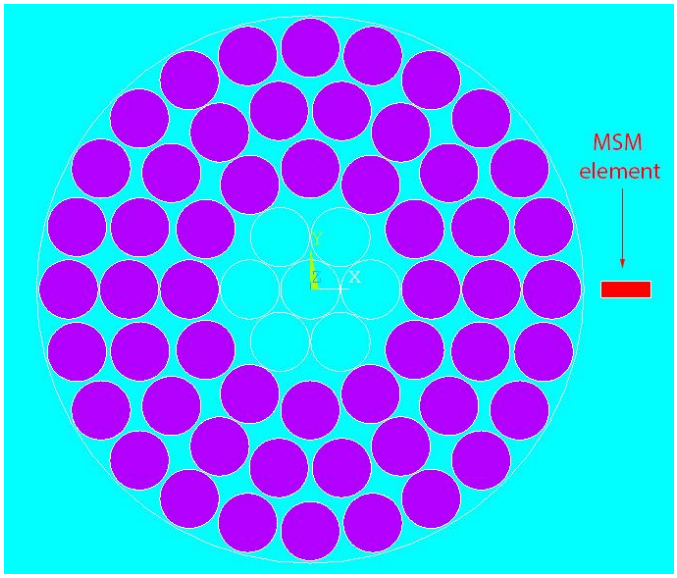

Figure 5.4.1 – Geometry of the model of ACSR conductor 528-Al1/69-ST1A when an MSM element is added at the distance of 1 mm from its surface

The relative magnetic permeability of the MSM element, in this case, is $\mu_r = 2$ because it is assumed that the MSM element is still not triggered and thus still not elongated. The amplitude current is 1000 A.

The distribution of magnetic flux density is going to be different now with the MSM element around (in comparison to Figure 5.3.8) and that can be seen in Figure 5.4.2 and Figure 5.4.3.

It should be noted as well that in this case amplitude of current was 1000 A whereas in the previous cases it had different values.

Figure 5.4.2 shows the distribution of the magnetic field from the surface of the conductor to the distance of 100 mm (including the field inside the MSM element as well), whereas Figure 5.4.3 is focused more on the field around the MSM element as it shows the field from the surface of the conductor to the distance of 10 mm from it.

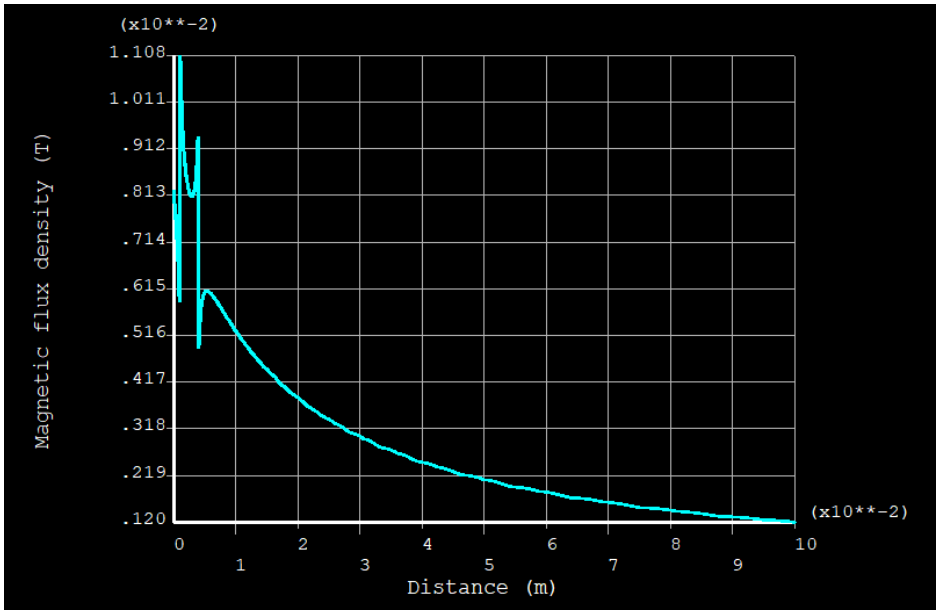

Figure 5.4.2 – Variation of magnetic flux density with distance from the surface of the conductor when an MSM element is placed at the distance of 1 mm from its surface (amplitude current 1000 A, 50 Hz)

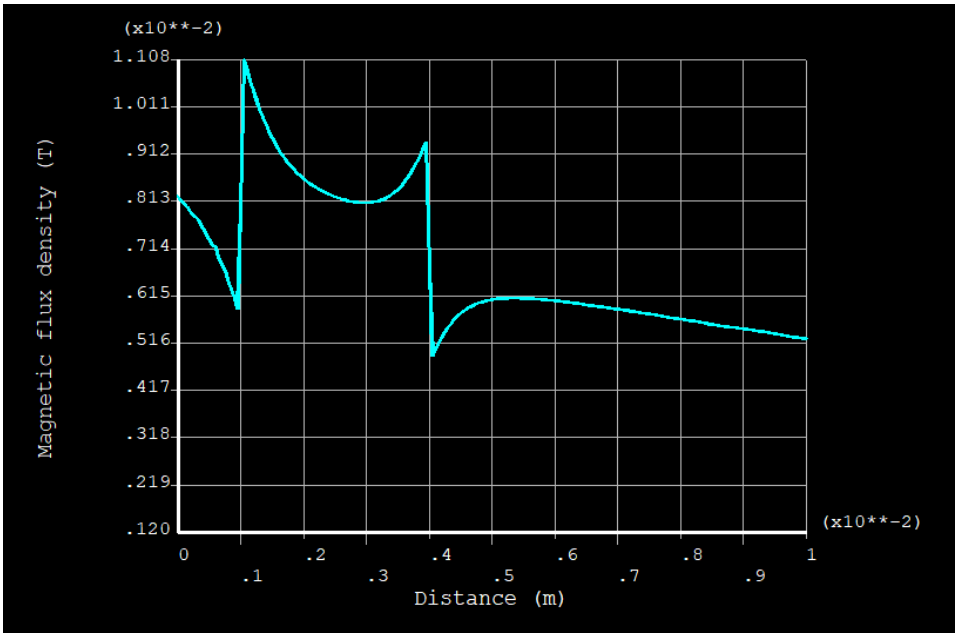

Figure 5.4.3 – Magnetic flux density inside the MSM element and around the conductor measured from its surface when an MSM element is placed at the distance of 1 mm from its surface (amplitude current 1000 A, 50 Hz)

From both graphs, it can be seen that the maximum value of *B* is 10.86 mT. That value of magnetic flux density is not enough to trigger an MSM element, thus the MSM element will not be triggered even if it is placed as close to the conductor as 1 mm, which has been done in this example. This was the case although the current amplitude was 1000 A, which is more than what normally would be expected in the normal working regime.

These results have shown that the MSM element is not sensitive enough to be used by itself for the measurement of AC in high voltage overhead transmission lines in the normal working regime.

That problem can be overcome by adding a magnetic circuit to NCIT's design in a way that it concentrates, as much as possible, the magnetic field around the current-carrying conductor and direct it towards the MSM element. Designing a magnetic concentrator raised several questions such as what should be the shape and size of it, which material should be used for its construction, and what should be the size of the air gap between the magnetic concentrator and MSM element.

5.4.2. Consideration of geometric parameters for NCIT design

Three different designs have been proposed and compared: rectangular, rectangular magnetic circuit with rounded corners and circular (Figure 5.4.4, Figure 5.4.5 and Figure 5.4.6).

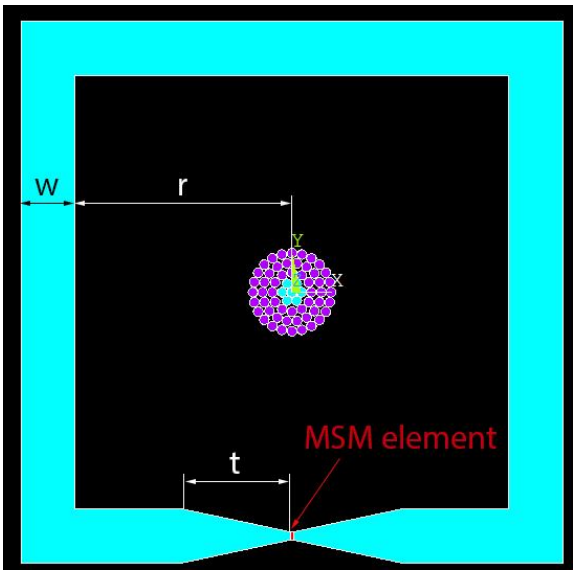

Figure 5.4.4 – 2D finite element model of the rectangular design of the magnetic circuit of the proposed NCIT around a 528-Al1/69-ST1A conductor (shown in the centre)

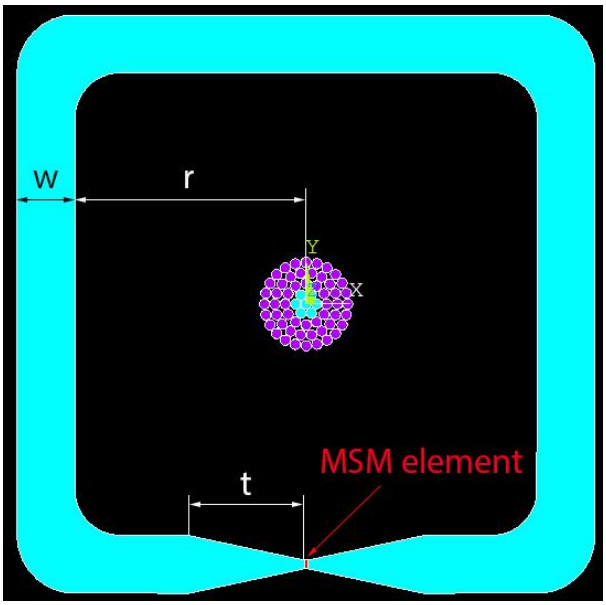

Figure 5.4.5 – 2D finite element model of the rectangular design with rounded corners of the magnetic circuit of the proposed NCIT around a 528-Al1/69-ST1A conductor (shown in the centre)

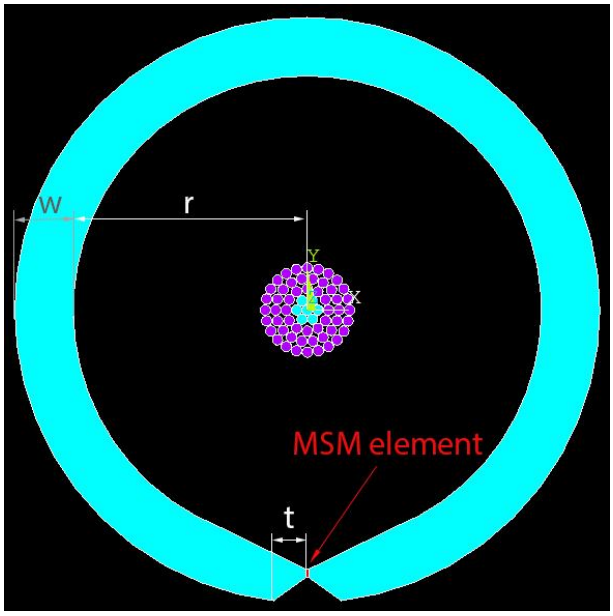

Figure 5.4.6 – 2D finite element model of the circular design of the magnetic circuit of the proposed NCIT around a 528-Al1/69-ST1A conductor (shown in the centre)

The poles in each of the designs were tapered in order to focus the field towards the MSM element which is placed between them. We have used rectangular geometry of the MSM element that can be readily obtained and is suitable for the proposed NCIT (length × width × thickness, 10 mm × 3 mm × 1 mm). As the MSM element and the airgap are of particular interest, they are shown enlarged in Figure 5.4.7 and Figure 5.4.8. This part of the magnetic circuit is very similar in all three designs so, here, only one of them will be shown. Figure 5.4.7 shows this part of the circuit without the MSM element whereas Figure 5.4.8 shows the same part with the MSM element.

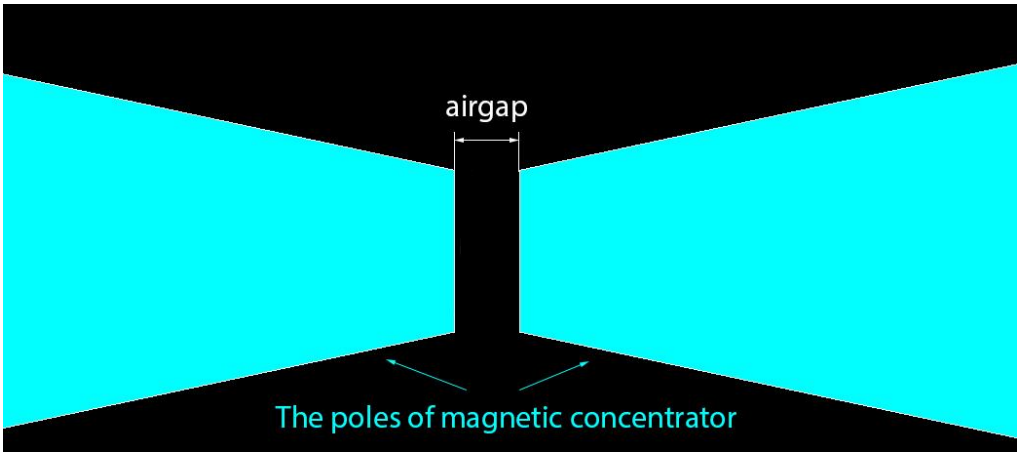

Figure 5.4.7 - The poles of the magnetic circuit and the airgap between them

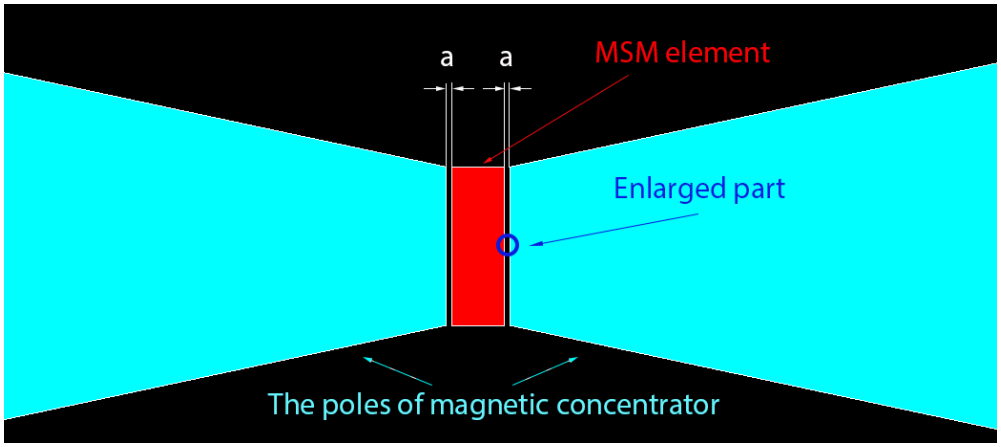

Figure 5.4.8 – The MSM element fitted between the poles of the magnetic circuit with the airgap 'a' on both sides of it

Furthermore, the meshes of the airgaps for all three proposed designs are shown in Figure 5.4.9, Figure 5.4.10 and Figure 5.4.11. It should be noted that this part of the model has very fine mesh so only a small, enlarged part of it is shown (as shown in Figure 5.4.8). Discussion about the mesh of the chosen design of the magnetic circuit will be continued later in the following subchapters.

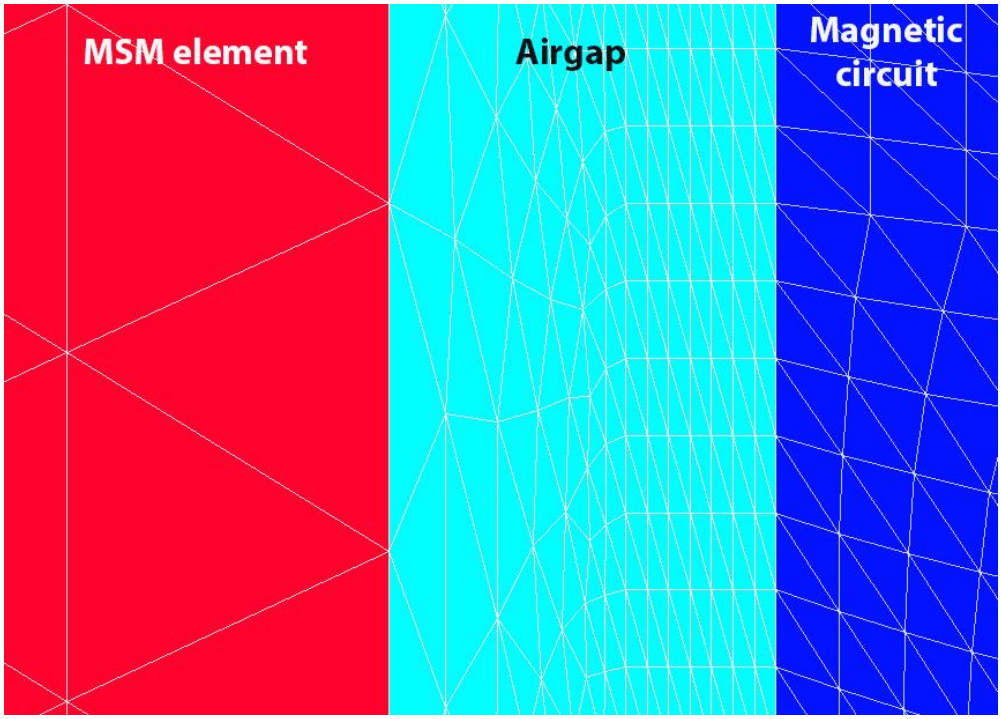

Figure 5.4.9 – Mesh of the airgap between the MSM element and the poles of the rectangular magnetic circuit

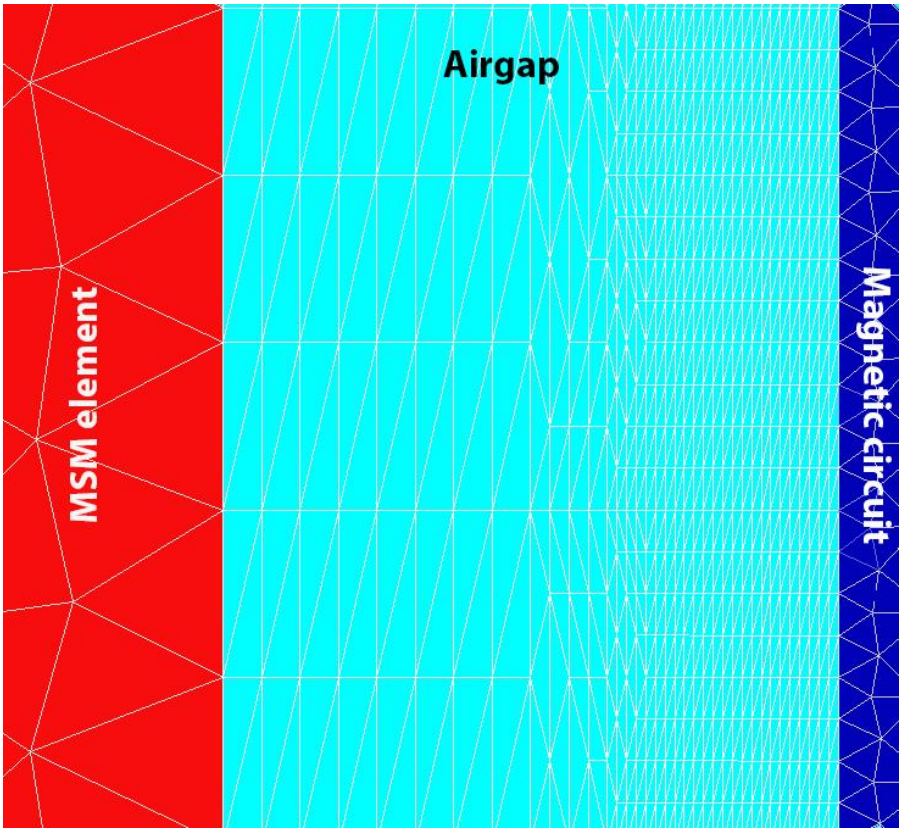

Figure 5.4.10 – Mesh of the airgap between the MSM element and the poles of the rectangular magnetic circuit with rounded corners

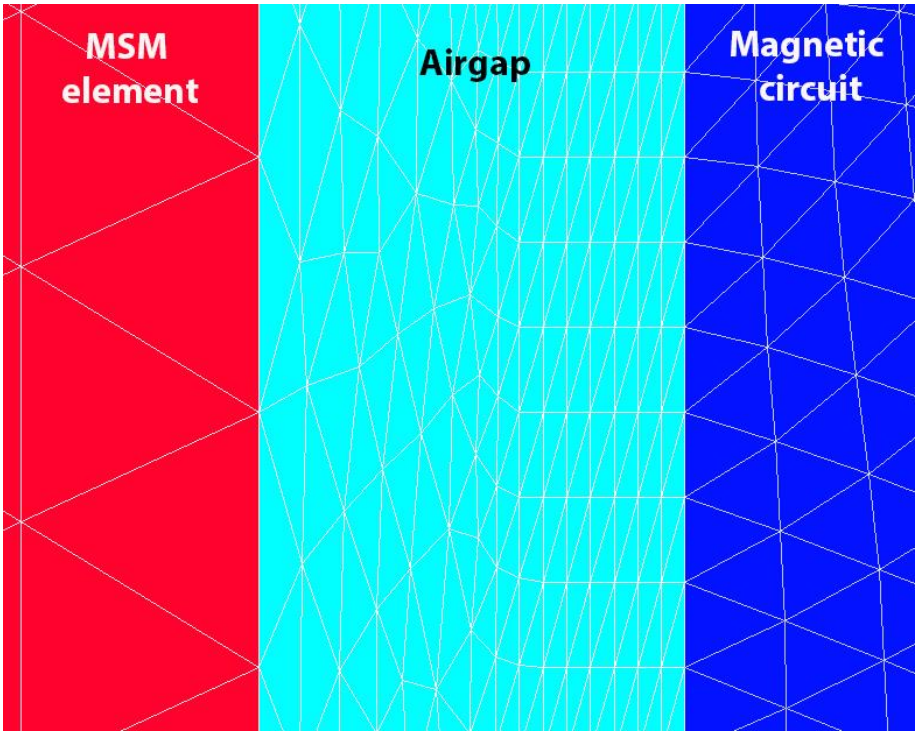

Figure 5.4.11 – Mesh of the airgap between the MSM element and the poles of the circular magnetic circuit

We have compared the sensitivity of all three NCIT designs for similar geometric parameters. The goal was to compare the variations of the magnetic field on the surface of the MSM element, $B_{surface}$ for the proposed designs. The obtained results are shown in Table 5.5. The position of the magnetic circuit relative to the conductor (distance between the centre of the conductor and the inner side of the magnetic circuit) is *r*, the magnetic circuit's width is *w* and the distance from the airgap to the point where the poles start to taper is *t* (Figure 5.4.4, Figure 5.4.5 and Figure 5.4.6). Simulations have been done for AC of the frequency 50 Hz and amplitude 400 A. The material used for the magnetic circuit is Hiperco 50. $B_{surface}$ [%] shows the change of the magnetic field density on the surface of the MSM element in comparison to the circular design.

Table 5.5 – Magnetic flux density on the surface of the MSM element for three different magnetic circuit designs of NCIT (I = 400 A, f = 50 Hz).

Shape of magnetic circuit	*w* [mm]	*t* [mm]	*r* [mm]	$B_{surface}$ [T]	$B_{surface}$ [%]
Circular	20	40	80	0.119	
Rectangular	20	40	80	0.112	-5.95
Rectangular with rounded corners	20	40	80	0.115	-3.36

The value of magnetic flux density slightly varies along the MSM element, especially at its edges which is something that can be expected. In Table 5.5, its average value is taken into account, which will also be the case in further discussions and observations.

The comparison of magnetic flux densities along the side of the MSM element for all three designs is presented in Figure 5.4.12

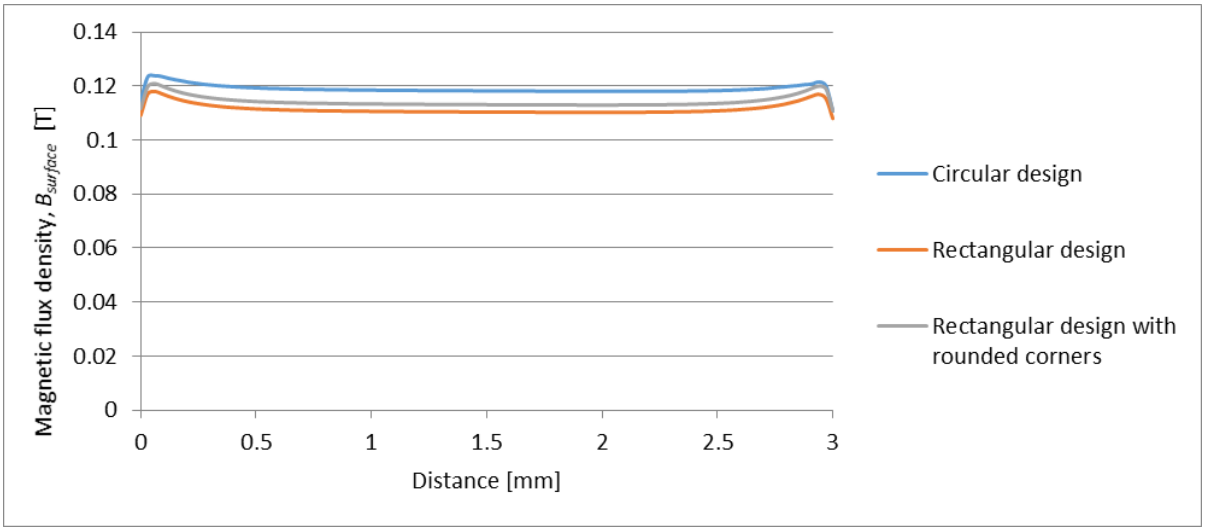

Figure 5.4.12 - Magnetic flux density in the airgap along the side of the MSM element for three designs: circular (top curve), rectangular with rounded corners (middle curve), and rectangular (bottom curve). (I_{amp} = 400 A, r = 80 mm, w = 20mm, t = 40 mm)

It can be seen from Table 5.5 and Figure 5.4.12 that the sensitivity of all three considered designs was very similar. $B_{surface}$ for both the rectangular designs are comparable to that of the circular design. As expected, the rounding of the corners has improved the sensitivity of the NCIT. The circular magnetic circuit shows slightly higher sensitivity than the rectangular ones and the rectangular magnetic circuit with rounded corners was slightly more sensitive than the rectangular circuit without rounded corners. The results show that any of the three proposed designs can be used. However, due to practical reasons in handling and mounting the magnetic circuit around the conductor, the preferred design would be the rectangular one with rounded corners. The following analyses apply to this design.

In this part where the magnetic flux densities in the airgaps of the three designs were discussed, it is suitable to show the distribution of magnet flux lines through the MSM element and the airgap between the poles of the magnetic circuit as well. Figure 5.4.13 shows these lines for the rectangular circuit with rounded corners, but they look very similar for the other two designs too.

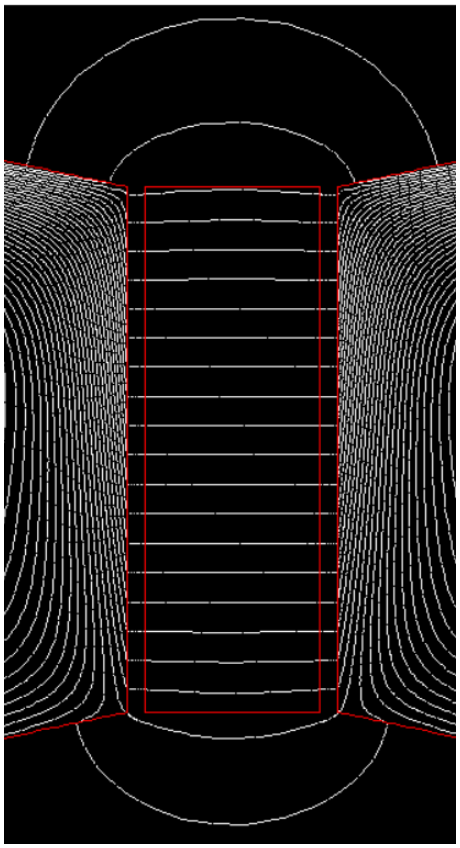

Figure 5.4.13 – Magnetic flux lines through the MSM element and the airgap between the poles of the magnetic circuit

Furthermore, it was interesting to do a comparison between the three designs when the MSM element was taken out from the airgap in order to get a better picture of how the presence of an MSM element in the airgap changes the magnetic field. The geometry of the circuits and the values of the current remained the same as in the previously discussed case when the MSM element was placed in the airgap. The comparison of magnetic flux densities in the airgap (at the same distance from the poles as in the previous case) for all three designs is presented in Figure 5.4.14.

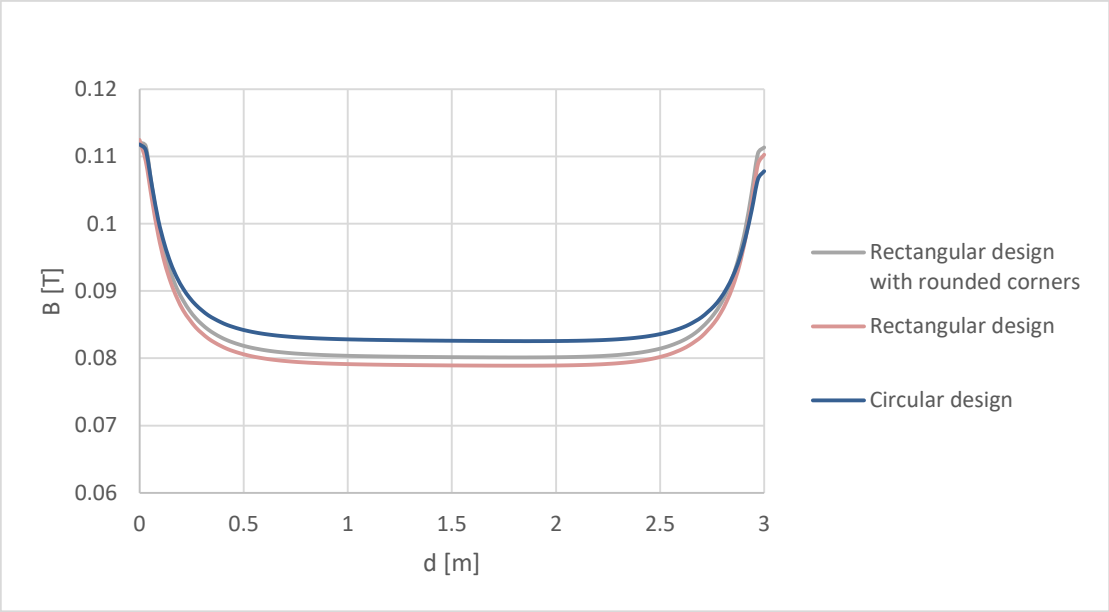

Figure 5.4.14 – Magnetic flux density in the airgap without the MSM element for three designs: circular (top curve), rectangular with rounded corners (middle curve) and rectangular (bottom curve). (I_{amp} = 400 A, r = 80 mm, w = 20mm, t = 40 mm)

If we compare Figure 5.4.12 and Figure 5.4.14, it can be seen that the values of magnetic flux density in the airgap are lower in the case when there is no MSM element which can be expected as the MSM element is a magnetic material. However, the relationship between the three designs has not changed – the circular design was the most sensitive one, followed by the rectangular design with rounded corners, and the rectangular design. The difference between their sensitivities once again was not very big. The maximum difference between magnetic flux densities of the circular design and the rectangular design with rounded corners was 2.95%, and it was 4.44% between the circular design and the rectangular design.

5.4.3. Choice of suitable materials for magnetic circuit

One of the questions that need to be considered is the choice of material for the magnetic circuit. Several aspects are needed to be taken into account, such as the value of saturation flux density, resistivity, skin depth, and availability of the bulk material. The higher resistivity means that the values of eddy currents induced in the concentrator will be smaller, but usually, the materials with high resistivity have a lower magnetic flux density saturation point.

We considered three materials that are commercially available, and that could be potentially interesting for this application: Hiperco 50, Radiometal 4550 and Armco. Furthermore, they have been found particularly suitable for actuator design in [76] and [100]. Hiperco 50 is an iron-cobalt-vanadium soft magnetic alloy whereas Radiometal 4550 is a 45% Nickel-Iron alloy. Armco is low-carbon steel with a purity that can be even over 99.85%. Hiperco 50 saturates at 2.33 T, Radiometal 4550 at 1.6 T and Armco at 2.15 T. Their BH curves can be seen in Appendix 4.

All three materials have high magnetic permeability, especially the first two. However, saturation flux density differs considerably among them. Their characteristics are shown in Table 5.6.

Table 5.6 – Characteristics of the materials considered for the magnetic circuit

Material	Resistivity [Ωm]	Relative magnetic permeability	Skin depth* [mm]	Saturation flux density [T]
Hiperco 50	$40.1 \cdot 10^{-8}$	1000 – 12000	1.42 – 0.41	2.33
Radiometal 4550	$4.5 \cdot 10^{-7}$	6000 – 40000	0.62 – 0.24	1.6
Armco	$9.9 \cdot 10^{-8}$	300 – 6000	1.29 – 0.29	2.15

*f=50Hz

It can be noticed that not a single, but a range of values is given for relative permeability μ_r as those values depend on the operating point of the BH curve. Consequently, as skin depth δ depends on magnetic permeability (equation 5.7), the range of its values is given as well. It can be concluded that the skin depth is very small for all the considered materials thus a laminated material should be used for the magnetic circuit.

We compared magnetic flux density in the air gap along the 3 mm side of the MSM element for the three magnetic materials when the current amplitude is 400 A and the geometry is the same (r = 80 mm, w = 20 mm, t = 60 mm, distance from the surface of the MSM element is 0.05 mm). Figure 5.4.15 shows the results obtained for the three different materials.

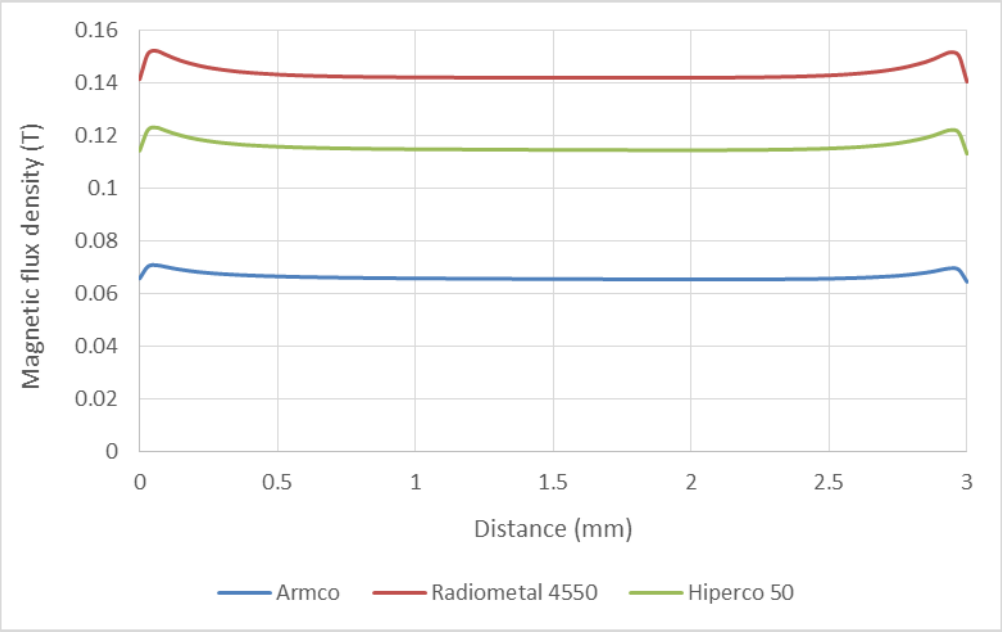

Figure 5.4.15 – Magnetic flux density in the airgap along the side of the MSM element for three materials: Radiometal 4550 (top curve), Hiperco 50, (middle curve), and Armco (bottom curve). (I_{amp} = 400 A, r = 80 mm, w = 20 mm, t = 60 mm)

The results show that Armco is considerably less sensitive in comparison to the other two materials. Although Radiometal 4550 is slightly more sensitive than Hiperco 50, it also saturates quicker than Hiperco 50 (Table 5.6). As their sensitivities are not very different, Hiperco 50 is the most suitable material for the proposed NCIT.

5.4.4. Optimisation of the magnetic circuit geometry

Besides the choice of magnetic materials, it is also very important to carefully consider the magnetic circuit geometry as it affects its saturation point, sensitivity to high temperatures from the current-carrying conductor and, finally, the triggering threshold of the MSM element. Whereas there is not much flexibility in the size of the MSM element, there are flexibilities in the design of the magnetic circuit, especially in terms of its geometry and distance from the conductor.

Many parameters need to be considered in order to optimise the magnetic circuit geometry for the application of NCIT for high voltage overhead transmission lines. These parameters include: the size of the airgap, *a* (the airgap between the MSM element and the poles), the

position of the magnetic circuit relative to the conductor (distance between the centre of the conductor and the inner side of the magnetic circuit, *r*), magnetic circuit's width, *w*, and the distance from the airgap to the point where the poles start to taper, *t* (Figure 5.4.5 and Figure 5.4.8). The comparisons presented in the following tables have been done for the rectangular Hiperco 50 magnetic circuit with rounded corners.

Firstly, we changed the size of the airgap while the other parameters were kept constant.

Table 5.7 shows the variation of magnetic field amplitude on the surface of the MSM element, $B_{surface}$, and the maximum value of the magnetic field inside the magnetic circuit, B_{max} in this case. $B_{surface}$ *[%]* and B_{max} in magnetic circuit [%] show a percentage change in comparison to the case when the airgap is the smallest (a = 0.1 mm). The current amplitude was 400 A and the frequency 50 Hz.

The results show that even a small increase in the airgap significantly decreases $B_{surface}$. To increase the sensitivity of NCIT, the airgap size needs to be as small as it is possible. The best choice for the airgap size was found to be 0.1 mm as any further decrease in the airgap is limited by technological factors.

Table 5.7 – Variation of magnetic flux density on the surface of the MSM element and in the magnetic circuit with the airgap (I = 400 A, f = 50 Hz)

w [mm]	*t* [mm]	*r* [mm]	Airgap [mm]	$B_{surface}$ [mT]	$B_{surface}$ [%]	B_{max} in mag. circuit [mT]	B_{max} in mag. circuit [%]
20	60	80	0.1	115.83	0	1086.68	0
20	60	80	0.2	100.23	-13.5	1048.47	-3.5
20	60	80	0.3	88.69	-23.4	1054.29	-3.0
20	60	80	0.5	72.51	-37.4	1013.01	-6.8
20	60	80	1	50.56	-56.4	983.34	-9.5

The overall diameter of the modelled conductor, 528-Al1/69-ST1A, is 31.8 mm. Therefore, the magnetic circuit around the conductor can be placed only in a way that r > 15.9 mm. On the one hand, the magnetic circuit should be placed as close as possible to the conductor

because flux density on the surface of the MSM element decreases significantly as it is placed away from the conductor. On the other hand, it is better to place it further away from the conductor as the MSM element then saturates at higher magnetic fields which increases the upper limit of the measured current range. Furthermore, it should be placed far enough so that the heat around the conductor does not affect the magnetic circuit, especially the temperature-sensitive MSM element. Table 5.8 shows the variation of magnetic flux densities $B_{surface}$ and B_{max}, with the position of the magnetic circuit relative to the conductor.

Table 5.8 – Variation of magnetic flux density on the surface of the MSM element and in the magnetic circuit with distance, r between the conductor and the magnetic circuit (I = 500 A, f = 50 Hz)

w [mm]	t [mm]	r [mm]	$B_{surface}$ [T]	$B_{surface}$ [%]	B_{max} in mag. circuit [T]	B_{max} in mag. circuit [%]
10	20	25	0.25	100.00	1.67	100.00
10	20	30	0.23	-6.8	1.57	-6.1
10	20	40	0.21	-17.2	1.48	-11.3
10	20	50	0.19	-25.4	1.41	-15.7
10	20	60	0.17	-31.9	1.31	-21.5

Table 5.8 presents quantitatively how B is decreasing as the magnetic circuit is moved further away from the conductor. As a referent point is taken a distance when the magnetic circuit is the closest to the conductor (r = 25 mm) and the decrease of B in percentage is shown in comparison to this point for all other designs.

Table 5.9 shows the range of currents that can be measured for various distances between the conductor and the magnetic circuit. The MSM element is triggered and begins to elongate when the current amplitude reaches a value, I_{trigg}, but it still does not follow current changes for this value. That happens for the values above I_{min}. It saturates and does not change its shape anymore for the currents above I_{max}.

Table 5.9 – Measurement range of the current amplitudes for different distances between the conductor and the magnetic circuit

w [mm]	*t [mm]*	*r [mm]*	I_{trigg} *[A]*	I_{min} *[A]*	I_{max} *[A]*
10	20	30	240	360	920
10	20	35	250	390	1000
10	20	40	270	420	1100
10	20	45	290	450	1185
10	20	50	300	460	1280
10	20	55	330	490	1370
10	20	60	335	530	1465
10	20	80	400	640	1830

In Table 5.7, the range of currents that can be measured once the MSM has been triggered for the distances from r = 30-80 mm is presented. This analysis provides a better insight into the required size of the magnetic concentrator depending on the range of currents that need to be measured.

Table 5.10 and Table 5.11 show the change of flux densities, $B_{surface}$ and B_{max}, when the parameters w and t have been changed, respectively. A narrow magnetic circuit is more sensitive but it saturates more easily. A wide magnetic circuit is not very practical either as it will increase both the size of the NCIT and its cost. Therefore, there needs to be a trade-off concerning the magnetic circuit width, w. We have found that a value, w = 20 mm is a reasonable size.

Table 5.10 – Variation of magnetic flux density on the surface of the MSM element and in the magnetic circuit with the magnetic circuit width, w (I_{amp} = 400 A, f = 50 Hz)

w [mm]	*t [mm]*	*r [mm]*	$B_{surface}$ *[mT]*	$B_{surface}$ *[%]*	B_{max} *in mag. circuit [mT]*	B_{max} *in mag. circuit [%]*
5	35	55	146.05	0	1328.91	0
10	35	55	144.84	-0.8	1314.12	-1.1
15	35	55	143.45	-1.8	1280.86	-2.3
20	35	55	141.90	-2.8	1290.81	-2.9
25	35	55	139.97	-4.2	1284.58	-3.3
30	35	55	137.96	-5.5	1271.47	-4.3

$B_{surface}$ *[%]* and B_{max} *in mag.[%]* show a percentage change in comparison to the case when the magnetic circuit is the narrowest (*w* = 5 mm).

Table 5.11 – Variation of magnetic flux density on the surface of the MSM element and in the magnetic circuit with the tapering distance (I_{amp} = 400 A, f = 50 Hz)

w [mm]	*t [mm]*	*r [mm]*	$B_{surface}$ *[mT]*	$B_{surface}$ *[%]*	B_{max} *in mag. circuit [mT]*	B_{max} *in mag. circuit [%]*
20	5	55	113.12	0	1307.64	0
20	10	55	127.56	12.8	1295.64	-0.9
20	15	55	133.87	18.3	1289.23	-1.4
20	20	55	137.22	21.3	1292.02	-1.2
20	25	55	139.44	23.3	1285.68	-1.7
20	30	55	140.87	24.5	1286.23	-1.6
20	35	55	141.90	25.4	1290.81	-1.3

Data presented in Table 5.11 show that tapering the poles of the magnetic circuit increases magnetic flux density on the MSM surface significantly (more than 20% in some cases) for the given geometry compared to the non-tapered circuit. However, the results also show that the level of tapering does not influence the sensitivity a lot as further tapering increase

sensitivity only for a few percents. Nevertheless, tapering is recommended as much as geometry allows it. For example, this value could be chosen around t = 35 mm for the given geometry.

5.5. Correlation between the strain of the MSM element and the conductor current

In the previous considerations, the focus was to increase the sensitivity of the proposed NCIT. The sensitivity of the MSM element was not very high at the low magnetic field, so it was necessary to add a magnetic circuit to increase the magnetic field through the MSM element to trigger its strain.

However, once the MSM element is triggered many other parameters need to be considered and analysed to obtain valid results.

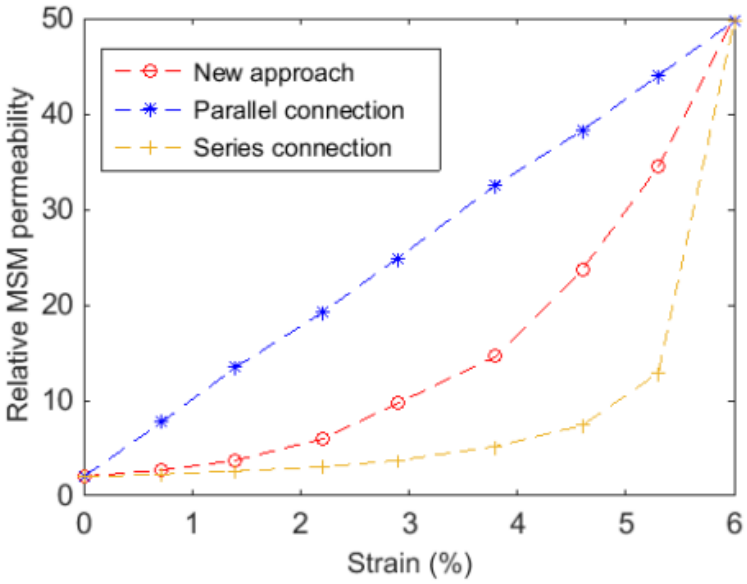

Figure 5.5.1 – Change in equivalent relative permeability of the MSM element [79]

The relative magnetic permeability of an MSM element is not constant. It changes from μ_r = 2, when it is fully contracted and consists only of hard variants, to μ_r = 50, when is fully

elongated and consists only of easy variants. During the elongation process, the MSM element consists of a variable number of hard and easy variants which results in different values of its magnetic permeability. In [79], it is shown that this change in the magnetic permeability is not linear and its change for different values of strain is presented (Figure 5.5.1, 'New approach' red curve). On the other hand, in Figure 4.3.1 can be seen a relationship between magnetic flux density on the surface of the MSM element, $B_{surface}$, and MSM's strain, ε.

To use the graphs in Figure 4.3.1 and Figure 5.5.1 in our analysis, it was needed to make data tables from both of them as these data have not been published. The obtained data table is presented in Appendix 5.

However, this is not sufficient to establish how the strain of a given MSM element will change with different values of the measured current for a given geometry, which is our goal. When the current changes, $B_{surface}$ also changes and thus, both the magnetic permeability and the strain of the MSM element will change as well. It is not straightforward to find a relationship between the change of current and the MSM element's strain as the relationship between $B_{surface}$ and MSM's relative magnetic permeability, μ_r is not known.

This was overcome by assuming the value of μ_r, and then obtaining the values of $B_{surface}$ and checking whether the strain was in accordance with the data obtained in [79] and shown in Figure 5.5.1, and matching the strain given by data curves shown in Figure 4.3.1. If these values did not match, another value of μ_r was assumed and the ANSYS simulation was run again for the same value of the current. This procedure was repeated until the value of the strain matched in both figures.

It was required to repeat this approach for each value of the current used in the simulation. Thus, several hundred simulations were carried out as the values of the amplitude current tested varied from 290 - 1400 A, with a step of 5 A. The results obtained are shown below (r = 55 mm, w = 20 mm, t = 35 mm). Figure 5.5.2 shows the relationship between the amplitude current, I_{amp} in the conductor and $B_{surface}$.

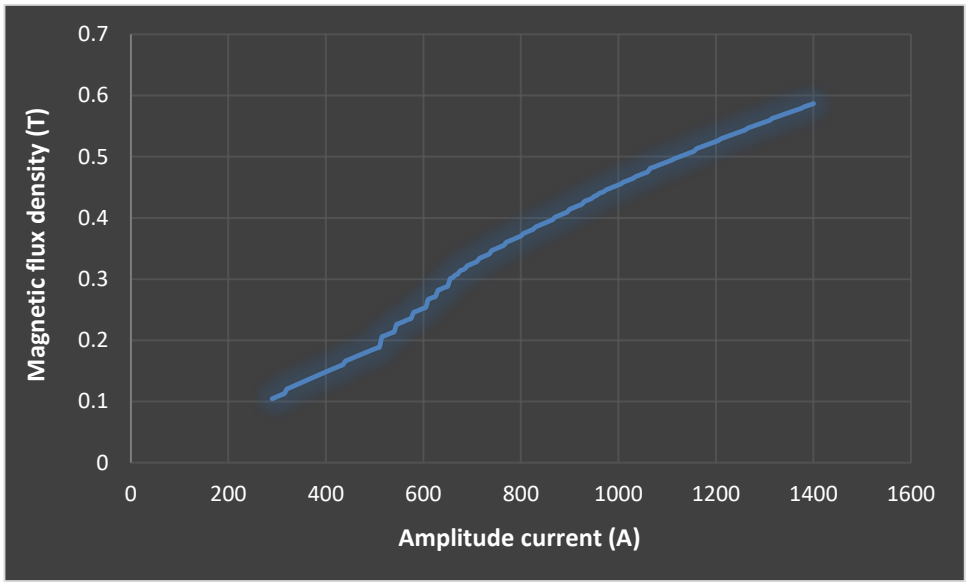

Figure 5.5.2 – Variation of magnetic flux density on the surface of the MSM element, $B_{surface}$ with amplitude current in the conductor, I_{amp} (r = 55 mm, w = 20 mm, t = 35 mm)

Finally, the relationship between the amplitude current I_{amp} in the conductor and strain ε of the MSM element is shown in Figure 5.5.3.

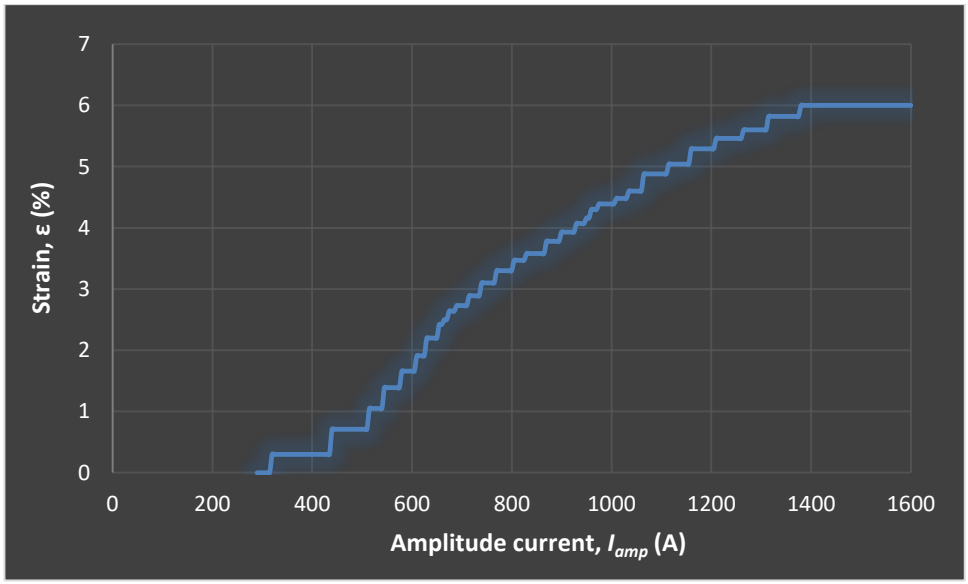

Figure 5.5.3 – Variation of strain of the MSM element, ε with amplitude current in the conductor I_{amp} (r = 55 mm, w = 20 mm, t = 35 mm)

By analysing the graph in Figure 5.5.3, several conclusions can be made. Besides the point when the MSM element saturates, these results show also, more precise data for the triggering point of the MSM element. It can be seen that an amplitude current of 330 A will

trigger the MSM element, but it will start to follow current changes for the amplitudes above 490 A.

Another point that should be noted in Figure 4.3.1 is that when the MSM material saturates and it does not elongate anymore at all. This is the point when the MSM element consists only of easy variants and there are no more hard variants that can rotate and thus increase the strain ε. This happens when the amplitude current reaches 1370 A for the given geometry.

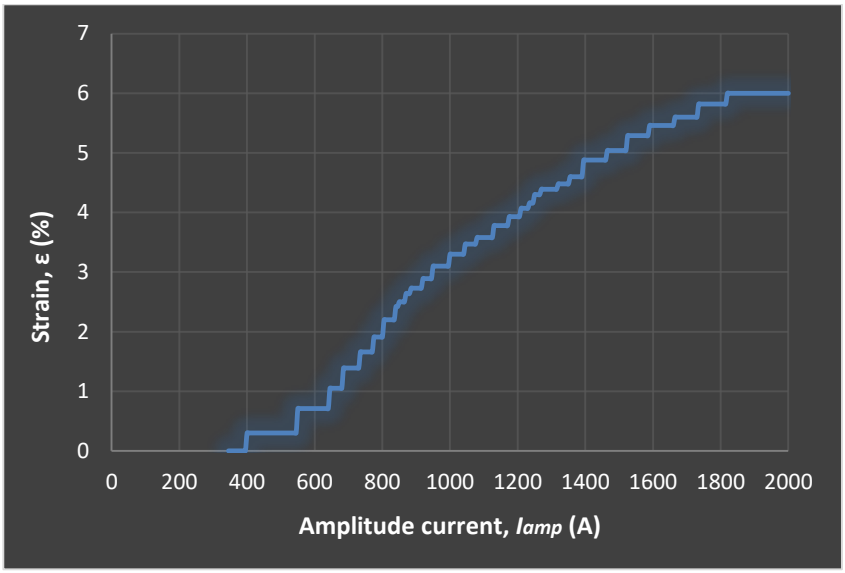

Figure 5.5.4 – Variation of strain of the MSM element, ε with amplitude current in the conductor I_{amp} (r = 80 mm, w = 20 mm, t = 50 mm)

Different measurement ranges can be achieved by changing the design of the NCIT. The procedures and simulations described above were repeated for several more geometries and some of the results can be seen in Table 5.9. Furthermore, as another example, variations of the strain of the MSM element with amplitude current in the conductor for the magnetic circuit with characteristics r = 80 mm, w = 20 mm, t = 50 mm are shown in Figure 5.5.4.

It can be seen that in this case, an amplitude current of 400 A will trigger the MSM element, but it will start to follow current changes for the amplitudes above 640 A. The MSM element saturates when the amplitude current is 1820A. In comparison to the previously described

case (r = 55 mm, w = 20 mm, t = 35 mm), this design provides measuring the wider current range. The MSM element will saturate later (I_{max} = 1820 A instead of I_{max} = 1370 A), but also only higher currents would be possible to measure (I_{min} = 550 A versus I_{min} = 490 A).

If this design (r = 80 mm, w = 20 mm, t = 50 mm) is compared to the one presented in Table 5.9 (r = 80 mm, w = 10 mm, t = 20 mm), it can be concluded that tapering the magnetic circuit and changing its width does not influence current range as much as changing its other dimensions, at the first place distance from the current-carrying conductor. Table 5.9 shows that the measuring range, in that case, would be 640A - 1830A.

Several more curves which show the variations of the strain with the current for various designs are presented in Figure 5.5.5. Their measurement current ranges are shown in Table 5.12.

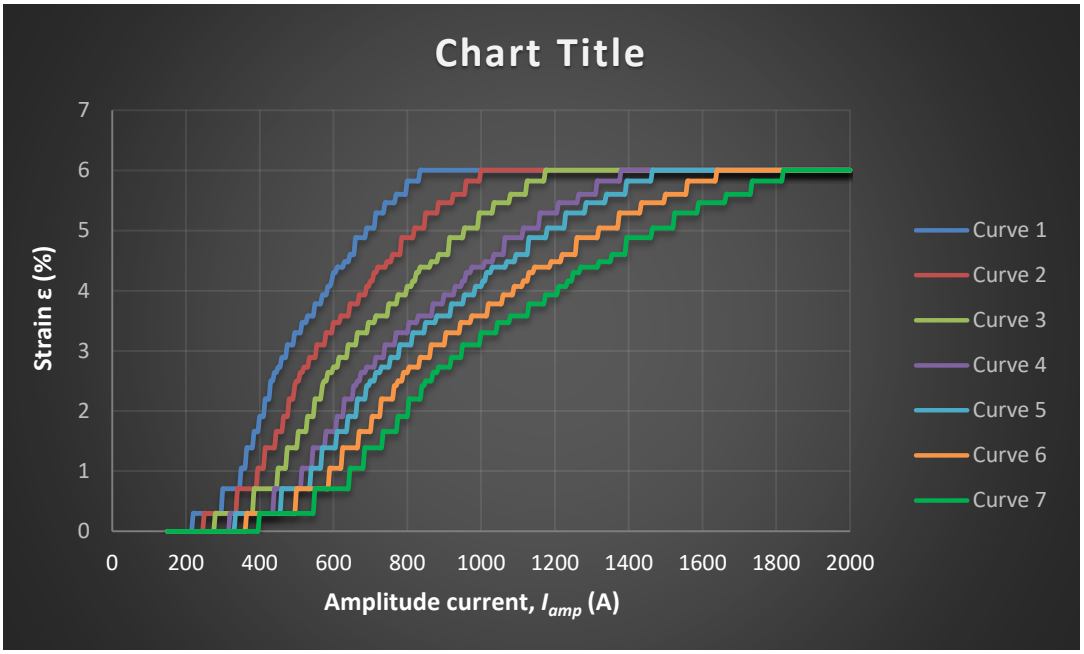

Figure 5.5.5 – Variation of the strain of the MSM element, ε with amplitude current I_{amp} for various designs of the magnetic circuit (Table 5.12)

Table 5.12 – Measurement range of amplitude currents for the various designs of the magnetic circuit shown Figure 5.5.5

	r	w	t	I_{trigg}	I_{min}	I_{max}
Curve 1	25	10	10	220	345	835
Curve 2	35	10	20	250	390	1000
Curve 3	45	10	30	290	460	1175
Curve 4	55	20	35	320	510	1380
Curve 5	60	20	40	335	535	1465
Curve 6	70	20	50	365	585	1640
Curve 7	80	20	50	400	640	1820

It should be noted here that the obtained results could be more precise if a smaller step of the current change has been taken in the simulations (it was 5A). However, decreasing the current step significantly increases the number of required simulations to be run. Furthermore, the values of $B_{surface}$, μ_r and ε had to be read from the graphs given in Figure 4.3.1 and in [79] as the data table spreadsheets are not officially published and thus not available. Although that also adds to the inaccuracy of the obtained results, nevertheless, they give a very good idea of the current range that can be measured for the given geometries of the proposed NCITs.

5.6. Estimation of modelling errors

There are two ways in ANSYS to control discretisation error in electromagnetic field analyses. The first of them is to control the tolerance of nodal solution (in this case magnetic vector potential). By default, this tolerance is 0.001.

In the electromagnetic analysis in ANSYS APDL, by using a macro called EMAGERR, it is possible to calculate the mesh discretisation errors for a given part of the model. Two

parameters are used to describe its value: B_{ei} - relative error for the magnetic flux density (magnitude) for element *i* and its normalised value, B_{nei}. They are calculated using equations (5.22) and (5.23), respectively.

$$B_{ei} = \frac{1}{n}\sum_{j=1}^{n}\left|B_j - B_{ij}\right| \tag{5.22}$$

where,

B_j – nodally averaged magnetic flux density (magnitude)

B_{ij} – magnetic flux density (magnitude) of element *i* at node *j*

$$B_{nei} = \frac{B_{ei}}{B_{max}} \tag{5.23}$$

where,

B_{max} - maximum nodally averaged magnetic flux density (magnitude)

The values of those two parameters have been calculated for each of the four materials that were defined in the model. Material 1 is the air around the conductor, material 2 are the aluminium strands inside the conductor, material 3 are the steel strands inside the conductor and material 4 is the air between the strands inside the conductor.

The maximum values of both parameters for each of these materials can be seen in Table 5.13. Those results show the maximum error for some element of a certain material, which means that all other elements of a certain material can have only smaller errors.

Table 5.13 – Error estimation of the obtained solutions

	Material 1	Material 2	Material 3	Material 4
$B_{ei\,max}$ [T]	$0.82 \cdot 10^{-6}$	$3.11 \cdot 10^{-6}$	$38.81 \cdot 10^{-6}$	$38.95 \cdot 10^{-6}$
$B_{nei\,max}$ [%]	0.0023	0.0086	0.1076	0.1080

According to ANSYSs APDL available documents and tutorials, only those two parameters (5.22 and 5.23) are available for error estimation in the case of electromagnetic field analysis. There are some additional parameters available for mechanical analysis (for example displacement-based problems) which can provide more precise error estimations.

These parameters are unfortunately not available for electromagnetic field-based problems, but the parameters mentioned above can also help give the overall picture of the correctness of the obtained solution. It should be noted once again that besides those two parameters, the tolerance of the nodal solution is always defined before solving the problem so the errors are controlled and limited in that way too.

Due to its geometry and the presence of several different materials, the airgap between the MSM element and the poles of the magnetic circuit is the most delicate part of the model. Since this airgap is of particular interest in obtaining the simulation results, B_{ei} and B_{nei} errors were calculated specifically for this part of the model.

The obtained results are valid within a material boundary and do not consider the error in the continuity of fields across dissimilar materials. Thus, in addition to B_{ei} and B_{nei}, the values of the normal component of B on the border between two materials (air in the airgap and Hiperco 50 in the magnetic circuit) needed to be evaluated, in order to control the error in the model. Although these values should be the same, it does not necessarily happen in FEM simulations. The relative error due to this discontinuity can be calculated using (5.24):

$$B_{nerr}\,[\%] = \frac{B_{nair} - B_{nmag}}{B_{nair}} \cdot 100 \qquad (5.24)$$

where,

B_{nair} – normal component of B in the airgap on the interface with the magnetic circuit;

B_{nmag} – normal component of B in the magnetic circuit on the interface with the airgap;

The values of the above parameters depend on the factors such as chosen geometry, fineness of the mesh, and loads. We developed and tested several models with different levels of mesh refinement.

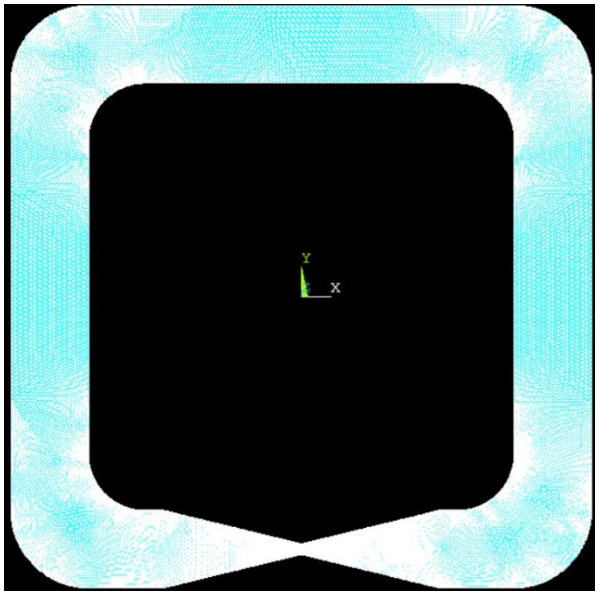

Figure 5.6.1 – Finite element mesh in the rectangular magnetic circuit with rounded corners (w = 20 mm, t = 35 mm, r = 55 mm)

The mesh of the rectangular magnetic circuit with rounded corners (I=400 A, w=20 mm, t=35 mm, r=55 mm) can be seen in Figure 5.6.1. Figure 5.6.2 shows the part of the mesh of the same circuit where the MSM element is placed (airgap) whereas the mesh of the airgap itself can be better seen in Figure 5.6.3.

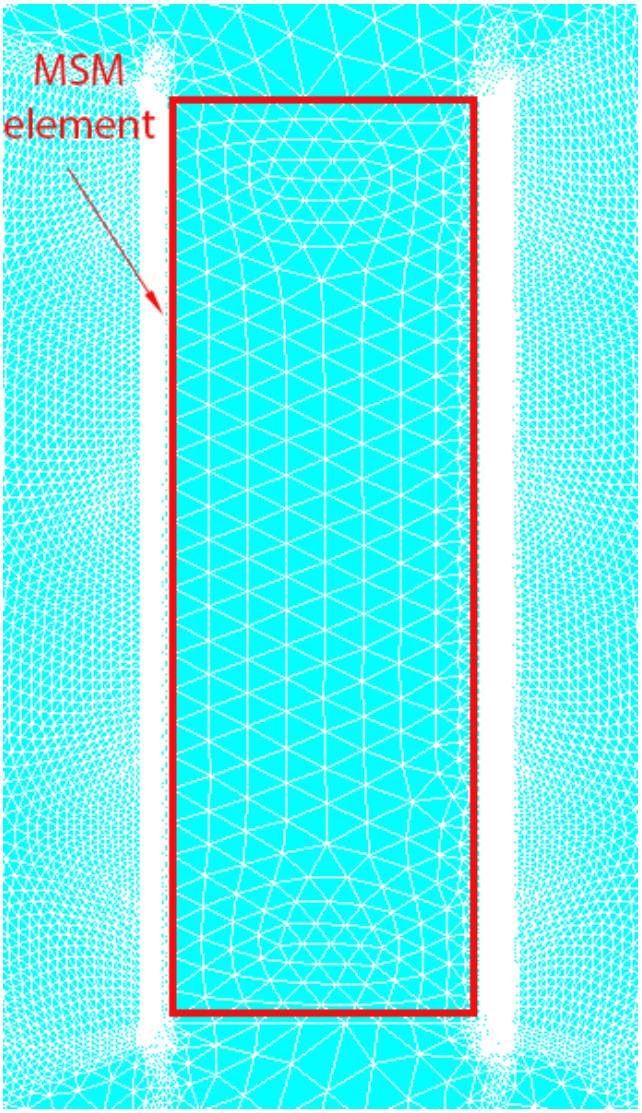

Figure 5.6.2 – Finite element mesh in rectangular magnetic circuit with rounded corners (w = 20 mm, t = 35 mm, r = 55 mm) - MSM element between the poles of the magnetic circuit

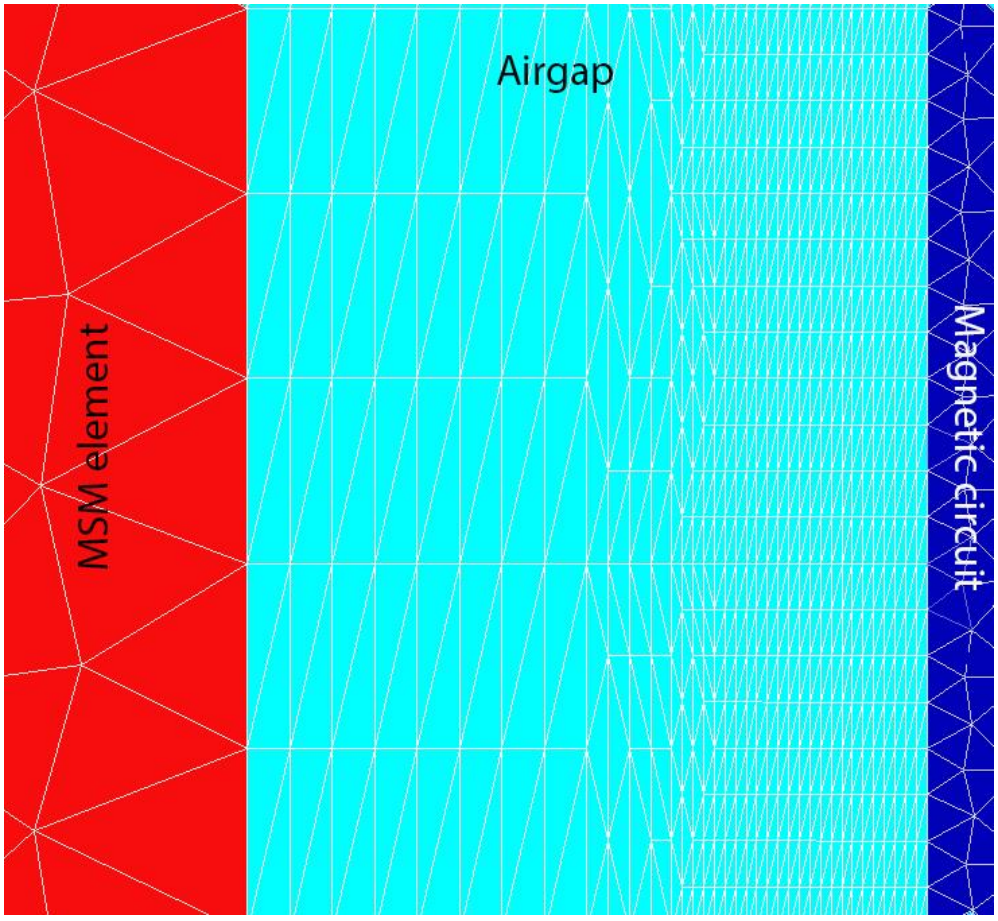

Figure 5.6.3 – Finite element mesh in rectangular magnetic circuit with rounded corners (w = 20 mm, t = 35 mm, r = 55 mm) - the airgap between the MSM element and the poles of the circuit

The maximum value of B_{nei} for this part was $B_{nei(max)}$ = 0.08824 and discontinuity on the interface was B_{nerr} = 0.66%. The model had 286188 FE elements in total out of which 95448 were in the airgaps between the MSM element and the poles of the magnetic circuit. This refined mesh was chosen to take into account the small airgap and the accuracy requirements for flux density calculation. An increase in the fineness of the mesh particularly affects the value of B_{nerr}. For example, this parameter took values from 13.56% for the mesh consisting of 14962 elements (525 elements in the airgap) to 0.66% for the presented case. At the same time, the range of B_{nei} was from 0.088-0.101. Although the number of elements in the model was relatively high, it should be mentioned that, for example, B_{nerr} = 2.97% was achieved with only 46500 elements in total (14482 in the airgap). Furthermore, it should be said that the convergence tolerance of the model was 0.001.

5.7. Results and discussion

Previously, we have shown that by using the proposed NCIT around overhead transmission lines, the MSM element can trigger an LVDT, together with presenting methodology and procedure to measure electrical current. We suggested several designs and showed the range of currents that could be measured. Our results were obtained by observing ETO MAGNETIC's elongation curves of MSM materials (Figure 4.3.1), whereas table data would provide more precise results if they were available. The blue curve in Figure 4.3.1 of load 0.5 N/mm^2 was chosen due to its lowest threshold for triggering the MSM element (reversibly) and large strain.

In Chapter 5.5, the correlation between the current inside the conductor and the strain of the MSM element was presented. For a commercially available LVDT, a linear relationship is specified between the input displacement (a strain of the MSM element in this case) and the voltage at its output. As this relationship is linear, it is easy to obtain a relationship between the current in the conductor and the voltage at the LVDT's output. Therefore, simply by measuring this voltage, it is possible to measure the current inside the conductor.

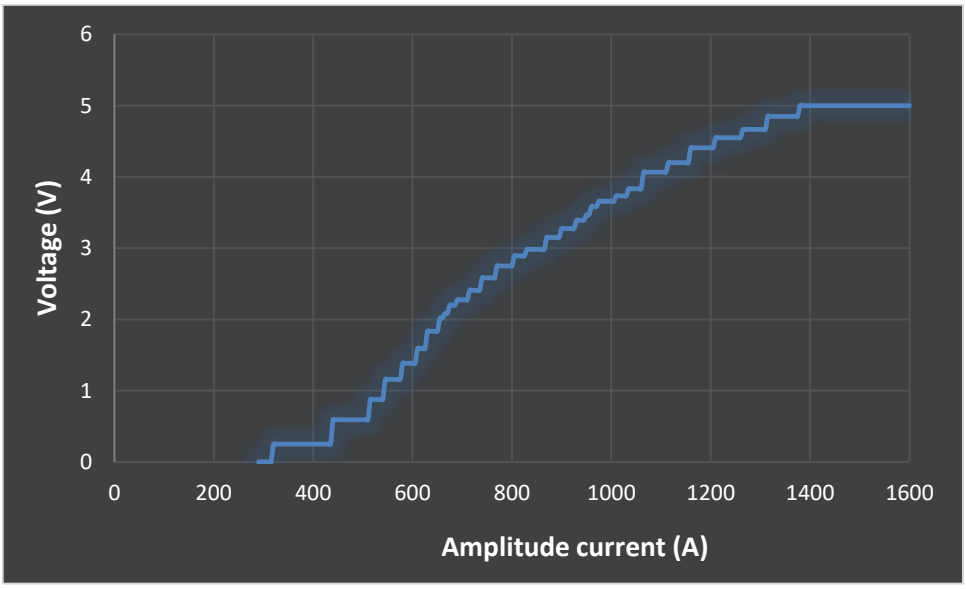

Figure 5.7.1 – Variation of voltage at the output of the LVDT with amplitude current in the conductor (r = 55 mm, w = 20 mm, t = 35 mm)

One of the suitable LVDTs for our application is a DC LVDT with an operating range of 0-5V. Using the results for the NCIT with a rectangular magnetic circuit with rounded corners (r = 55 mm, w = 20 mm, t = 35 mm) shown in Figure 5.5.3, it is possible to find which values at the output of the LVDT can be expected for the values of the current in the conductor in this case. This is shown in Figure 5.7.1.

As mentioned earlier, the obtained results could be more precise, and the obtained graph smoother if a smaller step of the current change was taken in the simulations. However, decreasing the current step significantly increases the number of required simulations, and already hundreds of simulations were required. As mentioned earlier, there are a few more factors that contribute to the inaccuracy of the obtained results (such as the non-availability of data table spreadsheets for the MSM parameters $B_{surface}$, μ_r and ε, unavoidable FEM modelling errors etc.). Nonetheless, the presented data give a good idea of the current range and values that can be measured for the given geometries of the proposed NCITs.

In our previous analysis, we observed the upward part of the blue curve of the strain-magnetic field relation (Figure 4.3.1). In future research, to get more precise results and measuring ranges, its downward part needs to be observed as well. The very similar analysis and methodologies presented for the upward part, need to be conducted for the downward return part of the hysteresis.

Since the MSM element with a load of 0.5 N/mm^2 does not fully compress, the strain of the whole MSM element is somewhat smaller than 6%. This will affect the expected measurement range (being somewhat smaller than predicted in the analysis for the upward curve), especially its bottom limit, as the minimum current that initiates a new elongation of the MSM element will be somewhat higher than for its initial elongation.

All designs and modelling in this research were made for MSM elements with type I twin boundaries, while less studied crystals with type II twin boundaries can be very promising for sensor applications. They offer even higher flexibility in the design of the proposed NCIT if their problem with twin microstructure instability is solved in the future.

5.8. Validation of results

In order to check and validate the methodology we have developed, as well as the obtained results (presented above), we compared them to results obtained through an experiment done by ETO MAGNETIC, the only global manufacturer of MSM materials.

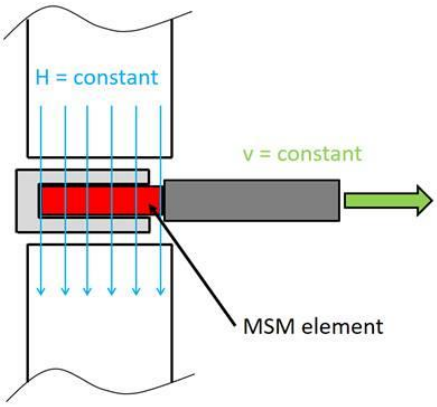

Figure 5.8.1 – The experimental setup [101]

In this experiment, a special test bench was used for the characterisation of an MSM element. The MSM element was connected to a push rod and exposed to a constant magnetic field (Figure 5.8.1). The push rod is blocked by a linear unit. This linear unit applies a constant slow motion so that the MSM element is able to elongate, making it possible to measure the quasi-static force-stroke characteristic. This procedure was repeated for several different values of a magnetic field. A force–stroke characteristic of the MSM element obtained through this experiment is shown in Figure 5.8.2. The size of the MSM element used in this case was 2.01 mm × 2.85 mm × 14.91 mm. [101]

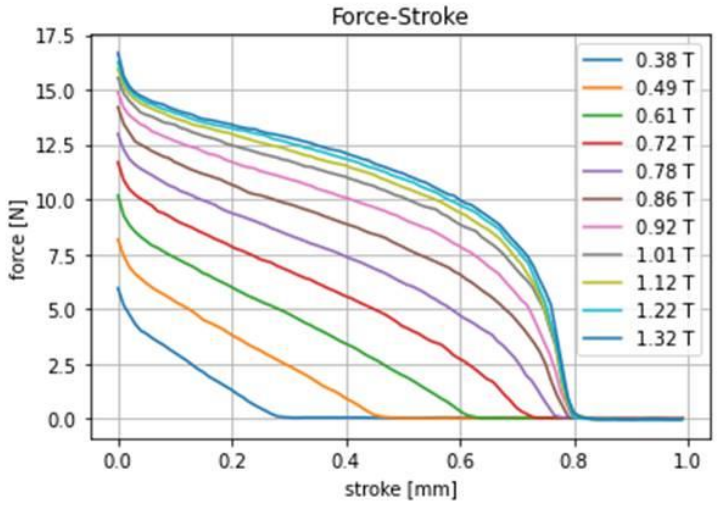

Figure 5.8.2 – Force–stroke characteristic of MSM element obtained through experiment [101]

The points on the curves where the force is zero show the maximum elongation of the MSM element for the applied magnetic field. By reading the values of the MSM's strokes at those points, δ_{exp}, and knowing the total length of the MSM element (14.91 mm), it is easy to calculate the experimentally obtained strains for those points, ε_{exp}, using the formula:

$$\varepsilon_{exp}\,[\%] = \frac{\delta_{exp}}{14.91} \cdot 100 \tag{5.25}$$

To verify our model, we used the same model as described in previous sections, but this time took into account the different size of the MSM element used in this experiment, and its different strain-magnetic field characteristics which are given in Figure 4.3.1 (return path of the yellow curve, load 2 N/mm^2). In our simulations, we would find the value of the current in the conductor that produces the same value of the magnetic field on the surface of the MSM element in the airgap as the value of the magnetic field used in this experiment. Then, by comparing the strain obtained in our model and the strain obtained in this experiment, we were able to make conclusions about the validity of our methodology and hence, the obtained results.

Table 5.14 shows the comparison between the results obtained in the experiment and our model. B is magnetic flux density and δ_{exp} and ε_{exp} are MSM's maximum stroke and maximum strain for the given magnetic field, respectively. ε_{sim} is the value of the strain obtained in our model. The last two columns show absolute and relative errors of the strains.

Table 5.14 – Comparison between the results obtained in the experiment and our model

B [T]	δ_{exp} [mm]	ε_{exp} [%]	ε_{sim} [%]	Absolute error (strain) [%]	Relative error (strain) [%]
0.38	0.30	2.02	1.76	0.26	13.05
0.49	0.47	3.18	2.92	0.26	8.18
0.61	0.63	4.24	4.4	-0.16	-3.86
0.72	0.74	4.98	5.67	-0.69	-13.89
0.78	0.78	5.25	5.97	-0.72	-13.72

By comparing the experimental results and the results of our model, it can be seen that the model follows the experimental data. As mentioned earlier, the table data of MSM characteristics were not available, which increased the values of the absolute and relative errors. Furthermore, the value of maximum magnetic permeability of the MSM alloy used in the experiment was μ_r=90 whereas our model used the value of μ_r=50 as per the data available for this research [101]. Moreover, magnetic flux density values were rounded to two decimal places in the available data of the experiment, and as a result, so were the values in the analysis of our model. That additionally contributes to the inaccuracy of the results.

Nevertheless, the obtained results show that our model can predict the elongation of the MSM element. Since the same methodology and the same models (with only different MSM element input characteristics) were used in the simulation of the described experiment, and in the above case of the proposed NCIT, it can be concluded that the proposed methodology and the developed model of the NCIT are valid. This example also shows the flexibility of the developed model and the possibility to make analyses for different MSM elements.

6. CONCLUSIONS

6.1. Conclusions and original contribution to knowledge

This PhD research aimed to mathematically model and design current sensing elements, specifically the current sensing element used in modern non-conventional instrument transformers. To achieve this, the primary objectives of the research were: (a) to develop methodologies for 2D/3D finite element modeling of low power current transformers, (b) to optimize the design and evaluate the performance of appropriate CTs using the models developed in (a), and (c) to validate the modeling results by comparing them with data obtained through experimental studies. In the process of achieving these objectives, other original contributions to knowledge have also been made.

- The research concluded that conventional instrument transformers are no longer able to meet modern requirements, and NCITs are the solution to this problem. Different solutions for current measurement were discussed, including optical current sensors, Rogowski coils, magnetic current sensors, and sensors based on the Hall Effect.
- The research also identified that special attention needed to be given to ACSR and AAAC conductors, more specifically to 528-Al1/69-ST1A conductor (old code MOOSE) and 996-AL5 (old code REDWOOD). ACSR is the most used conductor at the HV level and above. The two chosen conductors have the highest current ratings of all the conductors used in the UK.
- The research proposed the use of MSM alloys as a novel current measuring principle for NCITs, and identified 5M Ni-Mn-Ga MSM crystals with Type I twin boundaries as the most suitable type of MSM materials for this application. The combination of a very long fatigue life with relatively low twinning stress makes them the most prospective for use in MSM-based current sensors. Although 5M crystals with Type II twin boundaries possess very small twinning stress, resulting in better sensitivity and

the possibility to be triggered by weaker electromagnetic fields, they are currently very unstable.

Furthermore, the MSM element with a load of 0.5 N/mm^2 was found to be the best option for the proposed NCIT. It has the lowest threshold for triggering the MSM element (reversibly) and the largest strain, thus it would be possible to measure the lowest electromagnetic fields and the lowest currents in comparison to the MSM elements with different loads.

- It was shown that the MSM element by itself is not sensitive enough to measure AC inside overhead line conductors, even if it is placed near the surface of the conductor. This problem was overcome by developing, modelling, and optimising a magnetic concentrator which significantly improves its sensitivity, making it possible to achieve the aim of this research.

  However, once the MSM element is triggered, many other parameters need to be considered and analysed to obtain valid results. The significant changes take place within an MSM element during the elongation process which translates into the change in magnetic circuit parameters of the proposed sensor. Finding methodology to take this into account was crucial for capturing mutual influence between the MSM element, and the rest of the magnetic circuit.

- The proposed NCIT model, consisting of overhead line conductors, MSM elements, and a magnetic concentrator, was optimized for the transmission lines that was the primary objective of this research.

  Chapter 5 focused on modeling and evaluating the performance of the proposed NCIT using ANSYS APDL, and validated the modeling approach by comparing the obtained results with those obtained through other research. The developed model is flexible, and could simulate almost any overhead line conductor used in the world. It is also possible to model a wide range of different designs of the proposed NCIT just by slightly changing the developed code.

- The conductor, MSM element, and the magnetic circuit were included into a single finite element model. This allows us to find a relationship between the change of

current inside a conductor and the MSM element's strain. The model obtained can predict the bottom and upper limits of the measurement range of the proposed NCIT. As a result, it was possible to relate the current inside the conductor to the voltage at the output of the LVDT. An estimation of the model's performance was done and it was proved that the proposed current sensor can trigger LVDT, and thus, by measuring the voltage on LVDT's output, it is possible to measure current inside the conductor.

- The developed methodology and obtained results are validated by comparing them to the results obtained through an experiment done by a manufacturer of MSM materials, which was one of the objectives of this research. The obtained results show that our model can predict the elongation of the MSM element. The presented example also shows the flexibility of the developed model and the possibility to make analyses for different MSM elements.
- Several designs of the proposed current sensor that could be used to measure various ranges of AC in overhead transmission lines have been suggested. Additionally, possible routes for further development of the sensor have been discussed at the end of this dissertation.

In conclusion, this research successfully achieved its aim of mathematically modeling and designing the current sensing element used in modern non-conventional instrument transformers, by fulfilling its primary objectives of developing methodologies for finite element modeling, optimizing the design and evaluating the performance of CTs, and validating the modeling results through experimental studies. The research proposed the use of MSM alloys as a novel current measuring principle for NCITs, and provided insights into the most suitable conductors and transmission lines for their application. Finally, the developed model of the proposed NCIT was found to be flexible and adaptable to various designs and physical properties.

6.2. Significance of this research

This part of the thesis will highlight its significance and potential impact. This research study explored the application of magnetic shape memory alloys in the development of current sensors for non-conventional instrument transformers. By employing mathematical modeling techniques and innovative design strategies, this thesis aims to advance the field of electrical power systems and instrumentation. The following paragraphs highlight the key areas where this thesis will make a substantial impact on the academic, industrial, and technological fronts.

- Advancement in current sensing technology

  The research carried out in this PhD thesis pushes the boundaries of current sensing technology by proposing a novel approach utilizing MSMAs. Current sensors play a vital role in electrical power systems, providing accurate measurements necessary for monitoring, protection, and control. By introducing MSMAs as the sensing material, this research offers a promising alternative to conventional current sensing techniques, leading to improved accuracy, reliability, and efficiency in instrument transformers.

- Impact of NCITs on energy efficiency and grid stability

  The application of MSMAs in non-conventional instrument transformers represents a significant departure from traditional designs. Non-conventional instrument transformers offer advantages such as reduced size, enhanced reliability, and improved resistance to harsh operating environments. The integration of MSMAs into these transformers opens new avenues for creating compact, robust, and high-performance current sensors, addressing the limitations of existing technologies and supporting the development of smart grid systems.

  Accurate current measurement enables more precise control and monitoring of power flow, facilitating optimized energy management and reducing power losses. The enhanced performance of non-conventional instrument transformers based on MSMAs

can lead to more efficient energy distribution, reduced downtime, and improved overall grid stability.

- Enabling renewable energy integration

  The integration of renewable energy sources into the existing power grid presents significant challenges, particularly in terms of accurate current measurement. The novel design approaches and mathematical models presented in this thesis offer a potential solution for precise and reliable current sensing in NCITs. This integration of NCITs will facilitate the efficient integration of renewable energy sources, such as wind and solar, into the grid, supporting the global transition toward a clean energy future.

- Mathematical modeling for enhanced performance

  This thesis incorporates mathematical modeling techniques to develop a comprehensive understanding of the behavior of MSMAs under different operating conditions. By constructing mathematical models, the research enhances the prediction and optimization capabilities of the proposed current sensors. The accurate mathematical models developed in this study can guide the design process, facilitate performance evaluation, and enable the identification of optimal configurations, leading to superior current sensing performance.

- Technological Innovation and industrial applications

  The outcomes of this thesis have significant implications for industries involved in power generation, transmission, and distribution. The improved accuracy and efficiency of current sensors will enhance the performance of protection systems, monitoring networks, and fault detection mechanisms. Furthermore, the adoption of non-conventional instrument transformers will reduce the reliance on traditional, bulky, and maintenance-intensive systems, leading to cost savings and increased operational flexibility. This research will drive innovation and provide tangible benefits to electrical engineering companies, helping them stay at the forefront of technological advancements.

  The findings and innovations presented in this PhD thesis have the potential to stimulate technological advancements in the field of current sensing and non-conventional

instrument transformers. The novel use of MSMAs as sensing materials and the mathematical modeling approach provide valuable insights for researchers, engineers, and manufacturers working on similar projects. The outcomes of this research can facilitate the development of commercial products and applications, fostering collaborations between academia and industry.

This PhD thesis holds significant potential for advancing the field of electrical power systems and instrumentation. Through the utilization of MSMAs, mathematical modeling techniques, and the exploration of non-conventional instrument transformers, this research contributes to improving current sensing technology, energy efficiency, and grid stability. The outcomes of this study can inspire further research, drive technological innovation, and find practical applications in the industrial sector.

BIBLIOGRAPHY

[1] C. Lijuan, "Application comparison of Rogowski-type and optical-type electronic current transformer", *CICED International Conference*, pp. 1052-1057, Nanjing, China, 2010.

[2] P. M. Cavaleiro, F. M. Araújo, and A. B. L. Ribeiro, "Metal-coated fibre Bragg grating sensor for electric current metering," *Electron. Lett.*, vol. 34, no. 11, pp. 2–3, 1998.

[3] J. Mora, A. Diez, J. L. Cruz and M. V. Andres, "A magnetostrictive sensor interrogated by Fiber gratings for DC-current and temperature discrimination," *IEEE Photonics Technology Letters*, vol. 12, no. 12, pp. 1680–1682, 2001. 10.1109/68.896347.

[4] L. Dziuda, G. Fusiek, P. Niewczas, G. M. Burt and J. R. McDonald, "Laboratory evaluation of the hybrid fiber-optic current sensor," *Sensors Actuators, A Phys.*, vol. 136. no. 1, pp. 184–190, 2007.

[5] C. Chin-Hsing, C. Ming-Hsien, and L. Wen-Fung, "Measurement of AC Current Using a Superstructure Fiber Grating," *Microw. Opt. Technol. Lett.*, vol. 50, no. 5, pp. 1168–1171, 2008.

[6] Y. Zhao, Q. Meng, and K. Chen, "Novel current measurement method based on fiber Bragg grating sensor technology," *Sensors Actuators A Phys.*, vol. 126, no. 1, pp. 112–116, 2006.

[7] J. Mora, L. Martínez-León, a. Díez, J. L. Cruz, and M. V. Andrés, "Simultaneous temperature and ac-current measurements for high voltage lines using fiber Bragg gratings," *Sensors Actuators A Phys.*, vol. 125, no. 2, pp. 313–316, 2006.

[8] D. Satpathi, J. A. Moore, and M. G. Ennis, "Design of a Terfenol-D based fiber-optic current transducer," *IEEE Sens. J.*, vol. 5, no. 5, pp. 1057–1065, 2005.

[9] J. Močnik, J. Humar, and A. Žemva, "A non-conventional instrument transformer," *Measurement,* vol. 46, no. 10, pp. 4114–4120, 2013. https://doi.org/10.1016/j.measurement.2013.08.011.

[10] B.-O. Guan and S.-N. Wang, “Fiber grating laser current sensor based on magnetic force,” *IEEE Photonics Technol. Lett.*, vol. 22, no. 4, pp. 230–232, 2010.

[11] J. L. Camas-Anzueto *et al.*, “Novel approach to indirect measurements of alternating current based on the interrogation of an all-fiber laser,” *Meas. J. Int. Meas. Confed.*, vol. 46, no. 10, pp. 4108–4113, 2013.

[12] G. K. Singh and G. Krishnamurthy, “Novel method for current measurement using single mode fiber,” *Int. J. Eng. Sci. Res. Technol.*, vol. 2, no. 8, 2013.

[13] L. Wang, B. Wang, L. Weng, Z. Wang and W. Huang, "Large current measurements using a fibre optics current sensor," *Proceedings of the 10th World Congress on Intelligent Control and Automation*, Beijing, China, 2012, pp. 4337-4340, doi: 10.1109/WCICA.2012.6359209.

[14] Y. W. Lee, I. Yoon, and B. Lee, “A simple fiber-optic current sensor using a long-period fiber grating inscribed on a polarization-maintaining fiber as a sensor demodulator,” *Sensors Actuators, A Phys.*, vol. 112, no. 2–3, pp. 308–312, 2004.

[15] H. Kirkham, “Current measurement methods for the smart grid,” *2009 IEEE Power Energy Soc. Gen. Meet.*, pp. 1–7, 2009.

[16] K. Thyagarajan and A. Ghatak, "Fiber Bragg gratings," in *Fibre Optic Essentials*, 1st ed. Hoboken, NJ, USA: John Wiley & Sons, Inc., 2007, ch. 7, pp. 195-222.

[17] J. Wang, F. Viawan, and T. Werner, “Effects of sensor technology on differential protection,” in *10th IET International Conference on Developments in Power System Protection*, 2010, pp. 1–5.

[18] J. Lenz and S. Edelstein, “Magnetic sensors and their applications,” *IEEE Sens. J.*, vol. 6, no. 3, pp. 631–649, 2006.

[19] I. A. Metwally, “Self-integrating Rogowski coil for high-impulse current measurement,” *IEEE Trans. Instrum. Meas.*, vol. 59, no. 2, pp. 353–360, 2010.

[20] L. A. Kojovic and M. T. Bishop, “Comparative characteristics of iron-core current transformers and Rogowski coils for applications for protective relaying purposes,” *2009 62nd Annu. Conf. Prot. Relay Eng.*, pp. 527–535, 2009.

[21] L. A. Kojovic, “Comparative performance characteristics of current transformers and non-conventional current sensors,” in *CIRED 20th International Conference on Electricity Distribution*, 2009, Prague, Czech Republic. no. 36.

[22] G. Frolov, O. Grudin, and T. Warland, “Compensating Rogowski coils for current measurement,” *Electron. Eng. Times*, no. 1511, pp. 31–32, 2008.

[23] Ming Zhang, K. Li, S. He, and J. Wang, “Design and Test of a New High-Current Electronic Current Transformer With a Rogowski Coil,” *Metrol. Meas. Syst.*, vol. 21, no. 1, pp. 121–132, 2013.

[24] P. Orr *et al.*, “An optically-interrogated Rogowski coil for passive, multiplexable current measurement,” *IEEE Sens. J.*, vol. 13, no. 6, pp. 2053–2054, 2013.

[25] L. A. Kojovic and R. Beresh, "Practical Aspects of Rogowski Coil Applications to Relaying," in Proc. 2010 *IEEE Power & Energy Society General Meeting*, Minneapolis, MN, USA, 2010, pp. 1-8.

[26] “Submetersolutions” [Online]

Available: https://submetersolutions.com/images/product/rocoil_2.jpeg. [Accessed: Apr. 12, 2021].

[27] S. Dong, J. F. Li, and D. Viehland, “Ultrahigh magnetic field sensitivity in laminates of TERFENOL-D and Pb(Mg1/3Nb2/3)O3-PbTiO3 crystals,” *Appl. Phys. Lett.*, vol. 83, no. 11, pp. 2265–2267, 2003.

[28] J. Ryu, S. Priya, K. Uchino, and H.-E. Kim, “Magnetoelectric effect in composites of magnetostrictive and piezoelectric materials,” *J. Electroceramics*, vol. 8, pp. 107–119, 2002.

[29] J. C. Peuzin, "Magnetostrictive Materials," in *Magnetostrictive Materials*, Elsevier Ltd, 2001, ch. 18.

[30] F. T. Calkins, A. B. Flatau, and M. J. Dapino, “Overview of magnetostrictive sensor technology,” *J. Intell. Mater. Syst. Struct.*, vol. 18, no. 10, pp. 1057–1066, 2007.

[31] G. P. Mccombe, J. A. Etches, I. P. Bond, and P. H. Mellor, “Magnetostrictive actuation of fiber-reinforced polymer composites,” *J. Intell. Mater. Syst. Struct.*, vol. 20, no. 10, pp. 1249–1257, 2009.

[32] X. Z. Zhou, C. Yu, Z. Y. Tang, C. P. Zhao, and H. Yan, “Wiedemann effect in Fe83Ga17 alloys for magnetostrictive sensors,” *IEEE Sens. J.*, vol. 14, no. 1, pp. 249–257, 2014.

[33] J. He, O. Yong, J. Hu, and S. Wang, “Giant Magnetoresistance Current Sensor,” US Patent Application 20130049750A1, 2013.

[34] S. S. P. Parkin *et al.*, “Giant tunnelling magnetoresistance at room temperature with MgO (100) tunnel barriers,” *Nat. Mater.*, vol. 3, no. 12, pp. 862–867, 2004.

[35] S. Yuasa, T. Nagahama, A. Fukushima, Y. Suzuki, and K. Ando, “Giant room-temperature magnetoresistance in single-crystal Fe/MgO/Fe magnetic tunnel junctions,” *Nat. Mater.*, vol. 3, no. 12, pp. 868–871, 2004.

[36] E. Ramsden, "Current-Sensing Techniques," in *Hall-Effect Sensors - Theory and Application*, Elsevier Ltd, 2006, pp. 131-150.

[37] Y. P. Tsai, K. L. Chen, Y. R. Chen, and N. Chen, “Multifunctional coreless hall-effect current transformer for the protection and measurement of power systems,” *IEEE Trans. Instrum. Meas.*, vol. 63, no. 3, pp. 557–565, 2014.

[38] M. Pastre and M. Kayal, "A Hall sensor-based current measurement microsystem with continuous gain calibration," in *Proceedings of 2005 PhD Research in Microelectronics and Electronics*, vol. II, pp. 295-298, 2005.

[39] A. Ajbl, M. Pastre, and M. Kayal, “A fully integrated hall sensor microsystem for contactless current measurement,” *IEEE Sens. J.*, vol. 13, no. 6, pp. 2271–2278, 2013.

[40] K.-L. Chen and N. Chen, “A new method for power current measurement using a coreless Hall effect current transformer,” *Instrum. Meas. IEEE Trans.*, vol. 60, no. 1, pp. 158–169, 2011.

[41] L. Cristaldi, A. Ferrero, M. Lazzaroni, and R. Ottoboni, “A linearization method for commercial Hall-effect current transducers,” *IEEE Trans. Instrum. Meas.*, vol. 50, no. 5, pp. 1149–1153, 2001.

[42] Northern Ireland Electricity and EirGrid, “Cavan-Tyrone and Meath-Cavan 400KV Transmission Circuits,” 2009, ch.2.

[43] C. R. Bayliss and B. J. Hardy, "Overhead Line Conductor and Technical Specifications," in *Transmission and Distribution Electrical Engineering*, Elsevier Ltd, 2012, pp. 683–750.

[44] British Standards Institution, "BS EN 50182:2001 Conductors for Overhead Lines - Round Wire Concentric Lay Stranded Conductors," London, England, 2013, pp. 27-74.

[45] British Standards Institution, "BS EN 50183:2000 Conductors for Overhead Lines - Aluminium-magnesium-silicon alloy wires," London, England, 2013.

[46] R. N. Nayak, Y. K. Sehgal, and S. Sen, “EHV transmission line capacity enhancement through increase in surge impedance loading level,” *2006 IEEE Power India Conf.*, vol. 2005, pp. 858–861, 2005.

[47] V. Patel and J. G. Jamnani, “Techniques to increase surge impedance Loading level of EHV AC transmission lines for improving power transfer capability,” *4th IEEE Spons. Int. Conf. Comput. Power, Energy, Inf. Commun. ICCPEIC 2015*, pp. 518–523, 2015.

[48] R. D. Begamudre, "Extra High Voltage Cable Transmission," in *Extra High Voltage AC Transmission Engineering*, New Age International (p) Limited, 2006, ch. 15, pp. 429-481.

[49] R. Lings, “Overview of transmission lines above 700 kV,” in *2005 IEEE Power Engineering Society Inaugural Conference and Exposition in Africa*, 2005, pp. 11–15.

[50] Z. Liang, Y. Li, H. Hu, and J. J. China, “Design of UHVAC transmission line in China Zheng-ping,” *Eur. Trans. Electr. Power*, vol. 22, pp. 4–16, 2012.

[51] Argonne National Laboratory, "China’s Ultra-High Voltage Technology and Global Standards," 2015. [Online]. Available:

https://www.anl.gov/file/8766/download?token=-e-ucdJS. [Accessed: Apr. 26, 2023].

[52] D. J. Holtzhausen and D. W. Vosloo, "High Voltage Insulating Materials," in *High Voltage Engineering Practice and Theory*, 1st ed. Newnes, 2009, ch. 5, pp. 143-180.

[53] L. Colla, F. M. Gatta, F. Iliceto, and S. Lauria, “Design and operation of EHV transmission lines including long insulated cable and overhead sections,” *2005 Int. Power Eng. Conf.*, pp. 1–10, 2005.

[54] Z. Xu, Z. Gao, and C. Zhou, "EHV/UHV AC Transmission Capability Analysis," *Proceedings of the CSEE*, vol. 22, no. 6, pp. 51-57, 2002

[55] I. S. Grant and J.R. Stewart, “Mechanical and electrical characteristics of EHV high phase order overhead transmission,” *IEEE Trans. Power Appar. Syst.*, vol. 103, no. 11, 1984.

[56] J. G. Anderson and L. E. Zaffanella, "Project UHV Test Line Research on the Corona Performance of Transmission Lines," in *IEEE Power Engineering Society Transmission and Distribution Committee*, Winter Power Meeting, 1971.

[57] J. G. Anderson, L. E. Zaffanella, G. W. Juette, and J. R. Stevenson, "Ultrahigh-Voltage Power Transmission," *IEEE Spectrum*, vol. 59, no. 11, 1971.

[58] C. Garrido and A. F. Otero, “Ampacity and Temperature in ACSR Overhead Conductors in Emergency Situations,” *Eur. Congr. Comput. Methods Appl. Sci. Eng.*, 2000.

[59] D. Lauria and S. Quaia, “Loadability of 400 kV four-bundled overhead transmission lines,” in *5th International Conference on Clean Electrical Power: Renewable Energy Resources Impact, ICCEP 2015*, 2015, pp. 160–164.

[60] Siemens, “Power engineering guide, power transmission and distribution solutions., Edition 7.0,” pp. 14–63, 2012.

[61] H. N. Scherer and G. S. Vassell, “Transmission of electric power at ultra-high voltages: current status and future prospects,” *Proc. IEEE*, vol. 73, no. 8, pp. 1252–1278, 1985.

[62] British Standards Institution, "Glossary of electrotechnical, power, telecommunication, electronics, lighting and colourtTerms - Group 15: Overhead Lines," *BS 4727-2*, vol. 50,

no. 321, 1991.

[63] British Standards Institution, "Conductors for overhead Lines - Zinc coated steel wires," *BS EN 50189:2000*, London, England: BSI, 2013.

[64] British Standards Institution, "Conductors for overhead Lines - Characteristics of reases," *BS EN 50326:2002*, London, England: BSI, 2013.

[65] British Standards Institution, "Hard drawn aluminium wire for overhead line conductors," *BS EN 60889:1997,* London, England: BSI, 2013.

[66] British Standards Institution, "Aluminium-clad steel wires for electrical purposes," *BS EN 61232:1997*, London, England: BSI, 2013.

[67] British Standards Institution, "General purpose galvanized steel wire strand," *BS 183:1972*, London, England: BSI, 2013.

[68] L. Weimers, “Bulk power transmission at extra high voltages, a comparison between transmission lines for HVDC at voltages above 600 kV DC and 800 kV AC,” *Indian J. Power River Val. Dev.*, vol. 61, no. 7, p. 107, 2011.

[69] J. Graham, S. E. Santo, and A. Kumar, “Comparison of the performance of HVDC and HVAC overhead transmission lines for the Itaipu system,” in *GridTech*, 2013.

[70] B.P.Lebedev and S.S. Rokotian, “EHV transmission in the U.S.S:R grid,” *IEE Spectr.*, pp. 73–79, 1967.

[71] A.Fakheri and J:C.Haahr, “Experience with the AEP 765-kV system Dumont - Marysville - Kammer field tests,” *IEEE Trans. Power Appar. Syst.*, vol. 97, no. 1, pp. 109–117, 1978.

[72] D. M. Larruskain, I. Marene, J. Zamora, O. Abarrategui, A. Iraolagoitia, M. Gutiérrez, E. Loroño, and F. Bodega, "Power transmission capacity upgrade of overhead lines," *Electricity Today*, vol. 19, pp. 1-8, 2007, doi: 10.24084/repqj04.296.

[73] S. J. Murray, M. Marioni, S. M. Allen, R. C. O’Handley, and T. A. Lograsso, “6% magnetic-field-induced strain by twin-boundary motion in ferromagnetic Ni–Mn–Ga,” *Appl. Phys. Lett.*, vol. 77, no. 6, p. 886, 2000.

[74] W. Z. A. Sozinov, N. Lanska, A. Soroka, “12% magnetic field-induced strain in Ni-Mn-Ga-based non-modulated martensite,” *Appl. Phys. Lett.*, vol. 102, no. 2, p. 21902, 2013.

[75] A. M. R. J. M. Stephan, E. Pagounis, M. Laufenberg, O. Paul, and P. Ruther, "A novel concept for strain sensing based on the ferromagnetic shape memory alloy nimnga," *IEEE Sensors Journal*, vol. 11, no. 11, pp. 2683-2689, Nov. 2011, doi: 10.1109/JSEN.2011.2158123..

[76] O. Heczko, “Determination of ordinary magnetostriction in Ni-Mn-Ga magnetic shape memory alloy,” *J. Magn. Mater.*, vol. 290–291, pp. 846–849, 2005.

[77] E. Pagounis and P. Müllner, "Recent Developments in Magnetic Shape Memory Actuation," in *Proceedings of the 15th International Conference on New Actuators (Actuator)*, pp. 86-91, June 2014.

[78] H. S. O. Heczko, V. Kopecky, L. Fekete, K. Jurek, J. Kopecek, and L. Straka, "Magnetic domains and twin microstructure of single crystal Ni-Mn-Ga exhibiting magnetic shape memory effect," *IEEE Trans. Magn.*, vol. 51, no. 11, pp. 15–18, Nov. 2015.

[79] Nikita Gabdullin, “Modelling and design of high-speed, long-lifetime and large-force electromagnetic actuators based on magnetic shape memory alloys”, *Ph.D. dissertation,* City, University of London, 2017.

[80] P. M. S. Barker, E. Rhoads, P. Lindquist, M. Vreugdenhill, “Micropump utilizing localized magnetic-field-induced deformation of MSM elements to deliver sub-microliter volumes of drugs to the rat brain,” *Proc. Actuator*, pp. 96–97, 2014.

[81] Jhih-Hong Lin and Mao-Hsiung Chiang, “Hysteresis analysis and positioning control for a magnetic shape memory actuator”, *Sensors*, volume 15, issue 4, pp. 8054-8071, 2015

[82] M. L. E. Pagounis, R. Chulist, M. J. Szczerba, “High-temperature magnetic shape memory actuation in a Ni–Mn–Ga single crystal,” *Scr. Mater.*, vol. 83, pp. 29–32, 2014.

[83] EtoMagnetic, "Magnetic Shape Memory Technology (MAGNETOSHAPE)," [Online]. Available: http://etogroup.com/MAGNETOSHAPE_EN.html. [Accessed: Apr. 30, 2023].

[84] B. Nikolić, S. Khan, and N. Gabdullin, “Development of non-conventional instrument transformers (NCIT) using smart materials,” *J. Phys. Conf. Ser.*, vol. 772, p. 12065, 2016.

[85] L. Straka, A. Soroka, H. Seiner, H. Hänninen, and A. Sozinov, “Temperature dependence of twinning stress of Type I and Type II twins in 10M modulated Ni-Mn-Ga martensite,” *Scr. Mater.*, vol. 67, no. 1, pp. 25–28, 2012.

[86] D. Kellis, A. Smith, K. Ullakko, and P. Müllner, “Oriented single crystals of Ni-Mn-Ga with very low switching field,” *J. Cryst. Growth*, vol. 359, no. 1, pp. 64–68, 2012.

[87] I. Aaltio *et al.*, “Crack growth of 10M Ni-Mn-Ga material in cyclic mechanical loading,” *Phys. Procedia*, vol. 10, pp. 87–93, 2010.

[88] Motioncontroltips, "What is an LVDT? Linear Variable Differential Transformer," [Online]. Available: https://www.motioncontroltips.com/what-is-an-lvdt-linear-variable-differential-transformer. [Accessed: Apr. 30, 2023].

[89] A. S. Morris and R. Langari, "Measurement and instrumentation: theory and application," 2nd ed. *Academic Press,* 2016, ch. Sensor Technologies, pp. 317-345.

[90] W. Bolton, "Measurement Case Studies," in Instrumentation and Control Systems, 2nd ed., *Elsevier Science,* 2015, ch. 15, pp. 373-397.

[91] C. Erdonmez and C. E. Imrak, "A finite element model for independent wire rope core," *Journal of Mechanical Science and Technology,* vol. 25, no. 12, pp. 995-1008, Dec. 2011.

[92] E. Stanova, G. Fedorko, M. Fabian, and S. Kmet, “Computer modelling of wire strands and ropes Part I: Theory and computer implementation,” *Adv. Eng. Softw.*, vol. 42, no. 6, pp. 305–315, 2011.

[93] S. Moaveni, "Design Optimization," in Finite Element Analysis: Theory and Application with ANSYS, 3rd ed. *Pearson Prentice Hall*, 2008, ch. 13, pp. 497-534.

[94] Oszkar Biro and Kurt Preis, "On the use of the magnetic vector potential in the finite element analysis of three-dimensional eddy currents," *IEEE Transactions on*

Magnetics. vol. 25, No. 4. 3145-3159, 1989.

[95] ANSYS, “ANSYS Mechanical APDL theory reference,” *ANSYS Inc*, vol. Release15, pp. 1–909, 2013.

[96] J. J. LaForest et al., "EHV-UHV Transmission systems," in Transmission Line Reference Book: 345 kV and Above 2nd Edition, pp. 31-88. New York, NY, *USA: American Electric Power Company*, Inc., 1982.

[97] N.A. Demerdash and D.H. Gillott, "A new approach for determination of eddy currents and flux penetration in nonlinear ferromagnetic materials", *IEEE Trans. on Magnetics*, Vol. 10, pp. 682-685, 1974

[98] S. H. Khan, K.T.V. Grattan, and J.R.Attwood, "Finite element modelling of skin and proximity effects in high voltage power cables", *Proceedings of the International Conference on the Computation of Electromagnetic Fields*, *COMPUMAG*, Evian, 2-5 July 2001, 26-47.

[99] S. H. Khan, K.T.V. Grattan, and J.R.Attwood, "Calculation of skin and proximity effects in solid conductors – comparison of analytical and numerical techniques", *in Studies in Applied Electromagnetics and Mechanics* 18, eds.P. Di Barba and A. Savini, IOS Press, The Netherlands, 2000, pp. 165-168

[100] K. Kajan, “Finite element modelling and invesigation of high speed, large force and long lifetime electromagnetic actuators,” *Ph.D. dissertation*, City, University of London, England, 2009

[101] Provided by courtesy of ETO MAGNETIC, 2022.

Appendix 1. Lay ratios for various types of conductors

Table A1 – Lay ratios used for calculation of increments due to stranding [44]

Aluminium wires		Steel wires		Lay ratio							
No.	Layers	No.	Layers	1	2	3	4	5	6	7	8
7	1	-	-	13	-	-	-	-	-	-	-
19	2	-	-	15	12	-	-	-	-	-	-
37	3	-	-	15	13.5	11.5	-	-	-	-	-
61	4	-	-	15	13.5	12.5	11	-	-	-	-
91	5	-	-	15	13.5	12.5	11	10.5	-	-	-
127	6	-	-	15	14.5	13.5	12	11.5	10.5	-	-
6	1	1	-	12.5	-	-	-	-	-	-	-
8	1	1	-	12.5	-	-	-	-	-	-	-
18	2	1	-	14	12	-	-	-	-	-	-
9	1	3	1	19	12	-	-	-	-	-	-
6	1	7	1	19	12	-	-	-	-	-	-
10	1	7	1	19	12	-	-	-	-	-	-
12	1	7	1	19	12	-	-	-	-	-	-
14	1	7	1	19	12	-	-	-	-	-	-
18	2	7	1	19	14	11.5	-	-	-	-	-
22	2	7	1	19	14	11.5	-	-	-	-	-
24	2	7	1	19	14	11.5	-	-	-	-	-
26	2	7	1	19	14	11.5	-	-	-	-	-
28	2	7	1	19	14	11.5	-	-	-	-	-
30	2	7	1	19	14	11.5	-	-	-	-	-
32	2	7	1	19	14	11.5	-	-	-	-	-
36	2	7	1	19	14	11.5	-	-	-	-	-
42	3	7	1	19	15	13	11.5	-	-	-	-
45	3	7	1	19	15	13	11.5	-	-	-	-
48	3	7	1	19	15	13	11.5	-	-	-	-
54	3	7	1	19	15	13	11.5	-	-	-	-
72	4	7	1	19	15.5	13.5	12	11.5	-	-	-
84	4	7	1	19	15.5	13.5	12	11.5	-	-	-
14	1	19	2	20	17.5	11.5	-	-	-	-	-
15	1	19	2	20	17.5	11.5	-	-	-	-	-
16	1	19	2	20	17.5	11.5	-	-	-	-	-
18	1	19	2	20	17.5	11.5	-	-	-	-	-
30	2	19	2	20	17	13	11.5	-	-	-	-
32	2	19	2	20	17	13	11.5	-	-	-	-
36	2	19	2	20	17	13	11.5	-	-	-	-
42	2	19	2	20	17	13	11.5	-	-	-	-
54	3	19	2	20	18	15	13.5	11.5	-	-	-
38+22	3	19	2	20	18	15	13.5	11.5	-	-	-
42+20	3	19	2	20	18	15	13.5	11.5	-	-	-
66	3	19	2	20	18	15	13.5	11.5	-	-	-
78	3	19	2	20	18	15	13.5	11.5	-	-	-
96	4	19	2	20	18	15	13.5	12.5	11.5	-	-
100	4	19	2	20	18	15	13.5	12.5	11.5	-	-
18	1	37	3	20	18	16	11.5	-	-	-	-
24	1	37	3	20	18	16	11.5	-	-	-	-

72	3	37	3	22	19	17	15	13	11.5	-	-
54+66	4	37	3	24	20	18	16.5	15	12.5	11.5	-
150	5	37	3	24	20	18	16.5	15	14	12.5	11.5
Note: For more accurate calculations, measured values may be used.											

Appendix 2. ACSR conductors used in the UK (type AL1/ST1A)

Table A2 – Characteristics of ACSR conductors used in the UK (type AL1/ST1A) [44]

Code	Old code	Areas			No. of wires		Wire diameter		Diameter		Mass per unit length	Rated strength	DC resistance
		Al	Steel	Total	Al	Steel	Al	Steel	Core	Cond.			
		mm²	mm²	mm²			mm	mm	mm	mm	kg/km	kN	Ω/km
11-AL1/2-ST1A	MOLE	10,6	1,77	12,4	6	1	1,50	1,50	1,50	4,50	42,8	4,14	2,702 7
21-AL1/3-ST1A	SQUIRREL	21,0	3,50	24,5	6	1	2,11	2,11	2,11	6,33	84,7	7,87	1,365 9
26-AL1/4-ST1A	GOPHER	26,2	4,37	30,6	6	1	2,36	2,36	2,36	7,08	106,0	9,58	1,091 9
32-AL1/5-ST1A	WEASEL	31,6	5,27	36,9	6	1	2,59	2,59	2,59	7,77	127,6	11,38	0,906 5
37-AL1/6-ST1A	FOX	36,7	6,11	42,8	6	1	2,79	2,79	2,79	8,37	148,1	13,21	0,781 2
42-AL1/7-ST1A	FERRET	42,4	7,07	49,5	6	1	3,00	3,00	3,00	9,00	171,2	15,27	0,675 7
53-AL1/9-ST1A	RABBIT	52,9	8,81	61,7	6	1	3,35	3,35	3,35	10,1	213,5	18,42	0,541 9
63-AL1/11-ST1A	MINK	63,1	10,5	73,6	6	1	3,66	3,66	3,66	11,0	254,9	21,67	0,454 0
63-AL1/37-ST1A	SKUNK	63,2	36,9	100,1	12	7	2,59	2,59	7,77	13,0	463,0	52,79	0,456 8
75-AL1/13-ST1A	BEAVER	75,0	12,5	87,5	6	1	3,99	3,99	3,99	12,0	302,9	25,76	0,382 0
73-AL1/43-ST1A	HORSE	73,4	42,8	116,2	12	7	2,79	2,79	8,37	14,0	537,3	61,26	0,393 6
79-AL1/13-ST1A	RACOON	78,8	13,1	92,0	6	1	4,09	4,09	4,09	12,3	318,3	27,06	0,363 5
84-AL1/14-ST1A	OTTER	83,9	14,0	97,9	6	1	4,22	4,22	4,22	12,7	338,8	28,81	0,341 5
95-AL1/16-ST1A	CAT	95,4	15,9	111,3	6	1	4,50	4,50	4,50	13,5	385,3	32,76	0,300 3
105-AL1/17-ST1A	HARE	105,0	17,5	122,5	6	1	4,72	4,72	4,72	14,2	423,8	36,04	0,273 0
105-AL1/14-ST1A	DOG	105,0	13,6	118,5	6	7	4,72	1,57	4,71	14,2	394,0	32,65	0,273 3
132-AL1/20-ST1A	COYOTE	131,7	20,1	151,8	26	7	2,54	1,91	5,73	15,9	520,7	45,86	0,219 2
132-AL1/7-ST1A	COUGAR	131,5	7,31	138,8	18	1	3,05	3,05	3,05	15,3	418,8	28,74	0,218 8
131-AL1/31-ST1A	TIGER	131,2	30,6	161,9	30	7	2,38	2,38	7,08	16,5	602,2	57,87	0,220 2
158-AL1/37-ST1A	WOLF	158,1	36,9	194,9	30	7	2,59	2,59	7,77	18,1	725,3	68,91	0,182 9
159-AL1/9-ST1A	DINGO	158,7	8,81	167,5	18	1	3,35	3,35	3,35	16,8	505,2	35,67	0,181 4
183-AL1/43-ST1A	LYNX	183,4	42,8	226,2	30	7	2,79	2,79	8,37	19,5	841,6	79,97	0,157 6
184-AL1/10-ST1A	CARACAL	184,2	10,2	194,5	18	1	3,61	3,61	3,61	18,1	586,7	40,74	0,156 2
212-AL1/49-ST1A	PANTHER	212,1	49,5	261,5	30	7	3,00	3,00	9,00	21,0	973,1	92,46	0,136 3
211-AL1/12-ST1A	JAGUAR	210,6	11,7	222,3	18	1	3,86	3,86	3,86	19,3	670,8	46,57	0,136 8
238-AL1/56-ST1A	LION	238,3	55,6	293,9	30	7	3,18	3,18	9,54	22,3	1 093,4	100,47	0,121 3
264-AL1/62-ST1A	BEAR	264,4	61,7	326,1	30	7	3,35	3,35	10,1	23,5	1 213,4	111,50	0,109 3
324-AL1/76-ST1A	GOAT	324,3	75,7	400,0	30	7	3,71	3,71	11,1	26,0	1 488,2	135,13	0,089 1
375-AL1/88-ST1A	SHEEP	375,1	87,5	462,6	30	7	3,99	3,99	12,0	27,9	1 721,3	156,30	0,077 1
374-AL1/48-ST1A	ANTELOPE	374,1	48,5	422,6	54	7	2,97	2,97	8,91	26,7	1 413,8	118,88	0,077 3
382-AL1/49-ST1A	BISON	381,7	49,5	431,2	54	7	3,00	3,00	9,00	27,0	1 442,5	121,30	0,075 8
430-AL1/100-ST1A	DEER	429,6	100,2	529,8	30	7	4,27	4,27	12,8	29,9	1 971,4	179,00	0,067 3
429-AL1/56-ST1A	ZEBRA	428,9	55,6	484,5	54	7	3,18	3,18	9,54	28,6	1 620,6	131,92	0,067 4
477-AL1/111-ST1A	ELK	477,1	111,3	588,5	30	7	4,50	4,50	13,5	31,5	2 189,5	198,80	0,060 6
476-AL1/62-ST1A	CAMEL	476,0	61,7	537,7	54	7	3,35	3,35	10,1	30,2	1 798,8	146,40	0,060 8
528-AL1/69-ST1A	MOOSE	528,5	68,5	597,0	54	7	3,53	3,53	10,6	31,8	1 997,3	159,92	0,054 7

NOTE Direction of lay of external layer is right-hand (Z).

Appendix 3. ACSR conductors for various voltage levels

Table A3 – Possible selection of ACSR conductors for various voltage levels of overhead power lines [43]

Voltage [kV] / Power [MVA]	11	33	66	132	220	275	330	400	500
5	100-DOG[1]	25-GOPHER[1]							
	300-GOAT[2]	25-GOPHER[2]							
10	300-GOAT[1]	50-RABBIT[1]	25-GOPHER[1]						
	INADEQUATE	50-RABBIT[2]	25-GOPHER[2]						
25		200-PANTHER[1]	75-RACCOON[1]						
		200-PANTHER[2]	75-RACCOON[2]						
50			200-PANTHER						
100				200-PANTHER					
200				2×150-WOLF	250-BEAR				
300					2×175-LYNX	400-ZEBRA			
400					2×250-BEAR	2×175-LYNX			
500					2×400-ZEBRA	2×250-BEAR (2× BATANG)			
600						2×350-ANTELOPE or BISON			
700							2×350-ANTELOPE or BISON		
800							3×300-GOAT	2×400-ZEBRA	
1000								3×250-BEAR or DOVE	
1200								3×400-ZEBRA	
1800								4×400-ZEBRA or 4×CROW	3×450-ELK 4×(282)DOVE
2000									4×300-GOAT

Several notes should be given about Table A3:

- The numbers given in the table next to the conductor codes refer to the nominal aluminium area (for example, '200-Panther' means that the conductor's code name is 'Panther' and its cross-sectional area of aluminium is 200 mm^2).
- For voltages up to and including 66 kV, conductor size is governed by thermal rating and/or voltage drop (because surface gradients are normally acceptable):
  - [1] – thermal rating
  - [2] – Rating for 10% voltage drop with power factor 0.9 over a distance of 10km
- For voltages 132 kV and above, the conductor size is also governed by surface gradient and electrical stability of systems. Although variations are possible, typically minimum conductor sizes would be:
  - 132 kV - 1 × 14.2 mm
  - 275 kV - 2 × 19.3 mm
  - 400 kV - 4 × 18 mm
- Data shown in the table are prepared for tropical conditions. For temperate conditions, where temperatures are relatively moderate, ratings would be 20–30% higher.

Appendix 4. BH curves of the considered materials for the magnetic circuit

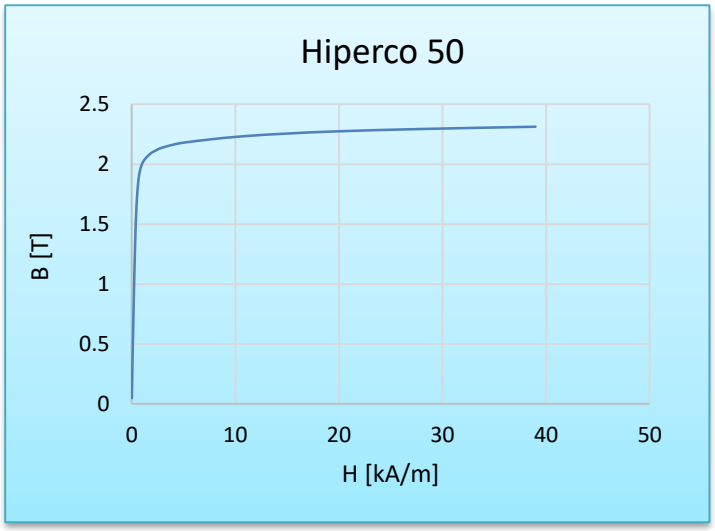

Figure A4.1 – BH curve of Hiperco 50 alloy [100]

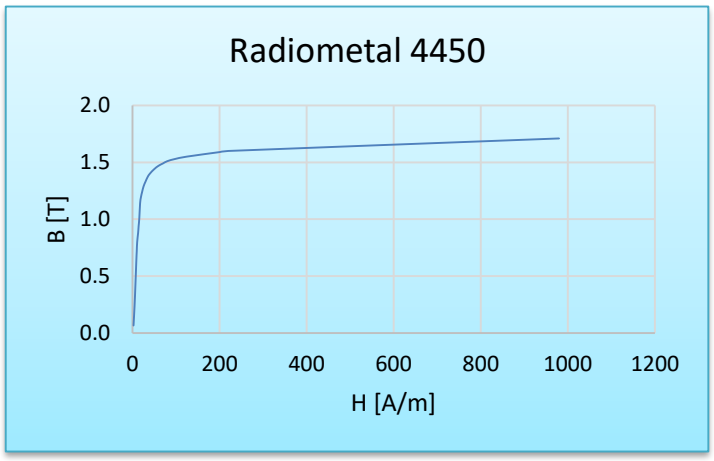

Figure A4.2 – BH curve of Radiometal 4550 alloy [100]

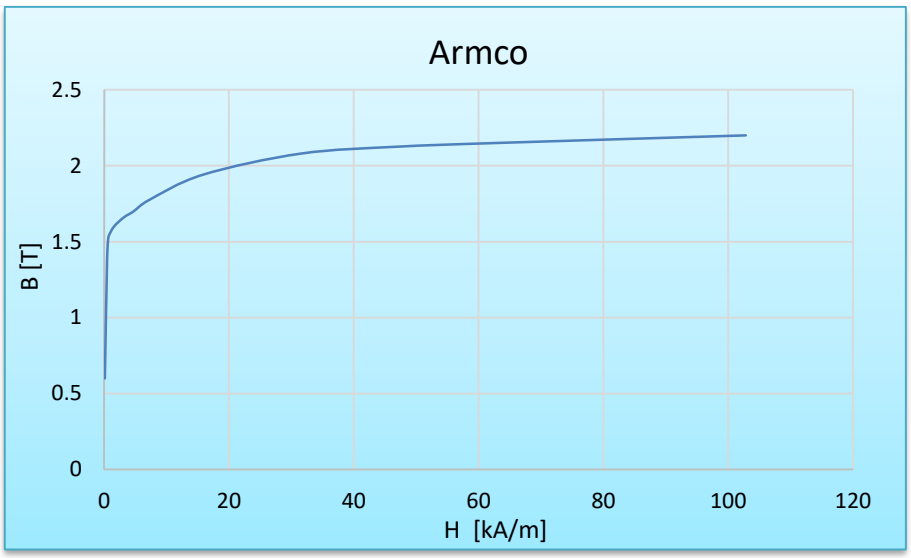

Figure A4.3 – BH curve of Armco [100]

Appendix 5. Data table obtained from $B_{surface}$ - ε and ε-μ_r graphs

Table A4 – Data table obtained from $B_{surface}$ - ε and ε-μ_r graphs

ε [%]	μ_r	$B_{surface}$ [T]
0	2.00	0.08535648
0.30	2.26	0.14235084
0.71	2.43	0.17871513
1.05	3.08	0.20110240
1.39	3.64	0.22761728
1.66	4.15	0.24629243
1.91	5.05	0.26209914
2.20	5.88	0.28452160
2.32	6.86	0.29533995
2.42	7.31	0.29826322
2.50	7.68	0.30739465
2.64	8.33	0.31182475
2.73	8.95	0.32396985
2.89	9.75	0.33431288
3.10	10.80	0.34797375
3.30	11.78	0.36604072
3.47	12.60	0.37734200
3.58	13.46	0.38864327
3.78	14.60	0.40633241
3.93	16.05	0.41575126
4.07	17.82	0.42931279
4.16	18.97	0.43478260
4.30	20.20	0.43930311
4.39	21.31	0.44683730

4.48	22.45	0.46491933
4.60	23.65	0.46501499
4.88	28.78	0.48724324
5.04	29.80	0.50324758
5.29	34.65	0.51658453
5.46	37.83	0.53703452
5.60	41.74	0.55126060
5.82	46.88	0.56904320
6.00	50.00	0.58949319

Appendix 6. ANSYS ELECTROMAGNETIC ANALYSIS CODE


```
/PREP7
counter2=0
FINISH
*DO,counter1,1,700,1
PARSAV,SCALAR
/CLEAR
PARRES,NEW
/PREP7

!Defining the parameters

*ask,n_st_wires,Number of steel wires,7
*ask,d_st,Diameter of steel wires (mm),3.53
*ask,n_al_wires,Number of aluminium wires,54
*ask,d_al,Diameter of aluminium wires (mm),3.53
*ask,I_cable,Value of electrical current (A),2500
*ask,ff,Frequency (Hz),50
*ask,sigma_concentrator,Conductivity of magnetic concentrator(S/m), 2.494e6
*ask,r_in, Inner radius of the magnetic concentrator (mm),35
*ask,conc_width,Width of magnetic concentrator (mm),10
*ask,conc_tip_length,Length of mag. concentrator tip (mm),20
*ask,air_gap,Width of air gap (mm),0.1
I_cable=100+5*counter2
*IF,I_cable,EQ,2000,THEN
        *EXIT
*ENDIF
counter2=counter2+1
n_wires=n_st_wires+n_al_wires
R=2.8264e-8                 !Resistivity of aluminium (om m)
R_st=19.2e-8                !Resistivity of steel (om m)
R_air=2e16                  !resistivity of air (om m)
R_msm=7e-7                  !resistivity of MSM element (om m)
R_concentrator=1/sigma_concentrator
mu_concentrator=10000       !magnetic permeability of magnetic concentrator
r_circle_air=280
```

```
circlegap=0.07
surfacegap=0.15
pi=acos(-1)
msm_side1=1                !the shortest side of msm element (mm)
msm_side2=3                !medium long side of msm element (mm)
msm_side3=10               !the longest side of msm element (mm)
rows_B_strain=33
*dim,msm_B_strain,array,rows_B_strain,2          ! MSM B vs strain (ETO's graph)
*dim,msm_B_strain_difference,array,rows_B_strain,2
*dim,msm_B_strain_difference_abs,array,rows_B_strain,2
msm_B_strain(1,1)=0.08535648,0.142350844,0.178715129,0.201102399,0.227617279,0.24
6292426,0.262099141,0.284521599
msm_B_strain(9,1)=0.295339954,0.298263217,0.307394646,0.311824745,0.323969847,0.3
34312879,0.347973753,0.366040722
msm_B_strain(17,1)=0.377341996,0.38864327,0.406332408,0.415751258,0.429312787,0.4
34782603,0.439303113,0.446837295
msm_B_strain(25,1)=0.464919333,0.465014988,0.487243238,0.503247578,0.516584528,0.
537034518,0.551260598,0.569043198
msm_B_strain(33,1)=0.589493188
msm_B_strain(1,2)=0,0.30,0.71,1.05,1.39,1.66,1.91,2.20
msm_B_strain(9,2)=2.32,2.42,2.50,2.64,2.73,2.89,3.10,3.30
msm_B_strain(17,2)=3.47,3.58,3.78,3.93,4.07,4.16,4.30,4.39
msm_B_strain(25,2)=4.48,4.60,4.88,5.04,5.29,5.46,5.60,5.82
msm_B_strain(33,2)=6.00
rows_mu_strain=33
*dim,msm_mu_strain,array,rows_mu_strain,2       ! MSM mag. permeabilty vs strain
*dim,msm_mu_strain_difference,array,rows_mu_strain,2
*dim,msm_mu_strain_difference_abs,array,rows_mu_strain,2
msm_mu_strain(1,1)=0.00,0.30,0.71,1.05,1.39,1.66,1.91,2.20
msm_mu_strain(9,1)=2.32,2.42,2.50,2.64,2.73,2.89,3.10,3.30
msm_mu_strain(17,1)=3.47,3.58,3.78,3.93,4.07,4.16,4.30,4.39
msm_mu_strain(25,1)=4.48,4.60,4.88,5.04,5.29,5.46,5.60,5.82
msm_mu_strain(33,1)=6.00
msm_mu_strain(1,2)=2.00,2.26,2.43,3.08,3.64,4.15,5.05,5.88
msm_mu_strain(9,2)=6.86,7.31,7.68,8.33,8.95,9.75,10.80,11.78
msm_mu_strain(17,2)=12.60,13.46,14.60,16.05,17.82,18.97,20.20,21.31
msm_mu_strain(25,2)=22.45,23.65,28.78,29.80,34.65,37.83,41.74,46.88
msm_mu_strain(33,2)=50.00
MP,MURX,1,1                !material one is air around the cable
MP,RSVX,1,R_air
MP,MURX,2,1                !material 2 is aluminium
```

```
MP,RSVX,2,R
MP,MURX,3,100                !material 3 is steel
MP,RSVX,3,R_st
MP,MURX,4,1                  !material 4 is air inside the cable, between strands
MP,RSVX,4,R_air
*IF,counter1,EQ,1,THEN
        msm_mu_initial=2
*ENDIF
MP,RSVX,6,R_msm                    !material 6 is hard MSM
MP,MURX,6,msm_mu_initial
MP,RSVX,7,R_concentrator                    !material 7 is magnetic concentrator
TB,BH,7,1,33
!nl-core-hip50-can
TBPT,,10.0000000,4.900000000E-02
TBPT,,15.0000000,7.200000000E-02
TBPT,,29.0000000,0.142000000
TBPT,,43.0000000,0.207000000
TBPT,,55.0000000,0.265000000
TBPT,,75.0000000,0.357000000
TBPT,,101.000000,0.472000000
TBPT,,132.000000,0.605000000
TBPT,,181.000000,0.810000000
TBPT,,246.000000,1.06100000
TBPT,,314.000000,1.29800000
TBPT,,344.000000,1.39200000
TBPT,,394.000000,1.52400000
TBPT,,442.000000,1.62000000
TBPT,,503.000000,1.72000000
TBPT,,643.000000,1.86800000
TBPT,,787.000000,1.94400000
TBPT,,923.000000,1.98600000
TBPT,,1006.00000,2.00500000
TBPT,,1107.00000,2.02200000
TBPT,,1378.00000,2.05400000
TBPT,,1763.00000,2.08600000
TBPT,,1989.00000,2.10000000
TBPT,,2474.00000,2.12200000
TBPT,,2998.00000,2.14000000
TBPT,,4322.00000,2.17000000
TBPT,,5341.00000,2.18400000
TBPT,,7549.00000,2.20700000
```

```
TBPT,,10669.0000,2.23300000
TBPT,,14977.0000,2.25600000
TBPT,,20003.0000,2.27500000
TBPT,,28352.0000,2.29500000
TBPT,,38978.0000,2.31300000
ET,1,PLANE53
ET,2,PLANE53,1

!Geometry

n_al1=0
n_al_i_temp=0
n_al_j_temp=0
n_al_i=0
n_al_j=0
n_st_layers=0
n_al_layers=0
n_total_layers=0
*IF,d_al,EQ,d_st,OR,n_st_wires,EQ,0,THEN
sum_total=0
sum_st=0
sum_al=0
*DO,i,1,50,1    ! counts the number of total and steel layers, as well as a number of
        aluminium layers in the case when there are no steel layers
*IF,sum_total,GE,n_wires,THEN                !calculating the total number of layers
*exit
*ELSEIF,i,EQ,1,THEN
sum_total=1
n_total_layers=1
*ELSE
sum_total=sum_total+6*(i-1)
n_total_layers=i
*ENDIF
*IF,sum_st,LT,n_st_wires,THEN                !calculating the number of steel layers
        *IF,i,EQ,1,THEN
        sum_st=1
        n_st_layers=1
        *ELSE
        sum_st=sum_st+6*(i-1)
        n_st_layers=n_st_layers+1
        *ENDIF
```

```
*ENDIF
n_al_layers=n_total_layers-n_st_layers        !number of aluminium layers
*ENDDO
*ELSE
sum=0
*DO,i,1,50,1                        !this "do loop" counts number of steel layers
*IF,sum,GE,n_st_wires,THEN
*exit
*ELSEIF,i,EQ,1,THEN
sum=1
n_st_layers=1
*ELSE
sum=sum+6*(i-1)
n_st_layers=i
*ENDIF
*ENDDO
!the lines below calculate the number of strands in the first layer of aluminium
n_al1_temp=2*pi/d_al*(d_st/2+(n_st_layers-1)*d_st+d_al/2)
n_al1=NINT(n_al1_temp)
*IF,n_al1,GT,n_al1_temp,THEN
n_al1=n_al1-1
*ENDIF
n_al_layers=1
sum_al=n_al1
*DO,i,2,50,1                        !this "do loop" counts number of aluminium layers
*IF,sum_al,GE,n_al_wires,THEN
*exit
*ELSE
!the lines bellow calculate the number of strands in the "i" layer of aluminium
 n_al_i_temp=n_al1*(1+(i-1)*d_al/(d_st/2+(n_st_layers-1)*d_st+d_al/2))
n_al_i=NINT(n_al_i_temp)
*IF,n_al_i,GT,n_al_i_temp,THEN
n_al_i=n_al_i-1
*ENDIF
sum_al=sum_al+n_al_i
n_al_layers=i
*ENDIF
*ENDDO
n_total_layers=n_st_layers+n_al_layers
*ENDIF
CYL4,0,0,r_circle_air
```

```
*IF,n_st_layers,GT,0,THEN
CYL4,0,0,d_st/2
AGEN,n_st_layers,2, , ,(d_st+circlegap), , , ,0
distance_al=(n_st_layers-1)*d_st+d_st/2+n_st_layers*circlegap+d_al/2
CYL4,distance_al,0,d_al/2
AGEN,n_al_layers,(n_st_layers+2), , ,(d_al+circlegap), , , ,0
CSYS,1
*IF,n_st_layers,GT,1,THEN                    !generation of steel wires
*DO,i,1,(n_st_layers-1),1
AGEN,(6*i),(i+2), , , ,(60/i), , ,0
*ENDDO
*ENDIF
*IF,d_st,EQ,d_al,THEN                        !generation of aluminium wires
*DO,j,n_st_layers,n_total_layers-1,1
AGEN,(6*j),(j+2), , , ,(60/j), , ,0
*ENDDO
*ELSE
*DO,j,1,n_al_layers,1
!lines bellow calculate number of wires in the "j" layer of aluminium
n_al_j_temp=n_al1*(1+(j-1)*d_al/(d_st/2+(n_st_layers-1)*d_st+d_al/2))
n_al_j=NINT(n_al_j_temp)
*IF,n_al_j,GT,n_al_j_temp,THEN
n_al_j=n_al_j-1
*ENDIF
AGEN,n_al_j,(n_st_layers+1+j), , , ,(360/n_al_j), , ,0
*ENDDO
*ENDIF                                       !end of generation of aluminium strands
CSYS,0
CYL4,0,0,(d_st/2+(n_st_layers-1)*d_st+n_al_layers*d_al+(n_total_layers-
1)*circlegap+surfacegap)
*ELSE                                        !if  there are only aluminium strands (no steel)
CYL4,0,0,d_al/2
*IF,n_al_layers,GT,1,THEN
AGEN,n_al_layers,2, , ,(d_al+circlegap), , , ,0
CSYS,1
*DO,i,1,(n_al_layers-1),1
AGEN,(6*i),(i+2), , , ,(60/i), , ,0          !there are 6*i more strands for each i-th layer,so
the needed space for them is 360/(6*i) i.e. 60/i
*ENDDO
*ENDIF
CSYS,0
```

```
CYL4,0,0,(d_al/2+(n_al_layers-1)*d_al+(n_al_layers-1)*circlegap+surfacegap)
*ENDIF
AOVLAP,ALL
*IF,n_st_layers,GT,0,THEN
d_cable=d_st/2+(n_st_layers-1)*d_st+n_al_layers*d_al+(n_total_layers-
1)*circlegap+surfacegap
*ELSE
d_cable=d_al/2+(n_al_layers-1)*d_al+(n_total_layers-1)*circlegap+surfacegap
*ENDIF
*GET,MinAreaNum,AREA,,NUM,MIN, , , ,
*GET,MaxAreaNum,AREA,,NUM,MAX, , , ,
CSYS,1
*IF,n_total_layers,GT,1,THEN                    !layers around the central strand
        *IF,n_st_layers,GT,1,THEN
        ASEL,S,LOC,X,(d_st/2+circlegap),(d_st/2+(n_st_layers-1)*d_st+(n_st_layers-
1)*circlegap)
        AATT,3,,1,0,
        *ENDIF
        *IF,n_st_layers,GT,0,THEN
        ASEL,S,LOC,X,(d_st/2+(n_st_layers-1)*d_st+n_st_layers*circlegap),
(d_st/2+(n_st_layers-1)*d_st+n_al_layers*d_al+(n_total_layers-1)*circlegap)
        AATT,2,,2,0,
        *ELSE
        ASEL,S,LOC,X,(d_al/2+circlegap),(d_al/2+(n_total_layers-1)*d_al+(n_total_layers-
1)*circlegap)
        AATT,2,,2,0,
        *ENDIF
*ENDIF

*IF,n_st_layers,GT,0,THEN
        ASEL,S,LOC,X,0,d_st/2
        AATT,3,,1,0,
*ELSE
        ASEL,S,LOC,X,0,d_al/2
        AATT,2,,2,0,

*ENDIF
CSYS,0
ASEL,S,AREA,,(MaxAreaNum-1)
AATT,1,,1,0,
ASEL,S,AREA,,MaxAreaNum
```

```
AATT,4,,1,0,


ASEL,NONE
*IF,n_st_layers,GT,0,THEN     !geometry for hard msm and concentrator
KSEL,NONE      !kp1-kp8 are kps for drawing lines of  the outside rectangular of concentrator
K,,r_in,r_in+conc_width
*GET,kp_conc_1,KP,0,NUM,MAX
KSEL,NONE
K,,-r_in,r_in+conc_width
*GET,kp_conc_2,KP,0,NUM,MAX
KSEL,NONE
K,,-r_in-conc_width,r_in
*GET,kp_conc_3,KP,0,NUM,MAX
KSEL,NONE
K,,-r_in-conc_width,-r_in
*GET,kp_conc_4,KP,0,NUM,MAX
KSEL,NONE
K,,-r_in,-r_in-conc_width
*GET,kp_conc_5,KP,0,NUM,MAX
KSEL,NONE
K,,r_in,-r_in-conc_width
*GET,kp_conc_6,KP,0,NUM,MAX
KSEL,NONE
K,,r_in+conc_width,-r_in
*GET,kp_conc_7,KP,0,NUM,MAX
KSEL,NONE
K,,r_in+conc_width,r_in
*GET,kp_conc_8,KP,0,NUM,MAX
KSEL,NONE !kp9-kp12 are kps for defining the centers of the outside arcs in the corners of
rectangular
K,,-r_in,r_in
*GET,kp_conc_9,KP,0,NUM,MAX
KSEL,NONE
K,,-r_in,-r_in
*GET,kp_conc_10,KP,0,NUM,MAX
KSEL,NONE
K,,r_in,-r_in
*GET,kp_conc_11,KP,0,NUM,MAX
KSEL,NONE
K,,r_in,r_in
```

```
*GET,kp_conc_12,KP,0,NUM,MAX
KSEL,ALL
LSEL,NONE                    !outside lines of the concentrator
L,kp_conc_1,kp_conc_2
*GET,line_conc_1,LINE,0,NUM,MAX
LSEL,NONE
L,kp_conc_3,kp_conc_4
*GET,line_conc_2,LINE,0,NUM,MAX
LSEL,NONE
L,kp_conc_5,kp_conc_6
*GET,line_conc_3,LINE,0,NUM,MAX
LSEL,NONE
L,kp_conc_7,kp_conc_8
*GET,line_conc_4,LINE,0,NUM,MAX
LSEL,NONE
LARC,kp_conc_2,kp_conc_3,kp_conc_9,conc_width
*GET,line_conc_5,LINE,0,NUM,MAX
LSEL,NONE
LARC,kp_conc_4,kp_conc_5,kp_conc_10,conc_width
*GET,line_conc_6,LINE,0,NUM,MAX
LSEL,NONE
LARC,kp_conc_6,kp_conc_7,kp_conc_11,conc_width
*GET,line_conc_7,LINE,0,NUM,MAX
LSEL,NONE
LARC,kp_conc_8,kp_conc_1,kp_conc_12,conc_width
*GET,line_conc_8,LINE,0,NUM,MAX
LSEL,A,LINE,,line_conc_7
LSEL,A,LINE,,line_conc_6
LSEL,A,LINE,,line_conc_5
LSEL,A,LINE,,line_conc_4
LSEL,A,LINE,,line_conc_3
LSEL,A,LINE,,line_conc_2
LSEL,A,LINE,,line_conc_1
CSYS,1
LSSCALE,ALL,,,r_in/(r_in+conc_width),,,,0,0
CSYS,0
ASEL,NONE
AL,ALL
*GET,concentrator_without_gap_number,AREA,0,NUM,MAX
LSEL,ALL
ASEL,NONE
```

```
RECTNG,-msm_side1/2-air_gap,msm_side1/2+air_gap,-r_in+1,-
(r_in+conc_width+1)*GET,concentrator_gap_number,AREA,0,NUM,MAX
ASEL,A,AREA,,concentrator_without_gap_number
ASBA,concentrator_without_gap_number,ALL,SEPO,DELETE,DELETE
*GET,concentrator_number1,AREA,0,NUM,MAX
ASEL,S,AREA,,concentrator_number1
AATT,7,,1,0
ASEL,NONE
X1_temp1=-msm_side1/2-air_gap-conc_tip_length
y1_temp1=-r_in
X2_temp1=-msm_side1/2-air_gap/2
y2_temp1=-r_in
x3_temp1=-msm_side1/2-air_gap/2
y3_temp1=-r_in-conc_width
x4_temp1=-msm_side1/2-air_gap-conc_tip_length
y4_temp1=-r_in-conc_width
x5_temp1=-msm_side1/2-air_gap
y5_temp1=-r_in-conc_width/2-msm_side2/2
x6_temp1=-msm_side1/2-air_gap
y6_temp1=-r_in-conc_width/2+msm_side2/2
PTXY,X1_temp1,y1_temp1,X2_temp1,y2_temp1,X3_temp1,y3_temp1,X4_temp1,y4_temp1
PTXY,X5_temp1,y5_temp1,X6_temp1,y6_temp1
POLY
*GET,area_temp1_left_number,AREA,0,NUM,MAX
ASEL,S,AREA,,concentrator_number1
ASEL,A,AREA,,area_temp1_left_number
ASBA,concentrator_number1,area_temp1_left_number,SEPO,DELETE,DELETE    !deleting
hexagon from the tip of mag. conc. on the lest hand side of msm
*GET,concentrator_number2,AREA,0,NUM,MAX
ASEL,NONE
X1_temp2=msm_side1/2+air_gap+conc_tip_length
y1_temp2=-r_in
X2_temp2=msm_side1/2+air_gap/2
y2_temp2=-r_in
x3_temp2=msm_side1/2+air_gap/2
y3_temp2=-r_in-conc_width
x4_temp2=msm_side1/2+air_gap+conc_tip_length
y4_temp2=-r_in-conc_width
x5_temp2=msm_side1/2+air_gap
y5_temp2=-r_in-conc_width/2-msm_side2/2
x6_temp2=msm_side1/2+air_gap
```

```
y6_temp2=-r_in-conc_width/2+msm_side2/2
PTXY,X1_temp2,y1_temp2,X2_temp2,y2_temp2,X3_temp2,y3_temp2,X4_temp2,y4_temp2
PTXY,X5_temp2,y5_temp2,X6_temp2,y6_temp2
POLY
*GET,area_temp2_right_number,AREA,0,NUM,MAX
ASEL,S,AREA,,concentrator_number2
ASEL,A,AREA,,area_temp2_right_number
ASBA,concentrator_number2,area_temp2_right_number,SEPO,DELETE,DELETE  !deleting
hexagon from the tip of mag. conc. on the lest hand side of msm
*GET,concentrator_number,AREA,0,NUM,MAX
ASEL,S,AREA,,concentrator_number
AATT,7,,1,0
ASEL,NONE
RECTNG,-msm_side1/2,msm_side1/2,-r_in-conc_width/2+msm_side2/2,-r_in-conc_width/2-
msm_side2/2            ! msm hard element -  in the middle of air gap
*GET,msm_hard_area_number,AREA,0,NUM,MAX
ASEL,S,AREA,,msm_hard_area_number
AATT,6,,1,0
*ELSE
msm_distance_hard=msm_from_cable_hard+d_al/2+(n_al_layers-1)*d_al+(n_total_layers-
1)*circlegap+surfacegap
RECTNG,msm_distance_hard,msm_distance_hard+1,-1.5,1.5
*GET,msm_hard_area_number,AREA,0,NUM,MAX
ASEL,S,AREA,,msm_hard_area_number
AATT,6,,1,0
ASEL,NONE
RECTNG,msm_distance_hard-air_gap-conc_length,msm_distance_hard-air_gap,-
conc_height/2,conc_height/2          !concentrator left from the msm element
*GET,concentrator_left_area_number,AREA,0,NUM,MAX
ASEL,S,AREA,,concentrator_left_area_number
AATT,7,,1,0
ASEL,NONE
RECTNG,msm_distance_hard+1+air_gap,msm_distance_hard+1+air_gap+conc_length,-
conc_height/2,conc_height/2                    !concentrator right from the msm element ("+1"
because 1mm is msm eleemnts width)
*GET,concentrator_right_area_number,AREA,0,NUM,MAX
ASEL,S,AREA,,concentrator_right_area_number
AATT,7,,1,0
*ENDIF
ALLSEL,ALL
AOVLAP,ALL
```

```
!Mesh and applying loads

ASEL,S,MAT,,1,7         !
ASEL,INVE
AATT,1,,1,0
ASEL,ALL
ARSCALE,ALL,,,0.001,0.001,1,,0,1      !scale all geometry (mm to m)
SMRT,3
MSHAPE,1,2D
MSHKEY,0
ALLSEL,ALL
AMESH,ALL
ASEL,S,MAT,,6,7
AREFINE,ALL,,,3
ASEL,S,MAT,,7
AREFINE,ALL,,,3
ASEL,S,MAT,,1
NSLA
NSEL,R,LOC,X,-msm_side1/2000,(-msm_side1/2-air_gap)/1000
NSEL,A,LOC,X,msm_side1/2000,(msm_side1/2+air_gap)/1000
NSEL,R,LOC,y,-r_in/1000,(-r_in-conc_width)/1000
ESLN
EREFINE,ALL,,,3
ALLSEL,ALL
ANTYPE,HARMIC
CSYS,1
ESEL,ALL
NSEL,S,LOC,X, r_circle_air/1000
D,ALL,AZ,0
ESEL,S,MAT,,2
NSLE,S
CP,1,VOLT,ALL
*GET,N1,NODE,,NUM,MIN
F,N1,AMPS,I_cable
ASUM                    !area of aluminium strands (elements)
*GET,AlumArea,AREA,,AREA,
*SET,I_cab,I_cable
*SET,J_cab,I_cab/Alumarea   !current density (when current is uniformly distributed - DC)
CSYS,0
ALLSEL,ALL
FINISH
```

```
/SOLU
NEQIT,150
HARFRQ,ff
SOLVE
FINISH

!Results

/POST1
SET,1,1
ETABLE,JTReal,JT,sum
ETABLE,BReal,B,sum
SET,1,1,,1
ETABLE,JTImag,JT,sum
ETABLE,BImag,B,sum
SMULT,JTReal2,JTREAL,JTREAL,1,1
SMULT,BReal2,BReal,BREAL,1,1
SMULT,JTImag2,JTImag,JTImag,1,1
SMULT,BImag2,BImag,BImag,1,1
SADD,R2addI2,JTReal2,JTImag2,1,1
SADD,BR2addI2,BReal2,BImag2,1,1
SEXP,Jampl,R2addI2,,1/2
SEXP,Bampl,BR2addI2,,1/2
*IF,n_st_layers,GT,0,THEN
PATH,JTPath,2,6,200
startpointX=0
dist_cable=5            !distance from the surface of the conductor (mm)
PPATH,1,,startpointX,0,
PPATH,2,,(d_cable+dist_cable)/1000,0,
PDEF,jtpath,ETAB,Jampl,NOAV
PATH,BPath,2,,100
d_cable=d_st/2+(n_st_layers-1)*d_st+n_al_layers*d_al+(n_total_layers-
1)*circlegap+surfacegap
startpointY=-r_in-conc_width/2+msm_side2/2
endpointY=-r_in-conc_width/2-msm_side2/2
startpointX=msm_side1/2+air_gap/2
endpointX=msm_side1/2+air_gap/2
PPATH,1,,startpointX/1000,startpointY/1000
PPATH,2,,endpointX/1000,endpointY/1000
PDEF,bpath,ETAB,Bampl                    !magnetic density plot
```

```
PCALC,INTG,Bamp_avg_path,Bpath,S,1/(msm_side2*0.001),
*GET,Bamp_avg,PATH,0,MAX,Bamp_avg_path
ASEL,S,MAT,,7
ESLA
ESORT,ETAB,Bampl,0
*GET,Bamp_max_mat7,SORT,0,MAX
*ELSE
PATH,JTPath,2,100,100
startpointX=0
dist_cable=5              !distance from the surface of the conductor (mm)
PPATH,1,,startpointX,0,
PPATH,2,,(d_cable+dist_cable)/1000,0,
PDEF,jtpath,ETAB,Jampl
PATH,BPath,2,,100
startpointX=d_cable
dist_cable=100
PPATH,1,,startpointX/1000,0,
PPATH,2,,(d_cable+dist_cable)/1000,0,
PDEF,bpath,ETAB,Bampl
*ENDIF
ALLSEL,ALL
*STATUS,I_cable
*STATUS,Bamp_avg
*STATUS,Bamp_max_mat7
Brms_avg=Bamp_avg/SQRT(2)
*VABS,1,1
*VSCFUN,msm_B_strain_difference_index,LMIN,msm_B_strain_differencestrain=msm_B_st
rain(msm_B_strain_difference_index,2)
msm_B_difference_value=msm_B_strain_difference(msm_B_strain_difference_index,1)
*VOPER,msm_mu_strain_difference,msm_mu_strain,SUB,strain
*VABS,1,1
*VSCFUN,msm_mu_strain_difference_index,LMIN,msm_mu_strain_difference
msm_mu=msm_mu_strain(msm_mu_strain_difference_index,2)
msm_mu_difference_value=msm_mu_strain_difference(msm_mu_strain_difference_index,
1)
*IF,msm_mu,NE,msm_mu_initial,THEN
counter2=counter2-1
*ELSE
/INPUT,BNvwrit70.txt
*ENDIF
/INPUT,BNvwrit71.txt
```

```
msm_mu_initial=msm_mu
FINISH
/prep7
ALLSEL,ALL
VCLEAR,ALL
ACLEAR,ALL
LCLEAR,ALL
KCLEAR,ALL
VDELE,ALL
ADELE,ALL
LDELE,ALL
KDELE,ALL
FINISH
*ENDDO          !do loop from the beginning of the code
```